LEVEL II

(12)

SGI-R-80-022

# SEISMIC PROPAGATION IN THE KURILES/KAMCHATKA REGION

R. S. HART

S. K. KAUFMAN



FINAL TECHNICAL REPORT

SPONSORED BY

DEFENSE ADVANCED RESEARCH PROJECTS AGENCY (DoD)

ARPA ORDER No. 3693

MONITORED BY ONR UNDER CONTRACT #N00014-80-C-0250



The views and conclusions contained in this document are those of the authors and should not be interpreted as necessarily representing the official policies, either expressed or implicit, of the Defense Advanced Research Projects Agency or the United States Government.

July 25, 1980



SIERRA GEOPHYSICS, INC.

150 N. SANTA ANITA AVENUE • ARCADIA, CALIFORNIA 91006 • (213) 574-7052

# Sierra Geophysics, Inc.

150 N. Santa Anita Ave. • Suite 880 • Arcadia, California 91006 • (213) 574-7052



SGI-R-80-022


# SEISMIC PROPAGATION IN THE KURILES/KAMCHATKA REGION


R. S. HART

S. K. KAUFMAN


FINAL TECHNICAL REPORT


SPONSORED BY

DEFENSE ADVANCED RESEARCH PROJECTS AGENCY (DoD)

ARPA ORDER No. 3693

MONITORED BY ONR UNDER CONTRACT #N00014-80-C-0250





July 25, 1980

ABSTRACT

An analysis of seismic propagation in the crust and upper mantle of the Kuriles/Kamchatka region has been completed in support of the MSS site evaluation. Both three-dimensional ray tracing techniques and generalized ray theory methods have been utilized to model the propagation through a highly complex, laterally varying structure. The structural model of the upper mantle and descending lithospheric slab developed by Veith (1974) was modified for this study to include the observed change in angle of descent of the slab along the trench. The intensity of incident seismic energy at the surface was mapped and contoured for seismic rays refracting through the three-dimensional mantle structure. Synthetic seismogram profiles were also computed to investigate the waveguide effects of the lithosphere at the surface and to analyze the contribution of diffracted and multiple reflected energy, particularly within areas of classical shadow zones.

TABLE OF CONTENTS

## INTRODUCTION

In many, if not most, situations involving the calculation of seismic propagation within the earth, the assumption that seismic properties vary only with depth may be used successfully. Under these circumstances, the normal vectors to the propagating wavefronts, or rays, are well-behaved, remaining within their initial planes of propagation through the earth. As a result of the spherical symmetry, the travel-times and amplitudes of seismic phases depend only on distance from the source and not upon the source-receiver azimuth. However, in the presence of large-scale, localized heterogeneities in the crust or upper mantle, symmetry assumptions break down and relatively simple techniques for calculating ray paths, travel-times, and amplitudes are inadequate. This situation is particularly acute when the lateral heterogeneities are in the near-source region. Complex computational schemes must then be employed to follow the seismic rays point by point through the earth. The region encompassing northernmost Japan, the Kurile Islands, and the Kamchatka peninsula is typified by laterally heterogeneous crust and upper mantle structures. Any detailed evaluation of seismic propagation within this region must, therefore, take into account these variations in seismic properties.

Planning is currently underway for the deployment of a down-hole, ocean bottom seismometer system, the Marine Seismic System (MSS), roughly several hundred kilometers east or south-

east of the Kurile Islands. Such a sophisticated seismic monitoring system will be invaluable in increasing not only our capabilities for nuclear test monitoring and verification but also our knowledge and understanding of the earthquakes and tectonics of the northwest Pacific and the interaction between the Pacific and Asian plates at the Kurile Trench. Among the many considerations involved in the site selection for the MSS, the characteristics of seismic propagation between the centers of seismic activity in the Kuriles/Kamchatka region and the proposed MSS sites must be considered. This report examines seismic propagation in the Kuriles/Kamchatka region and analyzes the potential problems and advantages of the sites under consideration from a seismological viewpoint. This analysis has included examination of the laterally heterogeneous structure, distribution of seismicity, types and spatial distribution of source mechanisms, and the propagation characteristics of the area, including both geometric ray propagation and non-geometric paths (diffracted arrivals, head waves, etc.).

EARTH MODEL SELECTION

The Kuriles/Kamchatka region is, geomorphologically, a typical oceanic trench/island arc structure. To the east of the islands is a deep oceanic trench. The islands, as well as much of the Kamchatka peninsula, are highly volcanic. Seismically, the area is extremely active. Hypocentral depths range from the surface to 600-700 km in the mantle. This kind of geomorphologic and tectonic feature is very successfully described within the framework of seafloor spreading and plate tectonics.

The theory of plate tectonics is now widely accepted by earth scientists and is regularly employed in interpreting geological and geophysical observations and explaining the tectonic environment and evolution of the earth. The prime concept of plate tectonics is that the outer layer of the earth, the lithosphere, is broken into a number of relatively rigid, individual plates, each moving relative to one another. The driving mechanism for this motion is generally presumed to be thermally-derived. The plates interact in primarily three different modes. In regions where the motion is divergent, new material upwells from deeper in the mantle, forming long ridge-like or rifting structures. The mid-oceanic ridge system is the most prominent such feature. Earthquake mechanisms associated with this tectonic activity are generally tensional or normal faulting. The second interaction occurs where two plates are moving in roughly parallel directions, a transform

fault type of relationship. Such regions (e.g., the San Andreas fault zone in California) are typified by strike-slip earthquake faulting. The third region of interaction is a convergent zone, the type of zone of most interest to us in this study. In a typical convergent zone, one plate is underthrusting the second. In Figure 1, from Ringwood 1969), the general framework of this zone is illustrated. The seismicity in convergent zones ranges in depth from very shallow to quite deep (600-700 km) following a dipping zone of seismic activity, called a Benioff zone. The faulting types within this zone include normal, thrust, and strike-slip mechanisms. However, the different kinds of faulting are not randomly mixed but occur in systematic patterns based on the local tectonic environment (for example, in the region of maximum bending on the top of the underthrust slab, the earthquakes show tensional faulting). In some regions, such as the Northeast Japan arc, the seismicity falls into a double plane, clearly resolving the downgoing slab (Figure 2).

The Kurile Island/Kamchatka region is a zone of convergence between the Pacific and Asian plates. The Pacific plate is sharply underthrusting the Asian plate in this region. The angle of underthrusting, and therefore, the dip of the Benioff zone defining the focus of seismic activity, is steeply dipping. It is this highly complex, laterally heterogeneous region that must be modeled in order to analyze seismic propagation in support of the MSS site evaluation. Fortunately,

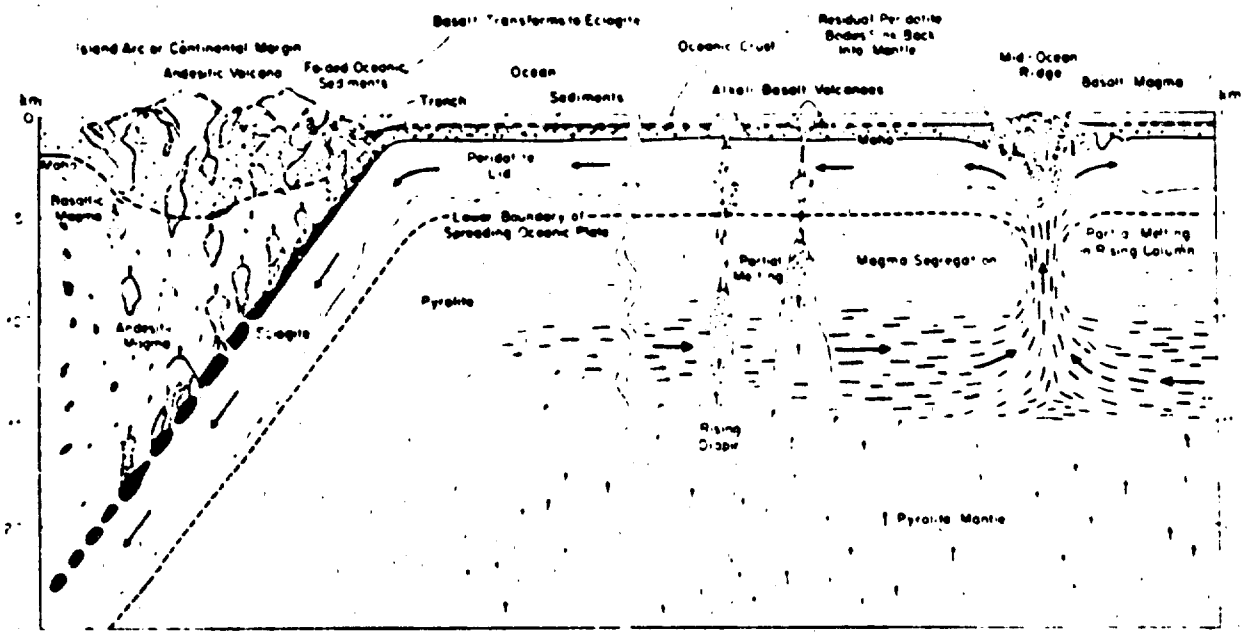


Figure 1. Generalized framework of the spreading and descending plates (from Ringwood, 1969).

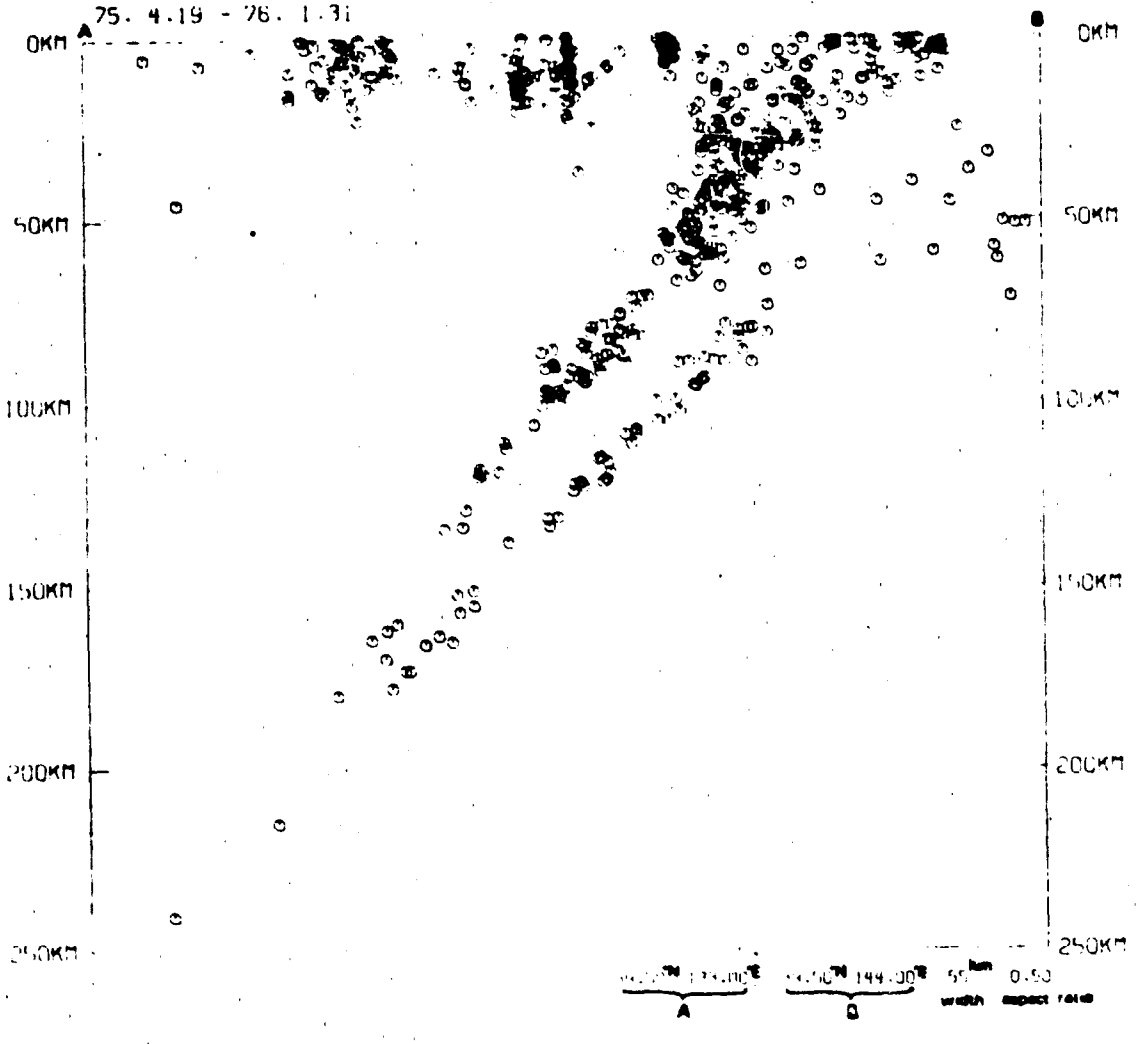


Figure 2. Two-layered deep seismic plane under the Northeast Japan Arc (from Hasegawa, Umino, and Takagi, 1976).

this region has received a significant amount of attention in the past several years, and an appropriate crust and upper mantle model can be constructed with some degree of confidence.

The most thorough study of the seismicity and structure of the Kurile Islands region was performed by Veith (1974). Veith relocated over three thousand earthquakes in the Kurile Islands using source-region/station time corrections. This permitted the determination of very precise hypocentral locations. Moreover, useful source mechanisms were determined for over four hundred of these events. This study was thus able to very clearly delineate not only both the non-laterally heterogeneous upper mantle structure in the area and the structure and velocity contrast to the downgoing slab but also the spatial variations and trends in faulting mechanism.

In Figure 3, Veith's (1974) variation of seismic velocity with depth in both the slab and the surrounding mantle is presented. The velocity contrast between the upper mantle and the descending plate ranges from about 4% at 600-700 km depth to a maximum of approximately 14% at about 200 km depth. Such a dramatic contrast does, as will be discussed in a later section, cause fairly dramatic alterations of ray paths. For shallow (less than ~100 km) depth events in the Kuriles, however, the presence of slab at depth is of little or no consequence for propagation to the proposed MSS sites. The most important model features for those cases is the rather typical oceanic structure with a well-developed lid and underlying low velocity zone. This lid structure provides a strong wave-guide

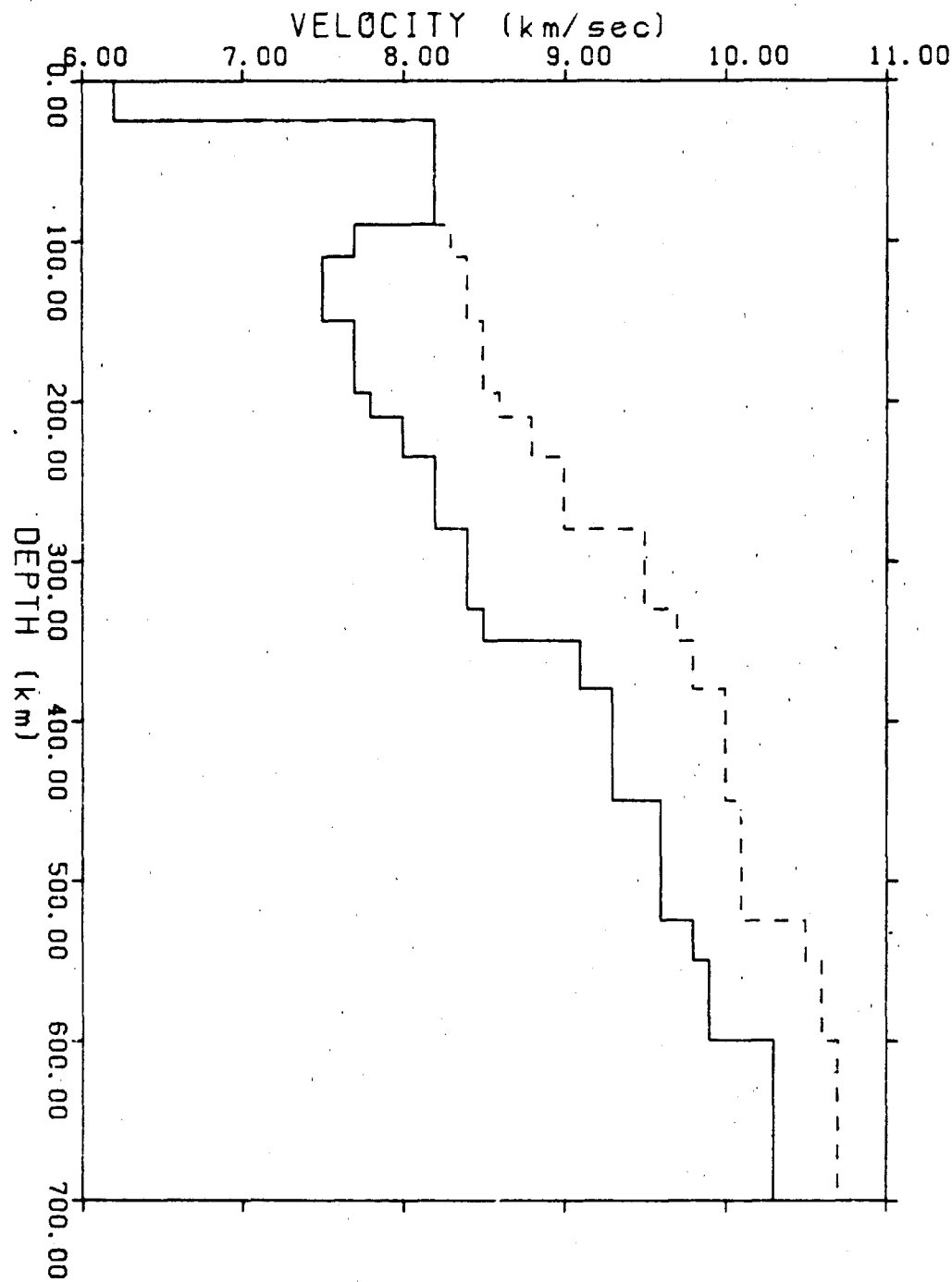


Figure 3. Compressional velocity vs. depth model for the upper mantle (solid line) and descending plate (dashed line) used in this study.

for trapped energy. Those effects are treated separately later in this report.

The slab model shown in Figure 3 is Veith's (1974) composite or average model, the dip angle of the descending slab being about 50°. The angle of descent actually varies along the trench from about 40° north of Hokkaido to about 60° under Kamchatka (Veith, personal communication). In this study, the three-dimensional slab model used has this warped configuration. In addition, the length of the slab, and, correspondingly the maximum depth attained, as defined by the observed seismicity, is also a function of position along the trench. In the shallow dipping regions at the southern extreme, the maximum depth is 350-400 kilometers; in the north, the maximum depth is about 700 kilometers. The velocity model for the warped slab, however, still corresponds to the velocity vs. depth profile shown in Figure 3.

APPROACH

The basic approach in our evaluation of the potential MSS sites in the Kuriles region has been to select a variety of representative hypocentral locations within the area and to then calculate an appropriate suite of the propagation paths from those hypocenters to the region encompassing all of the possible MSS locations east of the trench axis. This approach to ray propagation in the region was the best means to systematically analyze propagation from a large number of potential source sites to a fairly broad region in which the MSS might be located.

Seismic propagation in the region was divided into two distinct categories and different techniques were employed for each class of problems. The first grouping contains all cases in which the hypocentral location under consideration was deeper than 100 km. In such cases, the presence of the descending slab exerted a dominent propagation effect. Seismic propagation was modeled using solely three-dimensional ray-tracing methods since such deep sources are extremely inefficient in pumping trapped energy into the shallow lithospheric waveguides. The second category of problems involved locations at depths less than 100 km especially very shallow sources. These represent a very different class of propagational problems. At shallow source depths, a significant proportion of the seismic energy is trapped within the relatively efficient lithospheric waveguides. The behavior of such radiation is independent of the deep, downgoing slab effects, but is very dependent upon

frequency, fine structure (especially sediment thicknesses, and source depth). Multiply-reflected rays, head waves, and other non-geometric paths proliferate. We have employed complete generalized ray techniques to model this kind of propagation. Because of the sensitivity to fine structure, however, this part of the analysis has been conducted in only generic form. More detailed analysis can be employed for a specific path or suite of paths once a site has been selected. Three-dimensional ray-tracing analyses have also been conducted and some examples are presented for shallow sources. However, as will be seen, the basic oceanic structure in the region causes direct rays to be largely channeled out of the region of interest.

The propagational modeling presented here also includes the effects of differing radiation patterns. The study by Veith (1974) of this region was used to determine the dominant faulting types throughout the area and the resulting radiation pattern effects were convolved into our analysis. In Veith's study, five distinct types of faulting were found; transverse, shallow normal, thrust, compressional, and tensional. Transverse mechanisms occur at all depths within the plate and allow for both the differential rate of underthrusting along the trench (7.5 cm/yr in the north to 8.5 cm/yr in the south; Le Pichon, 1968) and for the warping or uneven bending of the slab. Such mechanisms comprise about 20% of the faulting overall and greater than 30% of events deeper than 70 kilometers. The events are nearly dip-slip slip with the northern segment moving down relative to the southern side. Shallow normal

faulting generally occurs only in areas of the oceanic trench. The third type of faulting, thrust faulting, is the dominent mode observed in the region comprising about 45% of all observed mechanisms. The final two types of earthquakes occur in relatively narrow zones at depth and it has been suggested that they may be related to a phase transition in the downgoing slab (Veith, 1974).

Figure 4 shows the five focal mechanisms which Veith found characteristic of the Kurile region. Shaded and unshaded areas of the hemispheres correspond to the polarity of the propagating wavefront. Rays leaving the source through the shaded regions have compressional first motions while those leaving through unshaded areas have dilatational wavefronts. The energy radiated from an earthquake source is distributed according to the radiation pattern. No energy escapes the source along nodal lines in the focal mechanism while maximum energy is radiated from the center of each region. Notice the similarity in fault orientation between the normal and thrust mechanisms and between compressional and tensional. These pairs essentially differ only by wavefront polarity which is not a necessary parameter in the calculation of radiated energy. For this reason we only consider three basic fault mechanisms in the Kuriles, with the understanding that first motions may be either compressional or dilatational for two of these mechanisms.

The most useful end product of the ray tracing modeling are spatial contours delineating the intensity of incident

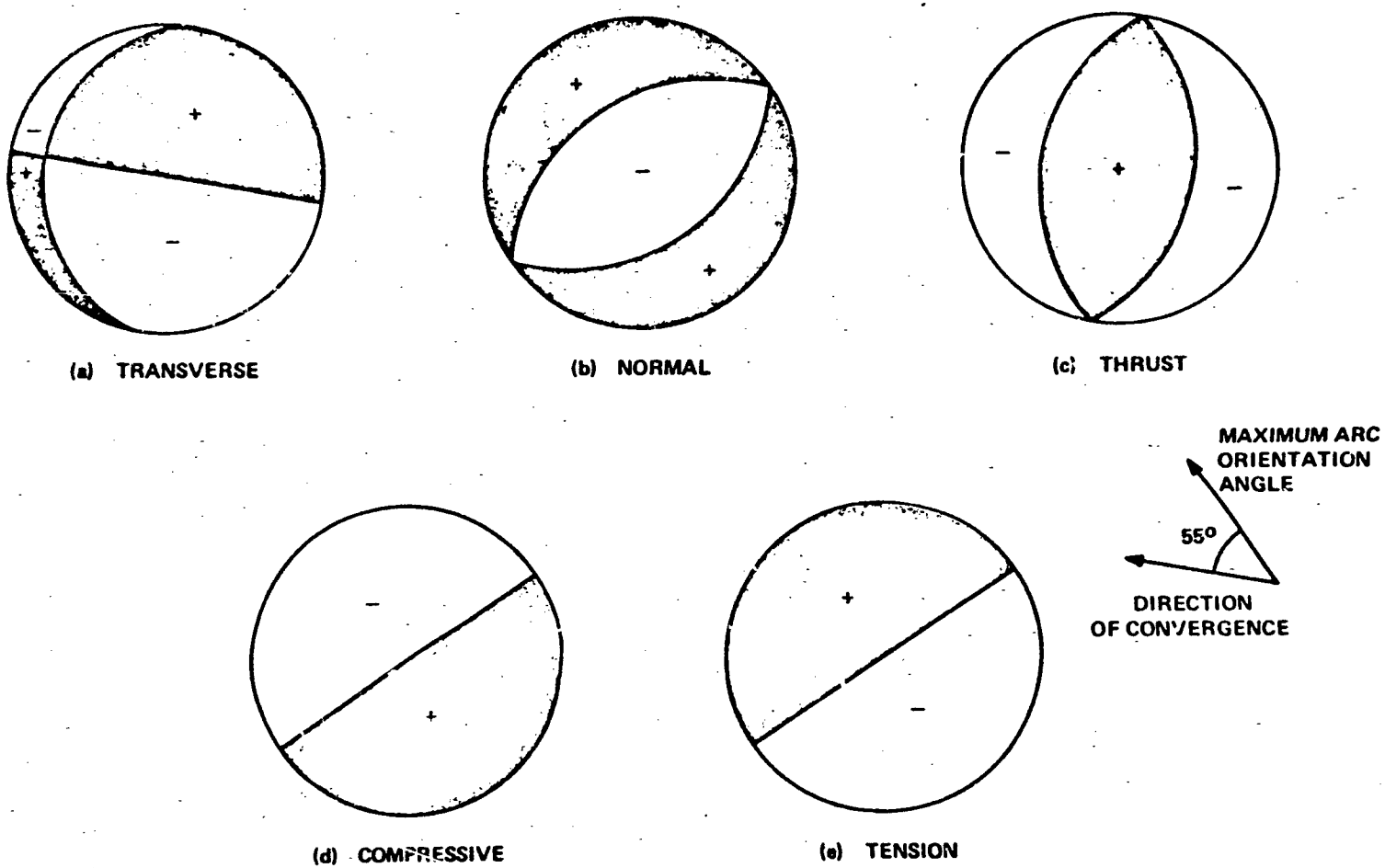


Figure 4. Lower hemisphere projections of the focal sphere for five typical Kurile sources. (Taken from Veith, 1974.)

direct arrivals, referred to as incident energy-density contours. The generalized ray calculations yield synthetic seismogram contours. Both provide useful tools for evaluating the suitability of potential station sites.

## RAY TRACING

Three-dimensional seismic ray tracing techniques have been applied in several studies of island arc regions. Jacob (1972) and Davies and Julian (1972) sought to explain anomalous travel time residuals from the underground nuclear explosion Longshot fired in the Aleutians. Large lateral variations in the upper mantle caused by a descending slab of lithospheric material severely distorted raypaths from this event. In these studies, as in ours, a regional earth model was adapted for use in a three-dimensional ray tracing code. Rays were traced through the slab model and travel-time residuals compared to those observed. In another study (Toksöz, et al., 1971), ray travel times for the Tonga-Fiji region were correlated with three-dimensional ray tracing results and theoretical travel times based on calculated temperature fields. More recent work by Engdahl (1980), has produced a highly detailed earth model of the Aleutian island arc region. Large travel-time data sets were used in conjunction with a three-dimensional ray tracing code to accurately determine the model.

Ray theory is particularly applicable to wave propagation problems involving inhomogeneous media with large linear dimensions compared to the dominant wavelengths. In such cases,

motion near a wavefront in examined and propagation may be characterized implicitly by an expanding surface $T(\bar{X},\bar{E})$, where T is the travel time between the source at $\bar{E}$ and a point $\bar{X}$ on the wavefront. The possible wavefronts are constrained by requiring that T satisfy the eikonal equation:

$$(\nabla T)^2 = 1/C^2 \tag{1}$$

where C equals the local P or S wave velocity along the wavefront. Since we are interested in tracing the surface explicitly as a function of travel time, the form $\bar{X} = \bar{X}(T)$ is more useful. Ray vectors, $\bar{S}$, are defined as normals to the wavefront, equivalent to $\nabla T$ with magnitudes equal to inverse local velocity $(1/C(\bar{X}))$ or $N(\bar{X})$, the ray slowness. From these definitions, a set of differential equations describing ray propagatio. may be expressed in Cartesian coordinates as follows:

$$d\bar{X}_i/dT = \bar{S}_i/N^2 \tag{2}$$

$$d\bar{S}_i/dT = (1/N)\ dN/d\bar{X}_i \tag{3}$$

The ray tracing code solves these equations for $\bar{X}_i$ and $\bar{S}_i$ in spherical coordinates by standard numerical methods.

The minimum requirement for a solution to the ray tracing equations is that first derivatives of $N(\bar{X})$ be continuous at each point $\bar{X}$. A cubic spline interpolation scheme was adapted for this purpose since by definition all first derivatives at $\bar{X}$ are forced to be continuous. Using this scheme, cubic poly-

nomials are fit between sampled $N(\bar{X})$ values as ray propagation progresses and spatial derivatives are calculated. This procedure poses a problem however, for accurately representing a layered earth model.

Polynomial approximations such as least squares are notorious for their resistance to bending around sharp corners, but spline approximation is especially unyielding. Step discontinuities in the data are splined together with continuous cubic polynomials producing numerous overshoots and undershoots. Layered earth models are especially prone to this error, being discrete functions with numerous discontinuous velocity steps. Figure 5 illustrates this point. Veith's original upper mantle earth model (homogeneous part) is shown here with a spline approximation curve. The large irregularities in the spline would noticeably alter ray propagation paths based on Veith's model.

Since the ray tracing code uses spline interpolation, the initial model shown in Figure 5 must be altered in such a way that when it is splined, the result matches the original model. Initially, the earth model is sampled evenly in radius (depth) every 25.93 km to a depth of 1200 km. This is a necessary formating step to prepare the model for input. Note that beyond the lower depth limit of Veith's upper mantle model an Anderson and Hart (1975) earth model is used. Ideally of course, the spline problem would vanish as the sampling increment decreased. The computational cost involved was too high to justify a densely sampled earth model. The result of

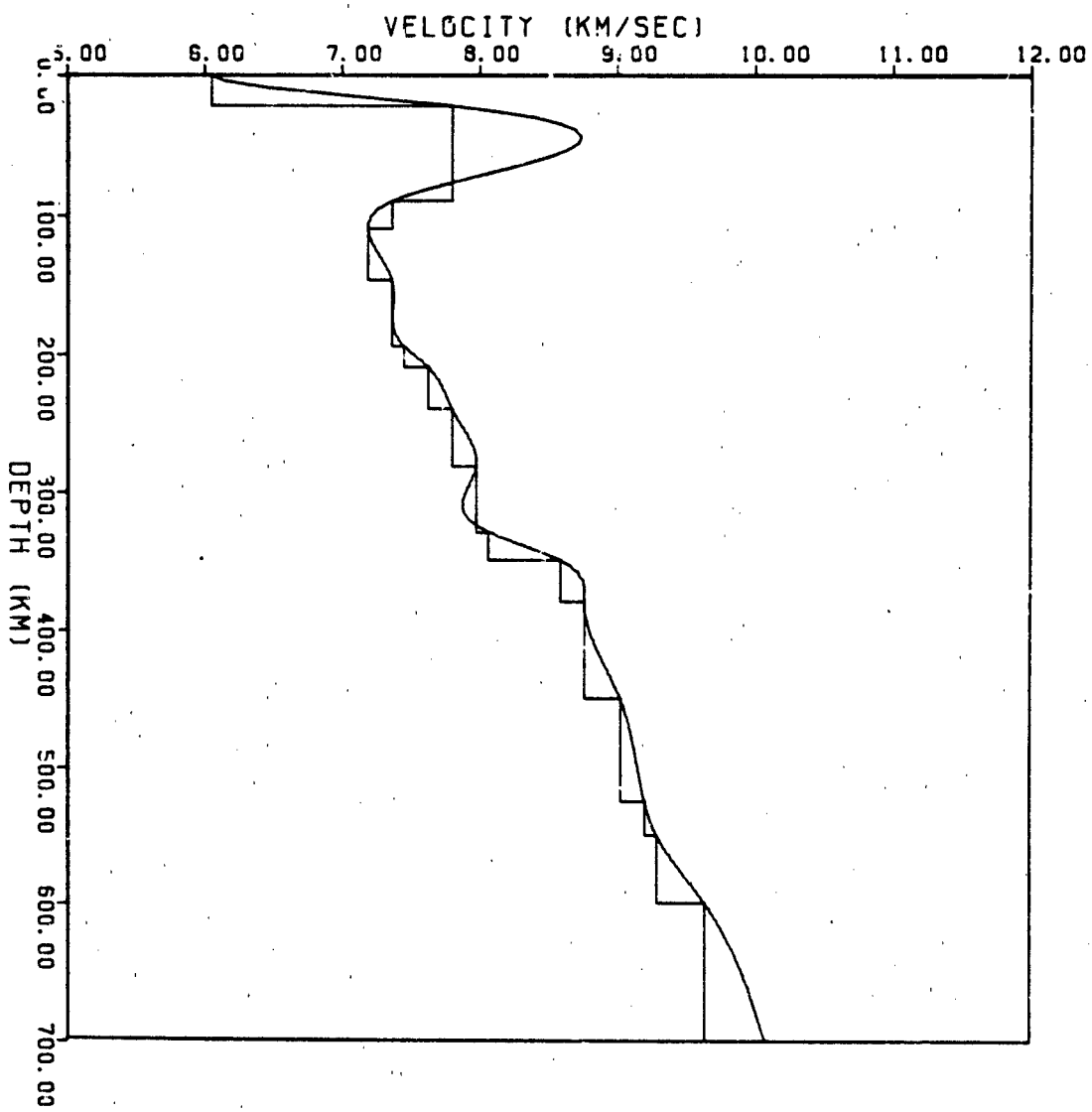


Figure 5. Veith's original upper mantle velocity profile of the Kuriles is shown here with a spline approximation curve. Step discontinuities produce large overshoots and undershoots in the spline.

discrete sampling is shown in Figure 6a and is almost identical to the original as one would expect. Next, in Figure 6b, the discretely sampled velocity structure is varied to prevent overshoots and undershoots present in Figure 6a. This spline is now representative of the original model as shown in Figure 6c. The modified velocity profile in 6b is suitable for input to the code since its spline interpolation closely approximates the initial model.

So far we have only addressed the problem of preparing the nomogeneous earth model. Heterogeneous structure is input as a perturbation to the layered earth model and a similar procedure is used to integrate the perturbation into the overall model. In this case the perturbations are modified slightly such that when added to the standard earth model the final profile is well-represented by a spline interpolation. Figure 7 shows the sampling grid used to input velocity perturbations due to the descending lithospheric slab. This portion of the model is sampled evenly in R and $\theta$, where dR is the same as before and $d\theta = 0.1214$ degrees. Perturbations are tapered to zero exponentially outside the slab and attain a maximum of 1.2 km/sec near 350 km depth. The tapering was introduced to help reduce splining errors.

The ray tracing is performed in spherical coordinates (R, $\theta$, $\phi$) with respect to a specified auxiliary coordinate system to aid in the placement of complicated structures. Inhomogeneous media are input in R, $\theta$ coordinates as perturbations of a homogeneous earth model $C(\bar{X})$. These may be discrete or

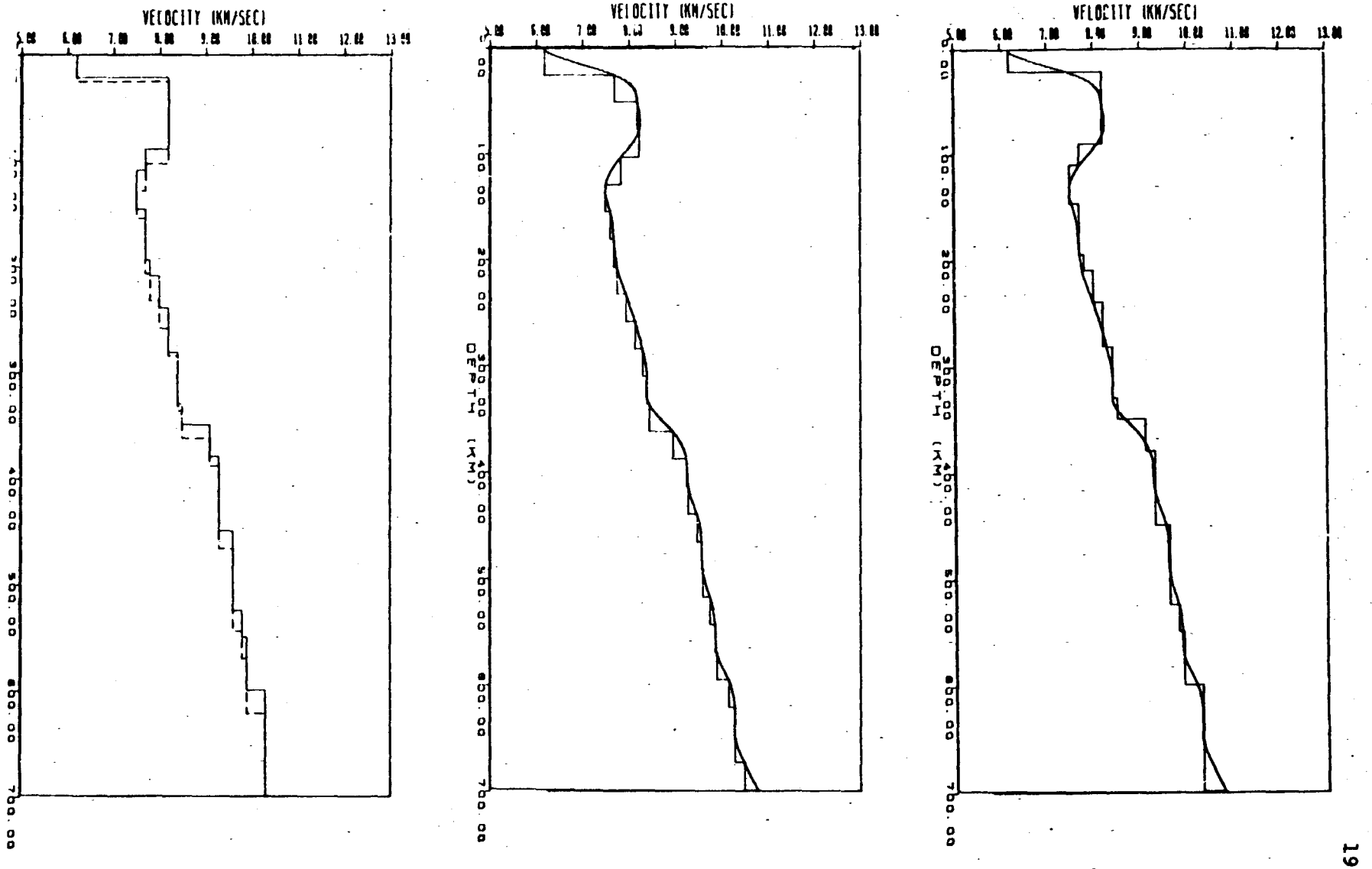


Figure 6. The evenly sampled (dR≅25Km) version of Veith's velocity profile is shown in 6a (dotted line) next to the original. Fig. 6b illustrates how small modifications to this model prevent overshoots from splinning. Finally, the spline curve from 6b is shown in 6c overlaying the original model. Since the ray tracing code used spline interpolation, the modified profile (6b) is input.

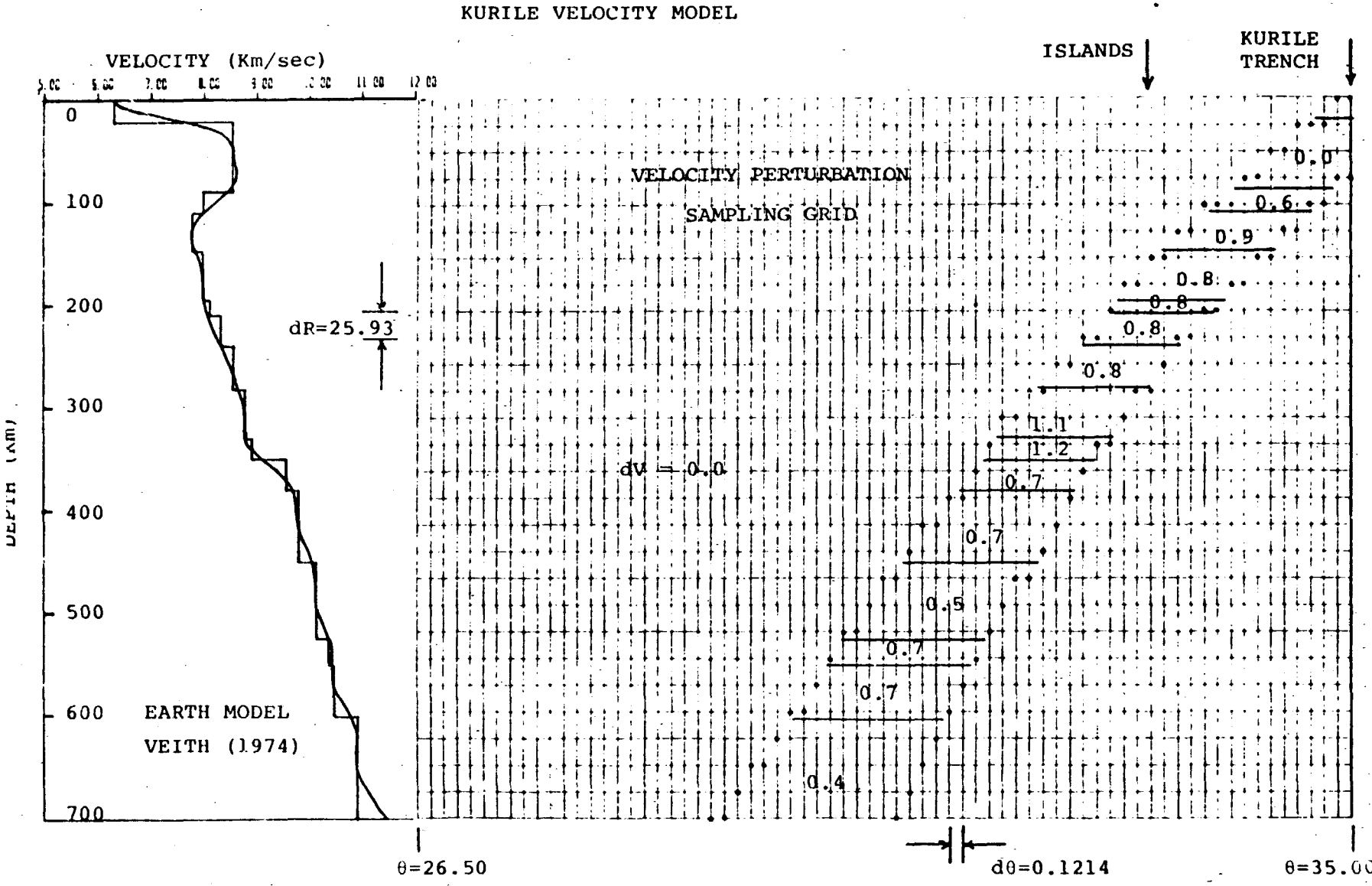


Figure 7a. Veith's original velocity profile was developed from examining over 3,000 relocated earthquakes in the Kurile Islands. The curve overlay is a functional approximation used in the ray tracing code.

Figure 7b. The velocity perturbation sampling grid is shown here with the actual values of dV specified within the descending slab. The velocity perturbation was zero outside this region. Below 700 km an Anderson and Hart earth model is used.

functional representations. The perturbed two-dimensional region is then extended along the $\phi$ axis and tapered at specified end points to generate a three-dimensional structure. The region must therefore have a standard cross-section with respect to the $\phi$ coordinate.

A generalized coordinated system is initially defined by Eulerian rotation angles (e.g., Goldstein, 1950). The Euler angles $\theta_p$, $\phi_p$, and $\psi_p$ specify a series of three rotations from an initial system of axes, X, Y, Z, to a new system, $X_p$, $Y_p$, $Z_p$, and should not be confused with the spherical coordinates R, $\theta$, and $\phi$. In this case the initial axes correspond to geographic coordinates with the positive Z axis at 90° North latitude (north pole) and the positive X axis at 0° longitude on the equator. $\theta_p$ is then the angular distance between the Z and $Z_p$ axes. $\phi_p$ specifies a counterclockwise rotation of the X axis to a new position E in the X-Y plane. $\psi$ is the angular distance between $X_p$ and E subtended from a counterclockwise rotation in the $X_p$-$Y_p$ plane. Figure 8 shows the generalized coordinate system used to model the Kurile subduction zone.

Veith's velocity profile of the Kurile region is represented as described previously, in discrete form as a function of R and $\theta$. Since this is an average model it is valid as a first approximation at every point along the arc. Choosing the trench axis as a reference line, we would like the coordinate $\theta$ to be constant along this line in order for any cross-section of the region to have identical velocity profiles when the model is extended to three dimensions. This places a constraint on the auxiliary pole location $Z_p$.

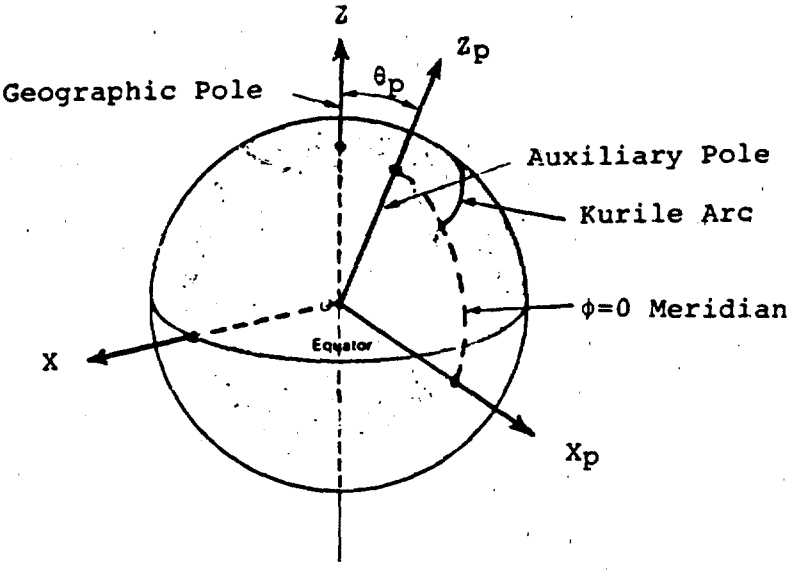


Figure 8. Ray tracing is performed in spherical coordinates $(R, \theta, \phi)$ with respect to an auxiliary coordinate system $(X_p, Y_p, Z_p)$. Rotation from a geographic system $(X, Y, Z)$ is specified by the Euler angles $\theta_p$, $\phi_p$, and $\psi_p$. The Kurile-Kamchatka arc is placed into this auxiliary system by requiring the pole $Z_p$ to be equidistant from all points on the arc. In addition, the prime meridian ($\phi$=0 line) is oriented to intersect the arc's southern-most extension.

The Kurile-Kamchatka arc was placed into the auxiliary coordinate system by requiring the pole $Z_p$ to be equidistant from all points on the trench axis. To accomplish this, the angular distance to the pole was varied until a best fit to the trench axis was found. Davies and Julian (1972) placed the Aleutian arc by the same technique finding that 10° was an optimal polar angle. In our case, a polar distance of 35° fit the data to within an average error of 0.10°. The following is a list of 7 trench axis points and their corresponding angle to the auxiliary pole $Z_p$:

| Latitude | Longitude | Angle | |
|---|---|---|---|
| 42.7N | 148.4E | 34.98 | |
| 43.6N | 150.0E | 35.07 | |
| 45.0N | 152.4E | 35.18 | |
| 47.N | 155.0E | 35.00 | (reference) |
| 48.6N | 157.0E | 34.84 | |
| 50.5N | 160.0E | 34.98 | |
| 52.8N | 162.4E | 34.60 | |

The actual location of the $Z_p$ axis (pole) in geographic coordinates is 61.18° N and 97.86°E. The prime meridian in this coordinate system intersects the southern most point on the Kurile trench axis. Hence, the azimuthal angle $\phi$ equals 0.° at this point. Since the Kurile arc is approximately 25° long and 8.5° wide, the regional model is defined for $\theta$ = 26.5° to 35° and $\phi$ = 0°-24°. The maximum depth of the lateral heterogeneity is 700 km.

The velocity profile determined by Veith (Figure 7) is an average model of the region. In reality, the dip angle of the slab is known to vary by 20° from north to south. In order to incorporate this feature into our model, the velocity profile

of the slab was made functionally dependent or R and $\phi$. At the extreme southern end of the trench, where $\phi = 0.°$, the dip angle was set to 40° by shifting the original perturbations. The shifting function varies dip angle continuously up to 60° at the northern most point of the trench. Northern and southern cross-sections of the warped slab model are shown in Figure 9. Velocity contour lines are drawn every 0.5 km/sec from 11.50 km/sec just above 1200 km. The obvious area of discontinuity outlined here corresponds to the descending slab.

Full three-dimensional variance of the model was accomplished by functional manipulations of a standard cross-section. This technique may be applied to almost any complicated structure given some fundamental profile. The ability to rotate the coordinate system also aids in placing structures as we have shown for the Kurile arc. Together, these two features make this ray tracing code a powerful tool in geophysical research.

To fully appreciate the three-dimensional nature of the slab models, a radial velocity contour map was constructed. Figure 10 shows the regular and warped slab models respectively at four depths. Each contour separates differing velocity regions, thus outlining the descending slab.

Utilizing the ray tracing techniques described above, incident energy density contour maps have been constructed in the Kurile region based on data collected from rays propagated through the warped slab model. Sources for these rays were selected to sample local seismicity data as previously discussed and the three basic focal mechanisms selected were thrust,

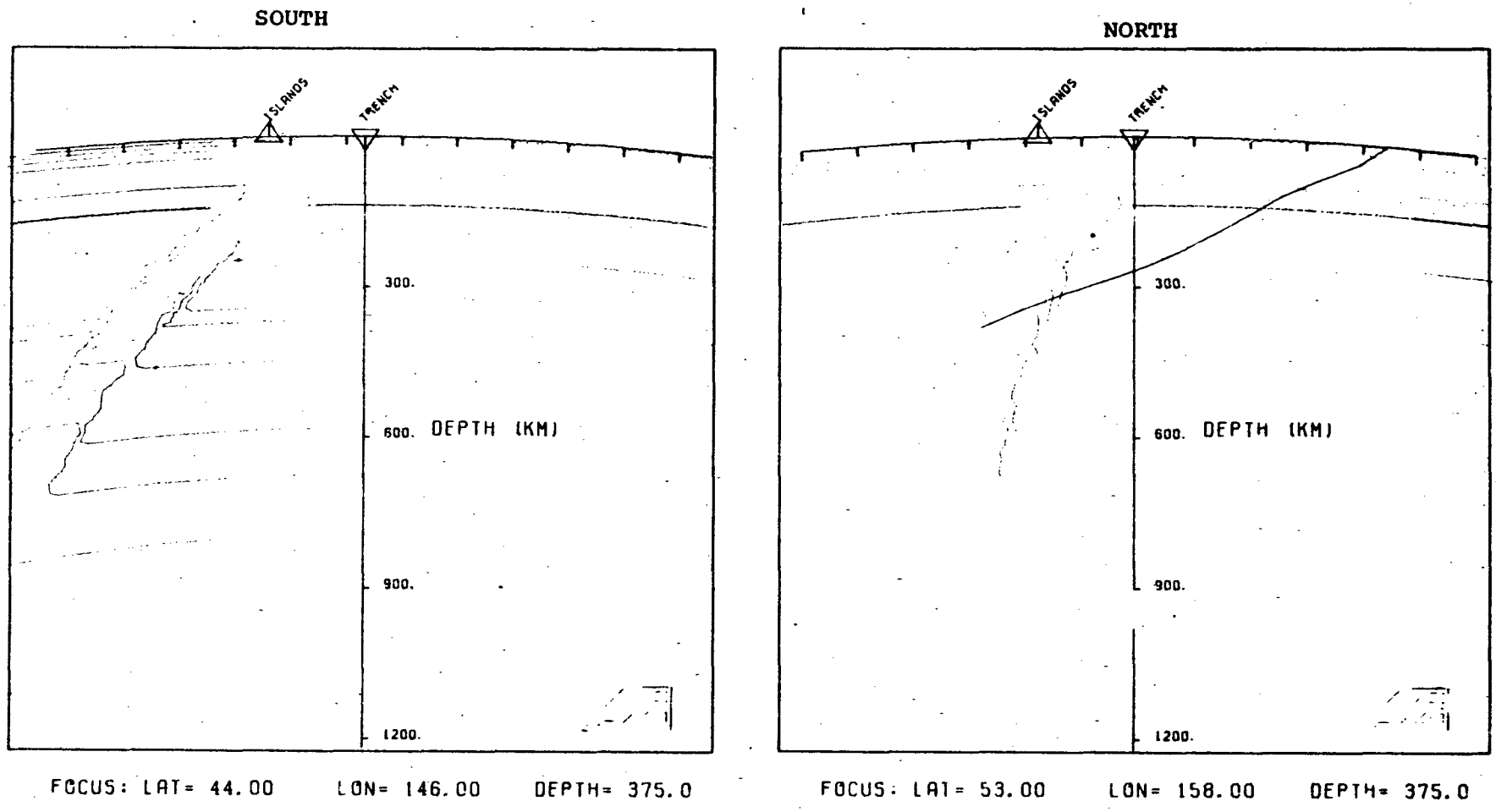


Figure 9. Northern and Southern cross-sections of the warped slab model illustrates the extent to which dip angle changes along the arc. A continuous shifting function was applied to the original perturbation model to represent this feature.

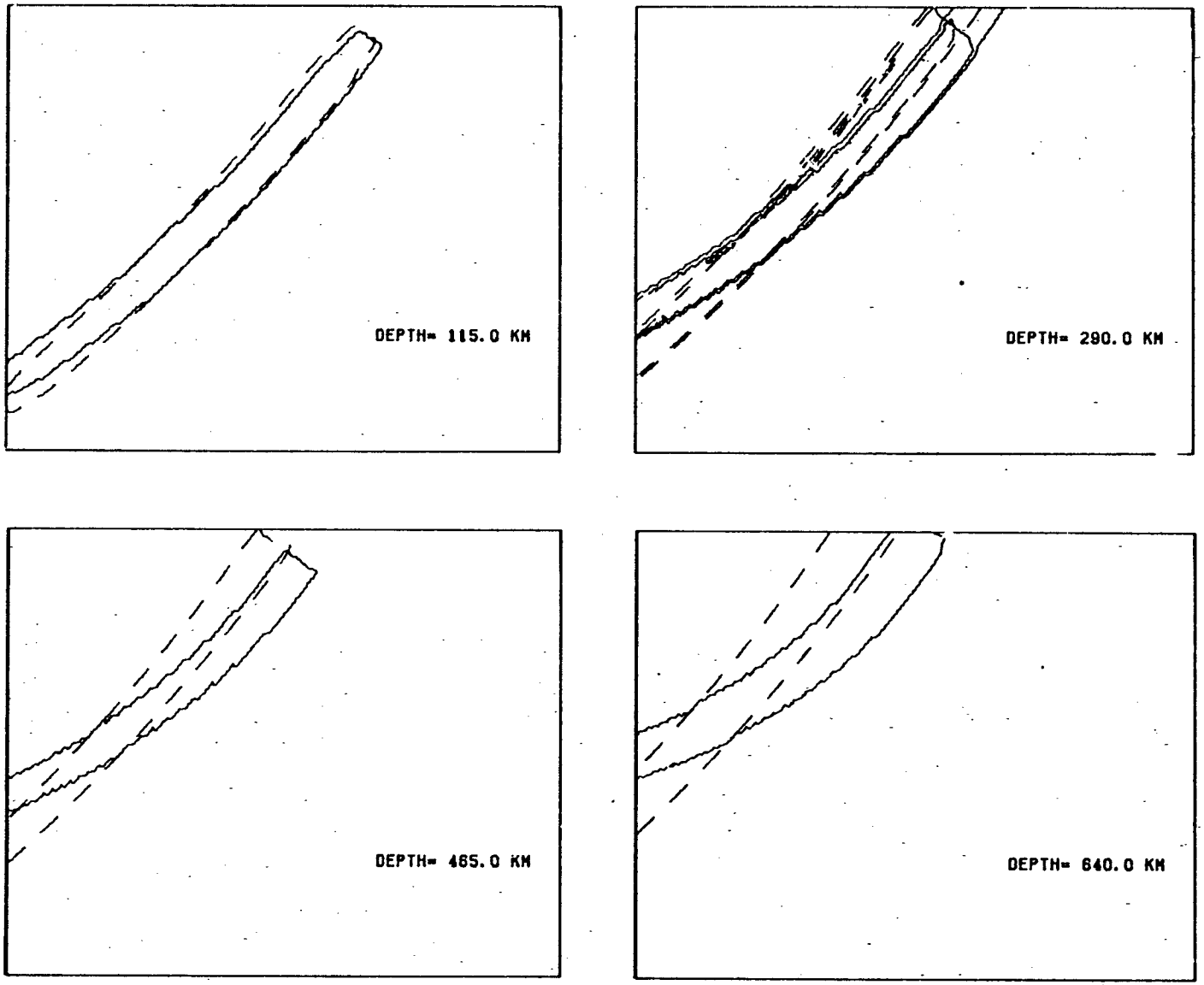


Figure 10. Radial cross-sections of the regular (dotted line) and warped slab models at four depths. Velocity contours outline the slab's position, varying from 8.0 km/sec at 115 km to 10.5 km/sec at 640 km.

transverse, and compressional. Relative energy of a seismic ray depends significantly on both source radiation pattern and geometrical spreading.

In a homogeneous earth, the geometrical spreading correction is a simple function $G(\Delta)$ where $\Delta$ is the angular distance between the epicenter and ray emergence point. The structural complexity of the Kurile subduction zone however, produces anomalous focusing and defocusing of rays which distort normal spreading. Corresponding irregularities in energy density ($E(\Delta)$) are produced at the surface as a function of both $\Delta$ and azimuth. In fact, $E(\Delta)$ varies proportionally to $\delta e_1/\delta\Delta$ where $e_1$ is the emergence angle at the source. The exact relation is given by Bullen (1965):

$$E(\Delta) = (I/R_o^2)*(\cos(e_1)\ /\sin(\Delta)*\sin(e_o))*|\delta e_1/\delta\Delta| \qquad (4)$$

where $R_o$ equals the earth's radius, I is the energy per unit solid angle emitted from the source, $e_o$ is the emergence angle at the surface, and $\Delta$ is the angular distance between the epicenter and ray emergence point. $E(\Delta)$ is then the energy per unit area of the portion of the wavefront emerging at angle $e_o$. For computational ease, the derivative $\delta e_1/\delta\Delta$ is determined discretely.

In our modeling, rays were emitted from the sources at a constant increment of take-off angle (usually 2.00°), hence $\delta e_1$ is a constant. As a result, the energy relation is most dependent on $\delta\Delta$ which is always changing. Where ray focusing occurs the change in $\Delta$ is small thus raising the incident energy-density. These areas are known as "bright spots" or caustics in the case of perfect focusing.

Having once specified a source mechanism by the fault plane orientation (dip, strike, and rake), a quadrupole radiation pattern is determined. Rays exiting the source have relative energies corresponding to their angle and azimuth of departure. Energy variation from radiation pattern is a straightforward calculation (Langston and Helmberger, 1975) and the resulting value for each ray may simply be multiplied by $E(\Delta)$. Radiation values vary between a minimum of 0, for rays exiting along nodal planes, and a maximum of inverse source velocity squared. Polarity of the wavefront is indicated by the sign of the radiation value.

Extensions to the ray tracing code originally developed by Bruce Julian in 1974 make it possible to calculate regional energy density given an appropriate earth model. In this case Veith's model of the Kuriles is adapted for input to the code and surface energy density maps constructed to the southeast of the island arc.

Five source regions, coded KAn-KEn, were examined at varying depths along the slab. Depths are numerically coded with n = 1 corresponding to the shallowest source at 150 km, and n = 2, 3, and 4 corresponding to progressively deeper hypocentral locations. Figure 11 illustrates the epicentral locations of the source regions used in this phase as well as the four proposed MSS sites. Rays from these sources were traced into a region which enclosed the four proposed OBS sites by specifying hypocenter location and propagation direction. More specifically, rays were shot from each of 16 total sources in 2.0° degree intervals

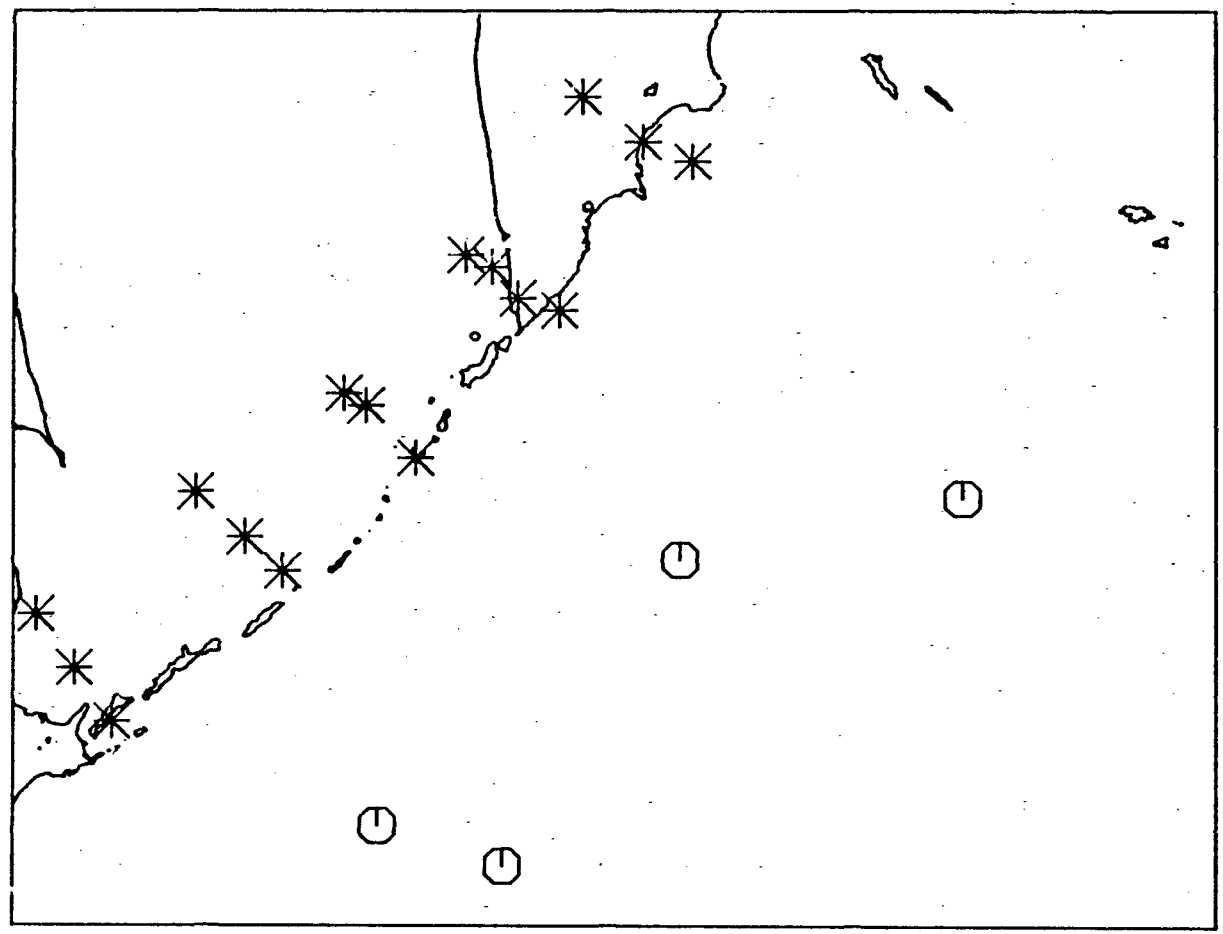

Figure 11. Map of the Kurile Islands/Kamchatka region showing the proposed MSS sites (circles) and the epicenters of the 16 sources (stars) used in the energy-density calculations. The variable dip in the slab model causes the irregularity in epicentral locations.

of take-off angle and 4.0° intervals of azimuth into this area. In most cases at least 400 rays were necessary for adequate coverage of the region.

Since the earth model is fully three-dimensional, rays were not just refracted within their initial departure plane. Many raypaths were forced out of the plane by the velocity structure producing unique focusing effects at the surface. Figures 12a and 12b are cross-sections of the earth model showing numerous raypaths from sources KD4 and KC2 respectively. Rays bending out of the plane here are projected into the initial ray departure plane. Tick marks on the surface are at 1° intervals and the depth is given in kilometers. An outline of the slab is produced by plotting velocity contours every 0.5 km/sec as was done in Figure 9. Note the increasing distortion in the raypath as the rays strike the slab-earth interface at increasingly oblique angles in 12a. The refraction of these rays is governed simply by Snell's Law. In the case of 12b we see that a low velocity zone at 150 km is actually trapping rays by bending them away from the interface as they strike a higher velocity medium above. Raypaths in Figure 12b are severely distorted by the structure causing shadow zone formation just beyond the trench axis.

As source locations approach the surface, the low velocity zone traps an increasing number of rays, producing an 8° wide shadow zone southeast of the trench axis. Figure 13 is a cross section of these raypaths from a surface focus event. The take-off angle increments have been made very small in

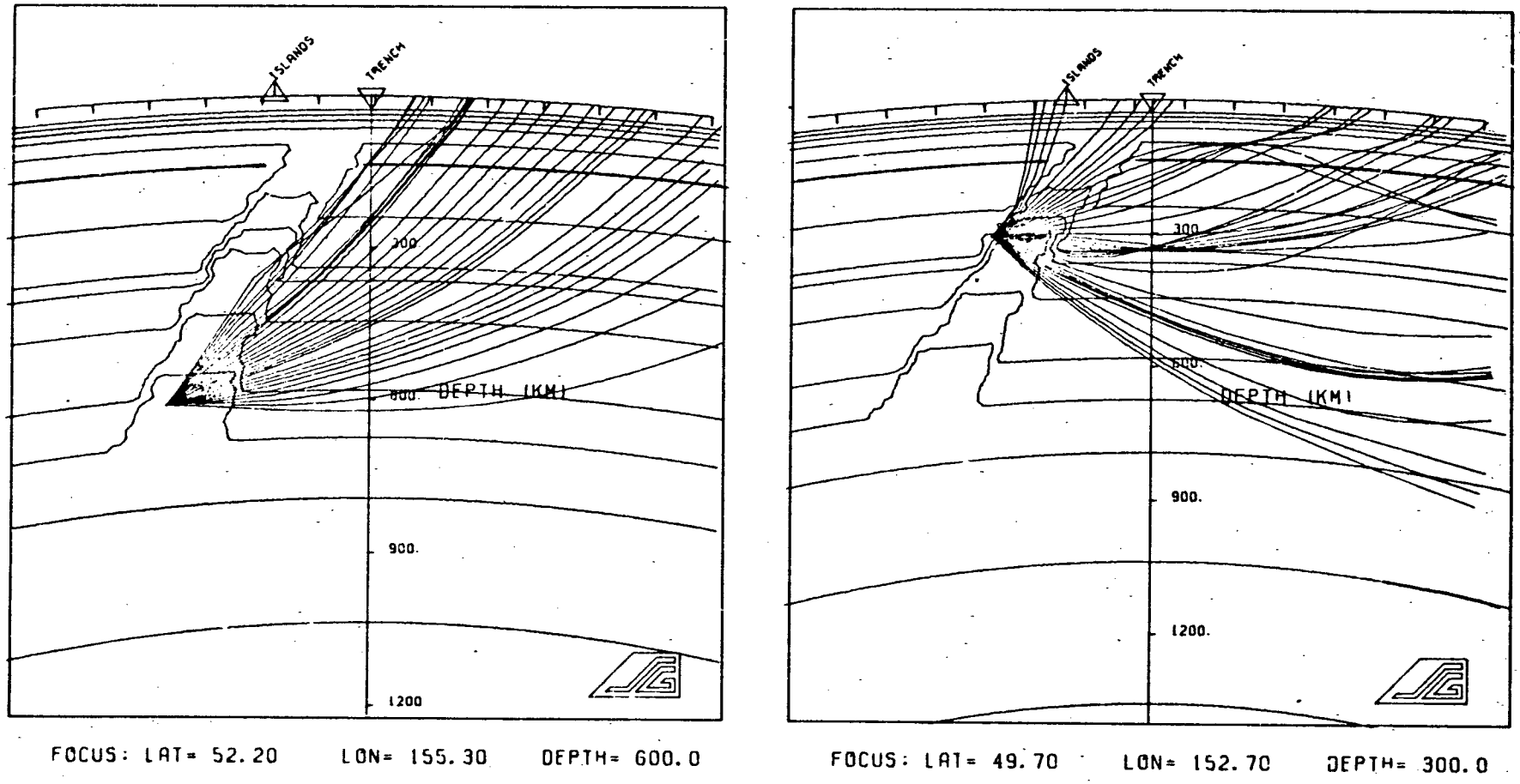


Figure 12. Cross section of seismic ray propagation from sources at 600 km and 300 km depth through a three-dimensional model of the Kurile subduction zone. Velocity contours are drawn every 0.5 km/sec from 6.5 km/sec near the surface.

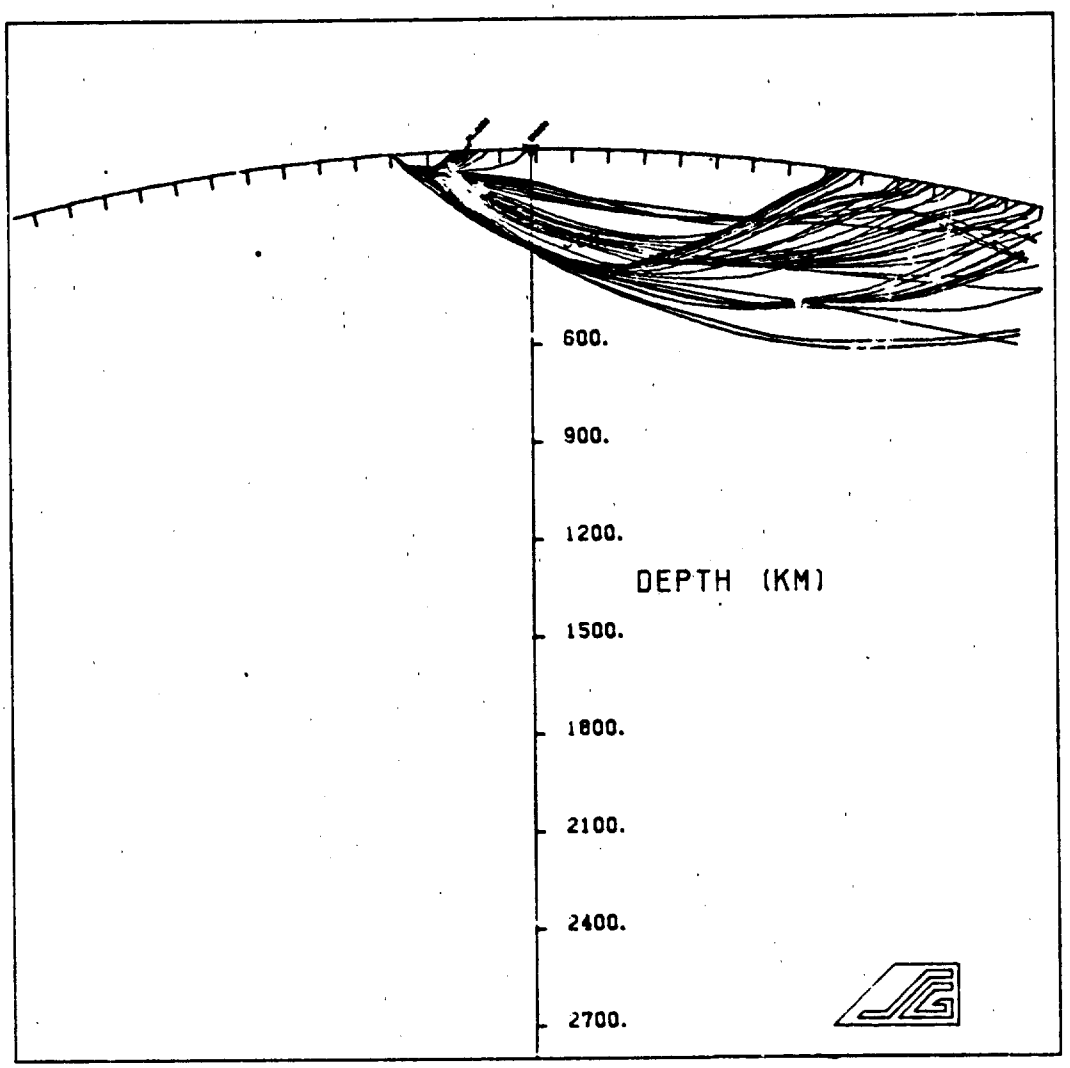


FOCUS: LAT=: 55.000 LON= 160.000 DEPTH= 0.0

Figure 13. Cross-sectional map of raypaths from a surface focus event in Kamchatka. A 10° shadow is produced by an upper mantle low velocity zone.

order to show more detail. The implication, of course, is that direct seismic arrivals from very shallow sources will be low amplitude, long period signals at any of the proposed sites. A treatment of this problem using full Cagniard methods is presented later.

Figures 14a and 14b present one mode of analyzing the ray tracing results. In these figures, the locus of emergence of each ray is plotted as a small vector. The vectors indicate the apparent back azimuth of each ray as determined by the angle of emergence. There are several interesting features of the propagation which become apparent in these figures. In Figure 14a, the hypocenter is located at a depth of 600 km near the northern terminus of the trench. The radical bending of some rays from this location can be seen rather dramatically in the area directly east of the epicenter where the apparent back azimuth is rotated as much as 180° from the true back azimuth. In Figure 14b, another effect, that of horizontal caustics, is illustrated from an event near the southern end of the trench. This caustic can be seen in the curving, increasingly dense pattern of arrivals from the southeast.

Although the presentation in Figure 14 can yield interesting and important information, it suffers the limitation of being a discrete, pointwise representation of the data. This limitation has been surmounted through the implementation of the incident energy-density contouring described earlier. Figures 15 through 30 show the incident energy-density distributions from the 16 hypocentral locations shown in Figure 12. Each figure

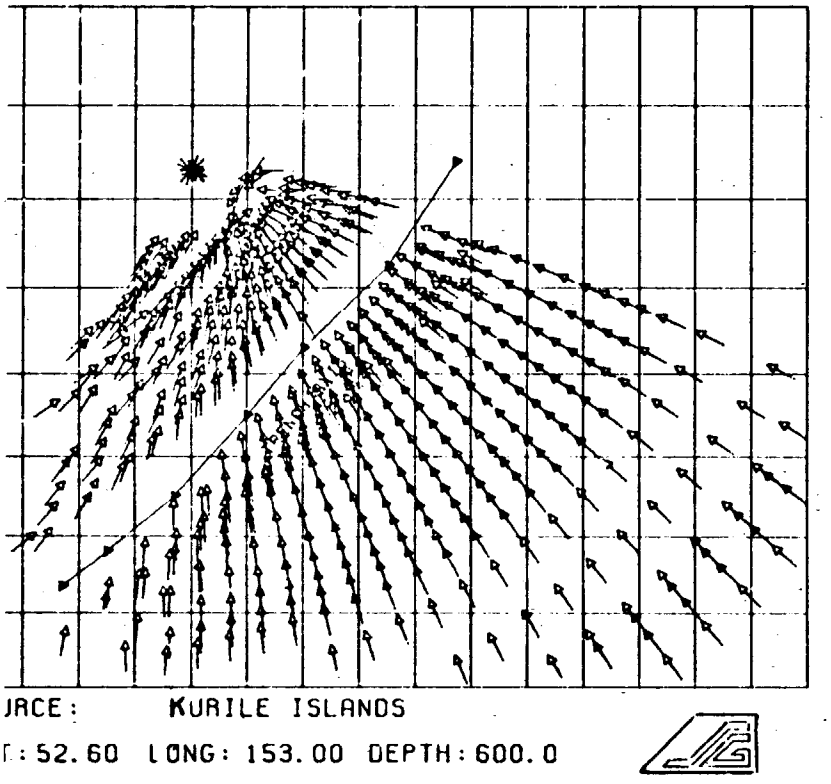


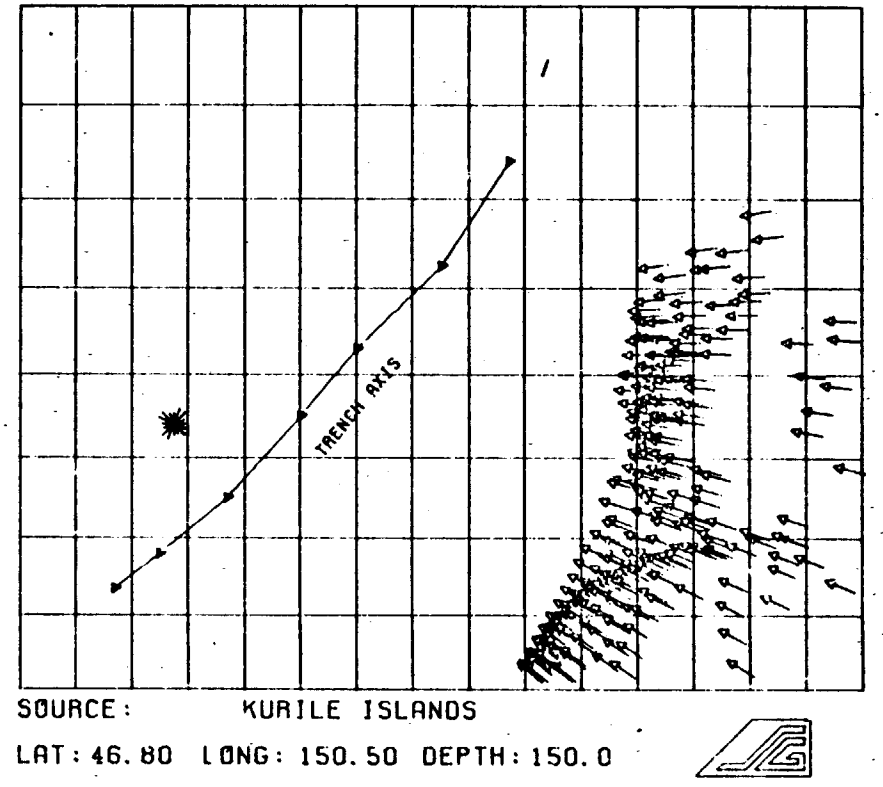


Figure 14. Surface maps of ray emergence points for two Kurile sources. Arrows indicate emergence azimuth. Structural interaction anomalously bends rays around and produces unusual focusing effects.

in this group is a composite of four individual plots. In the lower left, a back-azimuth vector plot of the type shown in Figure 14 is displayed for an explosion source (no radiation pattern). In the upper left, upper right, and lower right quadrants of each figure are the energy-density plots for the same hypocentral location but with the radiation patterns convolved into the result. These radiation patterns are indicated by the focal spheres illustrated in each plot. For clarity, the contours are illustrated in color. Changes in color from blue to green to red to yellow indicate decade changes in incident energy. Blank or uncolored zones indicate either complete shadow zones or regions not included in the calculation. The proposed MSS sites as well as the locus of the Kamchatka peninsula and Kurile Islands have been plotted on a transparent overlay for use with these figures (see pocket, inside back cover). In all cases, the propagational effects due to the downgoing slab dominate the broad features of the incident energy. The detailed distribution of relative energy is, however, more sensitive to the assumed radiation pattern of the source. It should be noted that the energy density levels are not normalized by figure but rather all figures are plotted on the same intensity scale.

It is also possible to utilize this ray tracing approach to analyze potential problems in source mechanism studies. Due to the extreme lateral refractions in this structure, nodal planes are often not clearly resolved. This result is implied from Figures 15-30. In these figures, it is at best

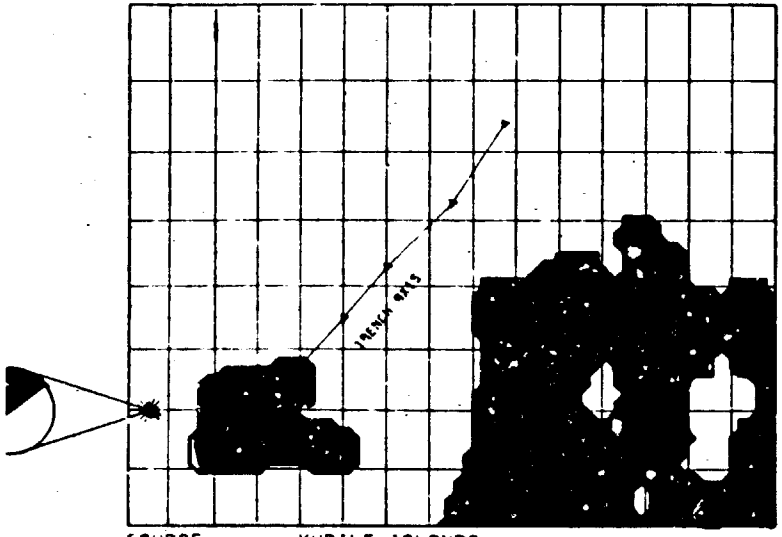


SOURCE: KURILE ISLANDS

LAT. 44.00 LONG: 146.00 DEPTH: 150.0

STRIKE: 53.0 DIP: 90.0 RAKE: 90.0 VSRC: 8.39

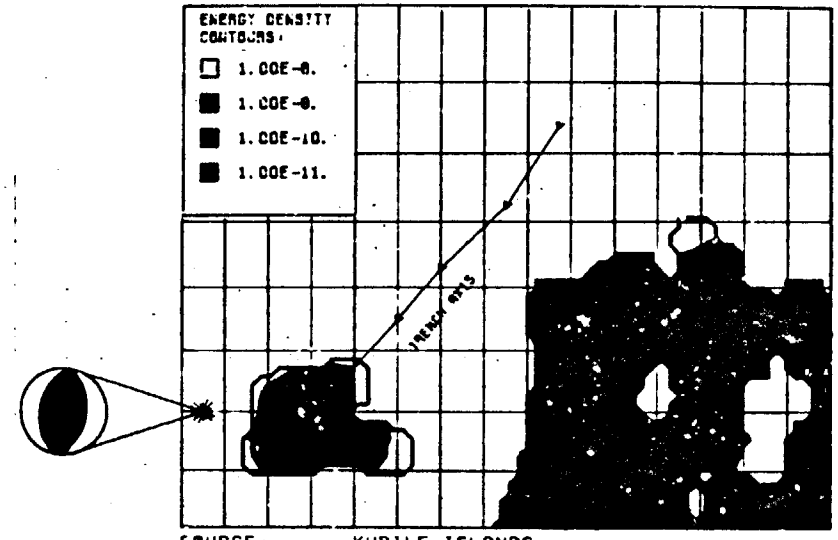


SOURCE: KURILE ISLANDS

LAT. 44.00 LONG. 145.00 DEPTH: 150.0

STRIKE: 10.0 DIP: 45.0 RAKE: 90.0 VSRC: 8.39

SOURCE: KA1

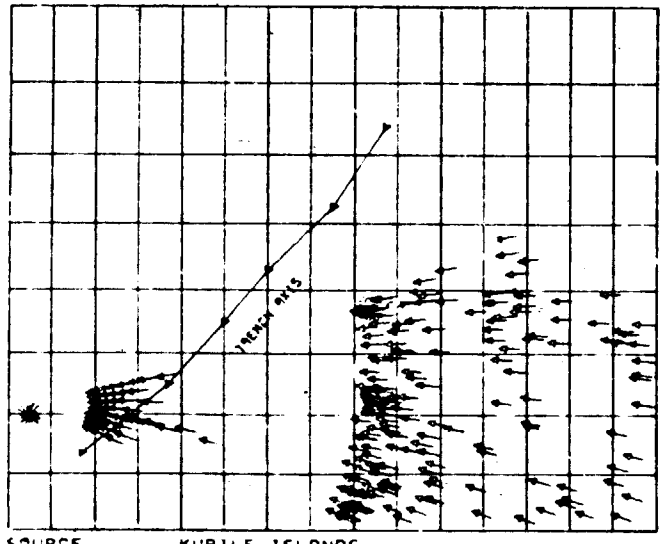


SOURCE: KURILE ISLANDS

LAT. 44.00 LONG. 146.00 DEPTH: 150.0

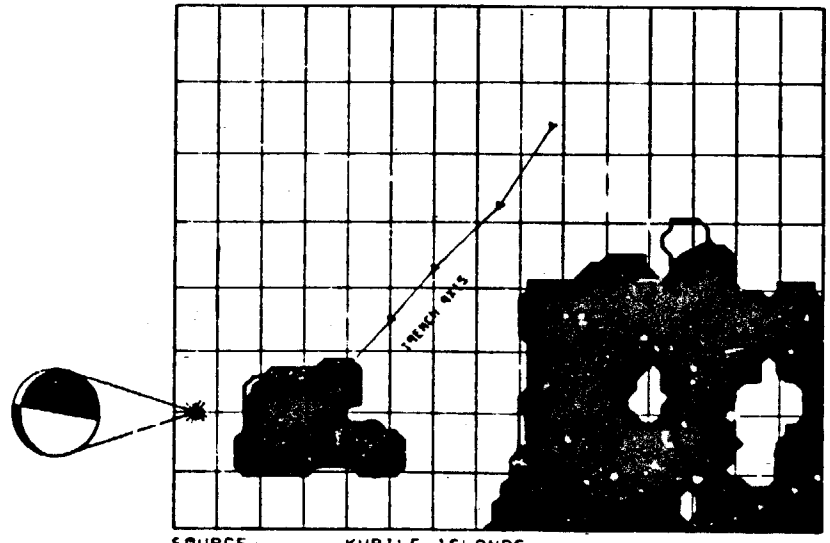


SOURCE: KURILE ISLANDS

LAT. 44.00 LONG. 146.00 DEPTH: 150.0

STRIKE: 100.0 DIP: 90.0 RAKE: 110.0 VSRC: 8.39

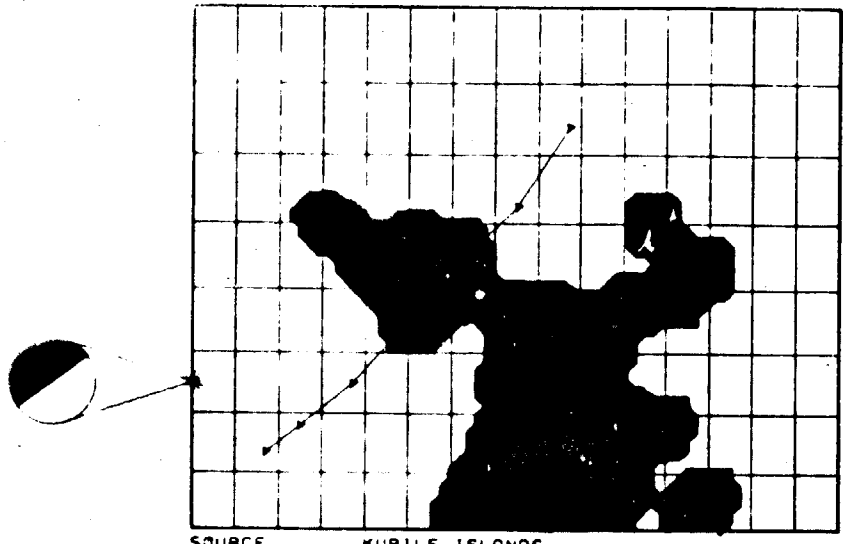

SOURCE KURILE ISLANDS
LAT. 45.00 LONG. 145.00 DEPTH. 225.0
STRIKE. 53.0 DIP. 90.0 RAKE 90.0 VSRC .8.59

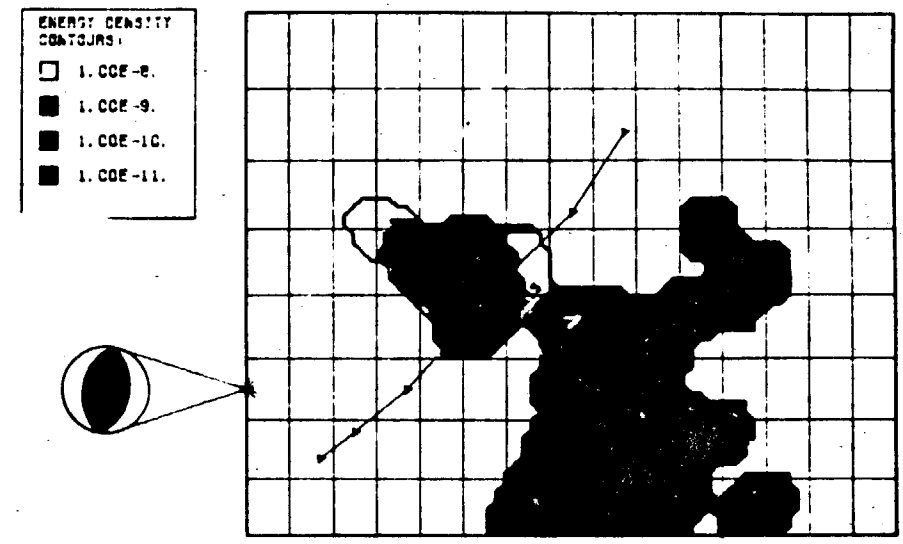


SOURCE: KA2

SOURCE. KURILE ISLANDS
LAT. 45.00 LONG. 145.00 DEPTH. 225.0
STRIKE. 10.0 DIP. 45.0 RAKE 90.0 VSRC .8.59

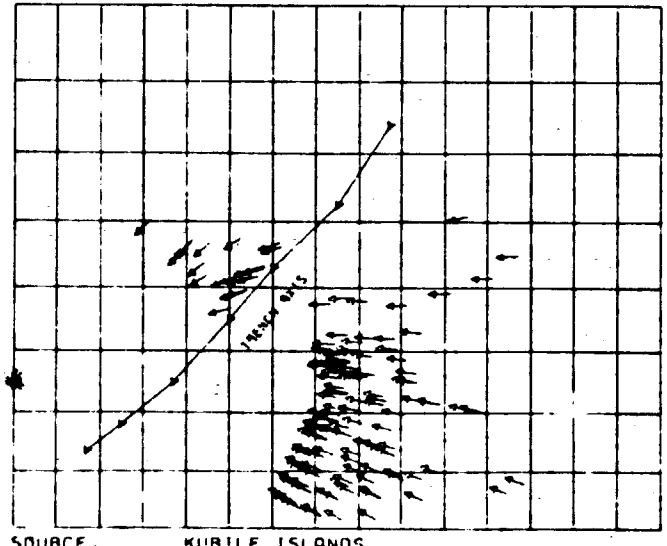

SOURCE. KURILE ISLANDS
LAT. 45.00 LONG. 145.00 DEPTH. 225.0

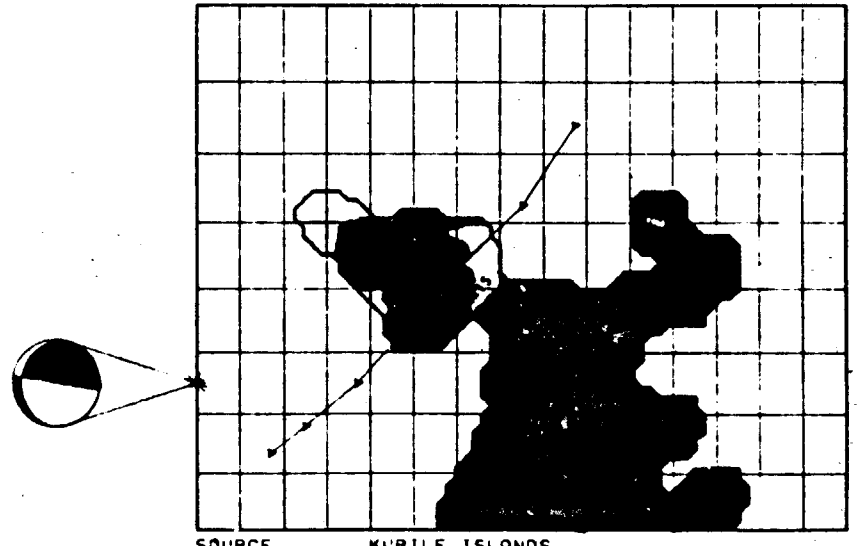

SOURCE. KURILE ISLANDS
LAT. 45.00 LONG. 145.00 DEPTH. 225.0
STRIKE. 100.0 DIP. 90.0 RAKE 110.0 VSRC .8.59

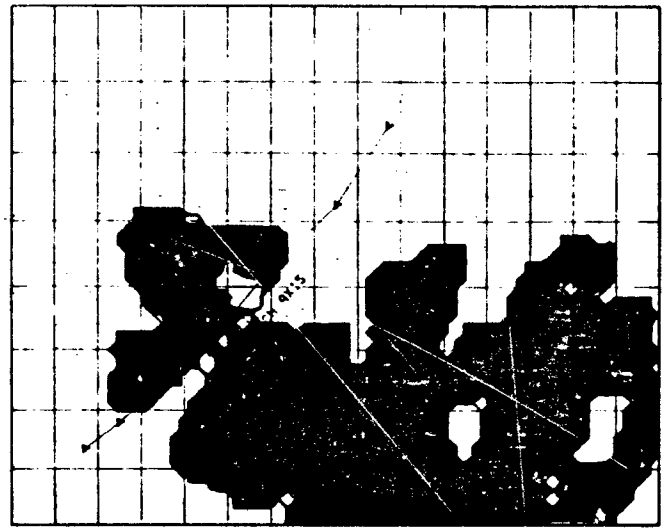


SOURCE: KURILE ISLANDS
LAT: 46.00 LONG: 144.00 DEPTH: 375.0
STRIKE: 53.0 DIP: 90.0 RAKE: 90.0 VSRC: 9.80

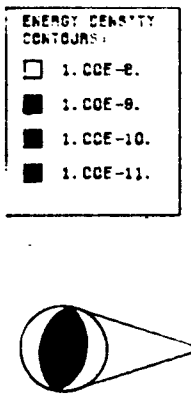


SOURCE: KA3

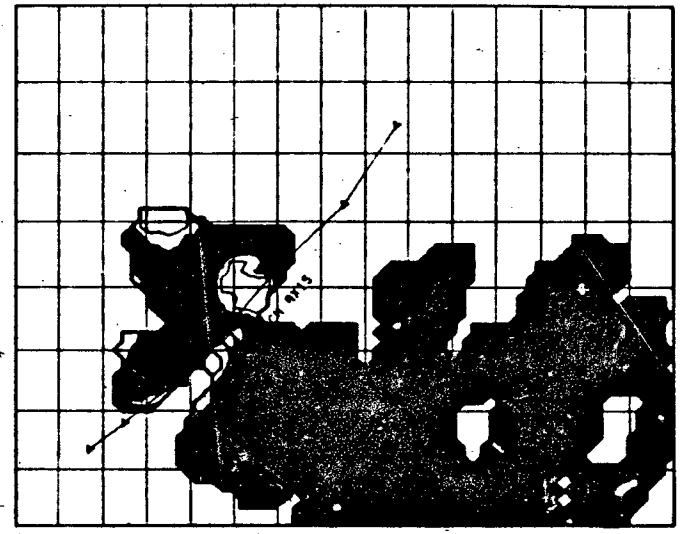


SOURCE: KURILE ISLANDS
LAT: 46.00 LONG: 144.00 DEPTH: 375.0
STRIKE: 10.0 DIP: 45.0 RAKE: 90.0 VSRC: 9.80

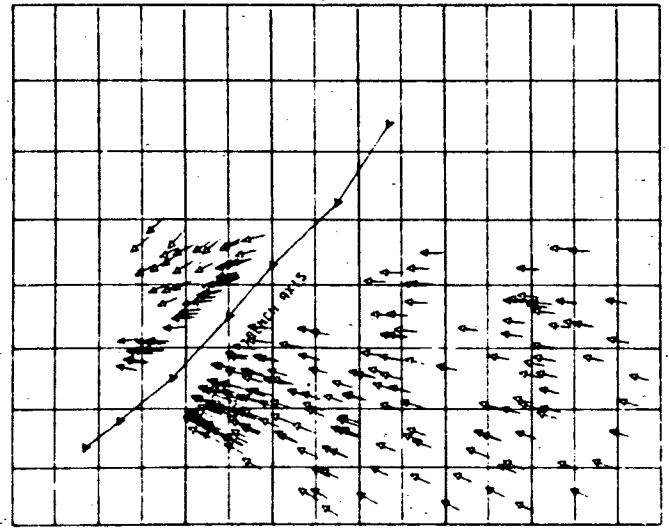


SOURCE: KURILE ISLANDS
LAT: 46.00 LONG: 144.00 DEPTH: 375.0

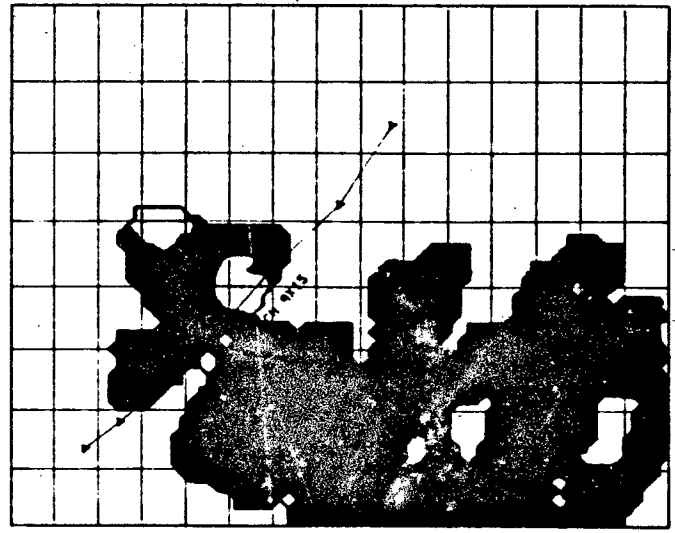


SOURCE: KURILE ISLANDS
LAT: 46.00 LONG: 144.00 DEPTH: 375.0
STRIKE: 100.0 DIP: 90.0 RAKE: 110.0 VSRC: 9.80

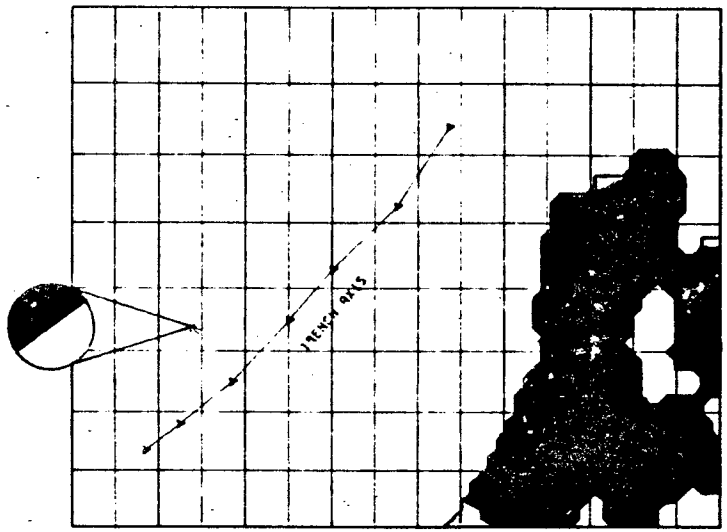


SOURCE: KURILE ISLANDS
LAT. 46.80 LONG. 150.50 DEPTH. 150.0
STRIKE. 53.0 DIP: 90.0 RAKE 90.0 VSRC .8. 30

SOURCE: KB1

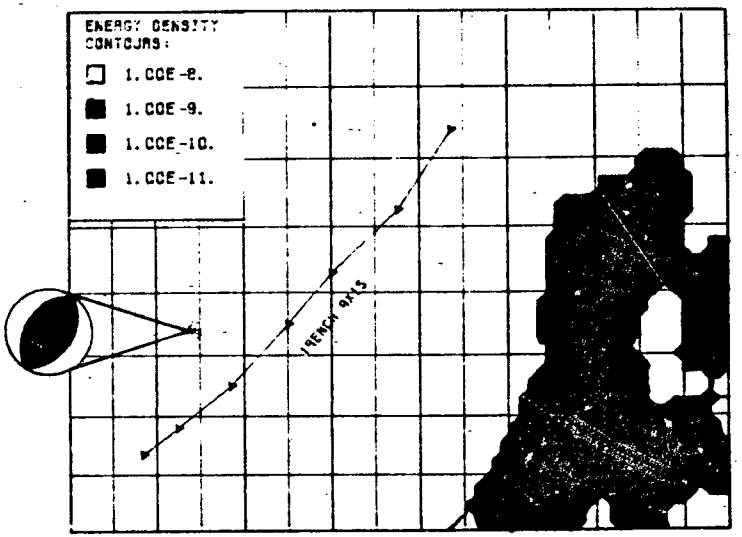


SOURCE: KURILE ISLANDS
LAT. 46.80 LONG. 150.50 DEPTH: 150.0
STRIKE. 34.0 DIP. 45.0 RAKE 270.0 VSRC .8. 30

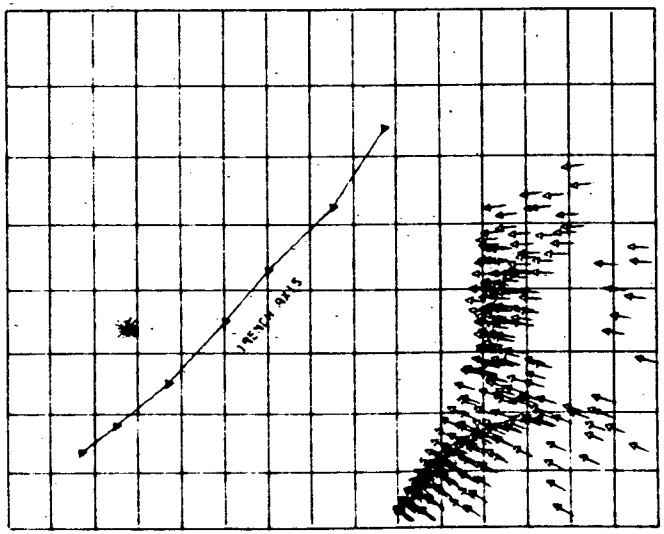


SOURCE: KURILE ISLANDS
LAT. 46.80 LONG. 150.50 DEPTH. 150.0

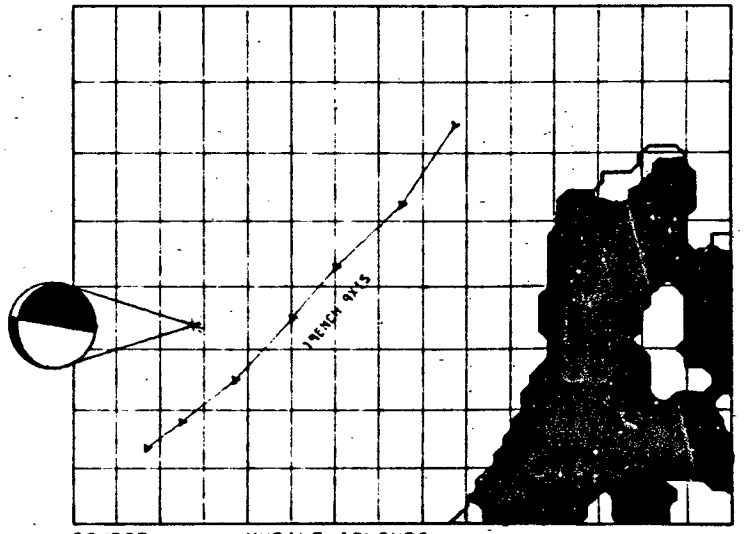


SOURCE: KURILE ISLANDS
LAT. 46.80 LONG. 150.50 DEPTH. 150.0
STRIKE. 100.0 DIP. 90.0 RAKE 110.0 VSRC .8. 30

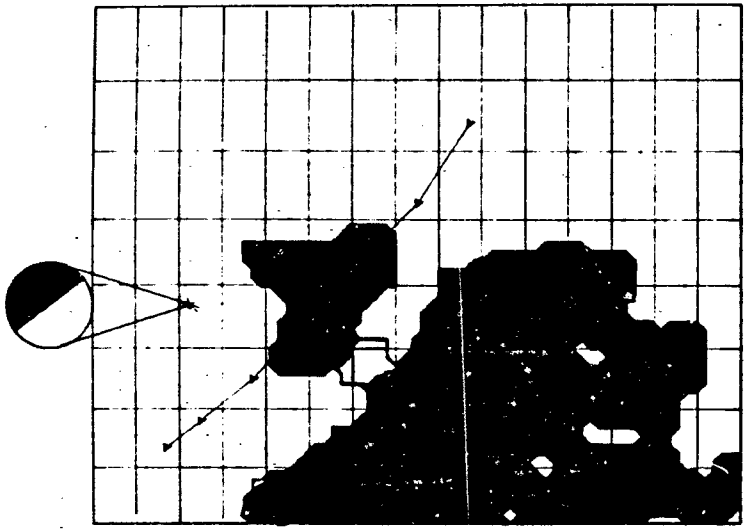

SOURCE: KURILE ISLANDS
LAT. 47.40 LONG. 149.50 DEPTH: 275.0
STRIKE: 53.0 DIP: 90.0 RAKE: 90.0 VSRC .9. 28

SOURCE: KB2

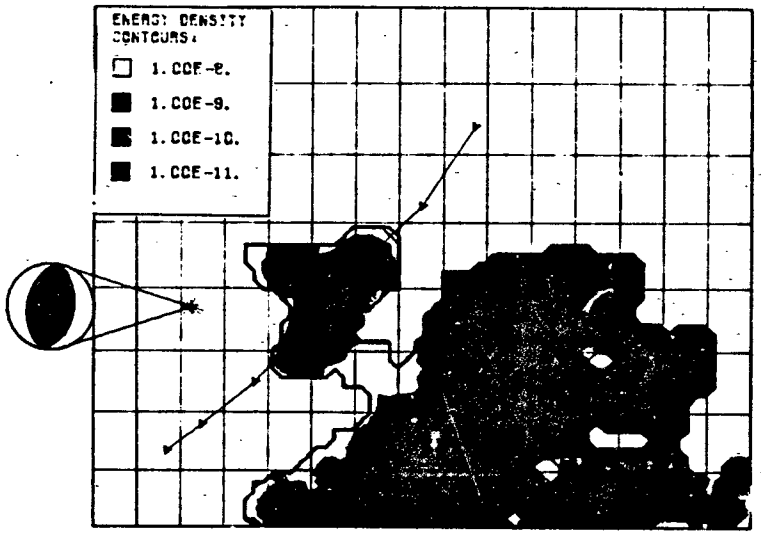


SOURCE: KURILE ISLANDS
LAT. 47.40 LONG. 149.50 DEPTH: 275.0
STRIKE. 10.0 DIP. 45.0 RAKE. 90.0 VSRC .9. 28

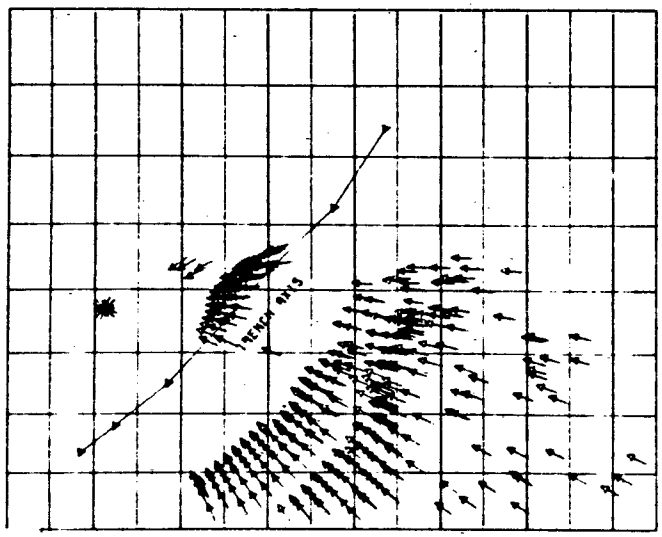


SOURCE: KURILE ISLANDS
LAT. 47.40 LONG. 149.50 DEPTH. 275.0

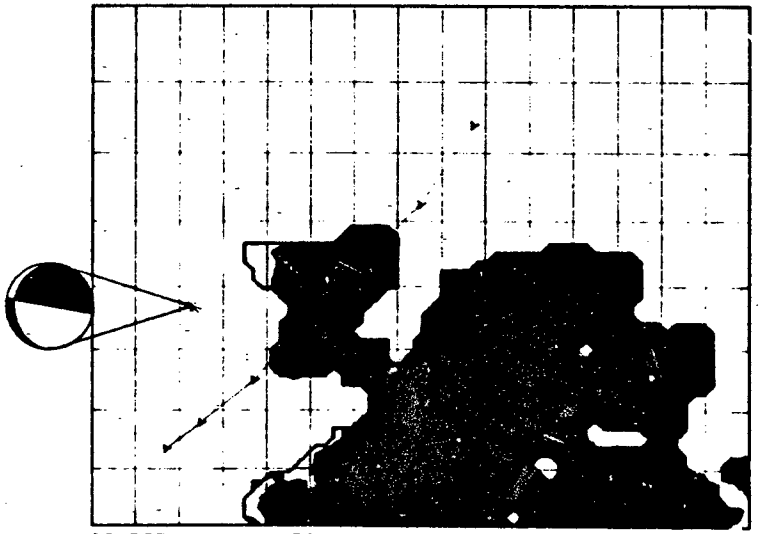

SOURCE: KURILE ISLANDS
LAT. 47.40 LONG. 149.50 DEPTH. 275.0
STRIKE. 100.0 DIP: 90.0 RAKE: 110.0 VSRC .9. 28

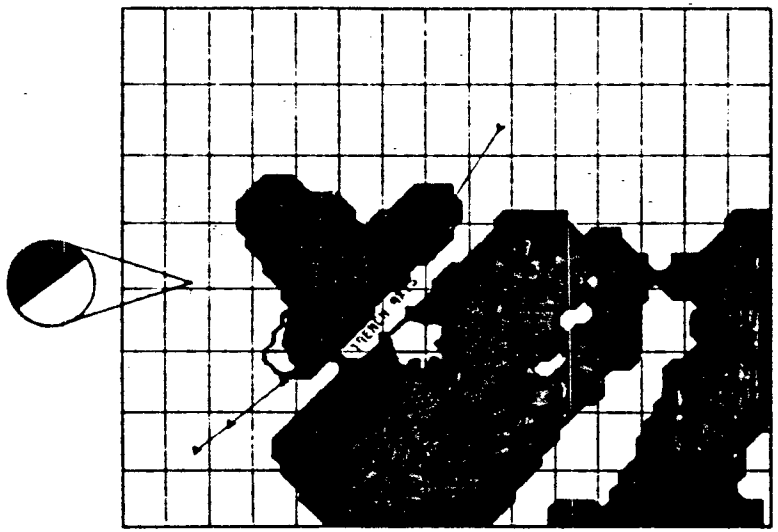

SOURCE: KURILE ISLANDS
LAT: 48.20 LONG: 148.20 DEPTH: 425.0
STRIKE: 53.0 DIP: 90.0 RAKE: -90.0 VSRC: -9.99

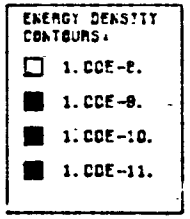


SOURCE: KB3

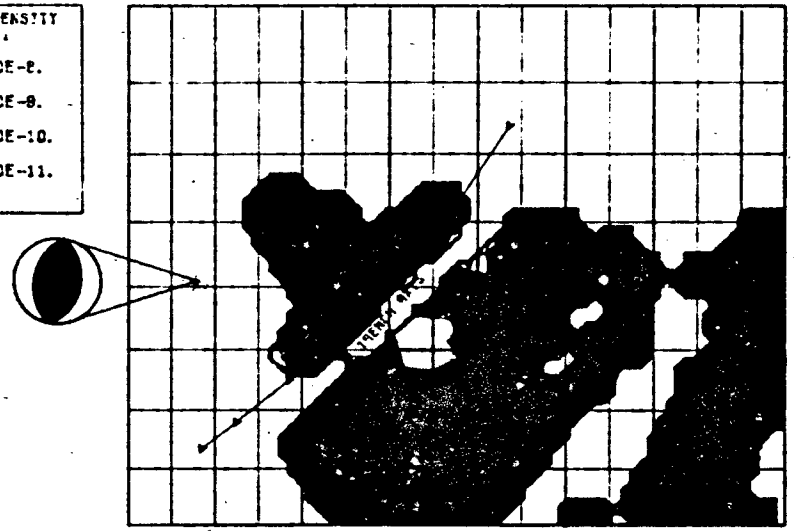

SOURCE: KURILE ISLANDS
LAT: 48.20 LONG: 148.20 DEPTH: 425.0
STRIKE: 10.0 DIP: 45.0 RAKE: -90.0 VSRC: -9.99

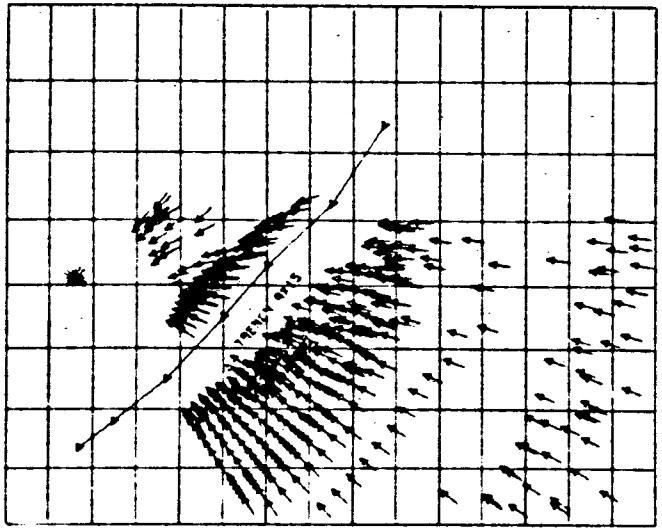

SOURCE: KURILE ISLANDS
LAT: 48.20 LONG: 148.20 DEPTH: 425.0

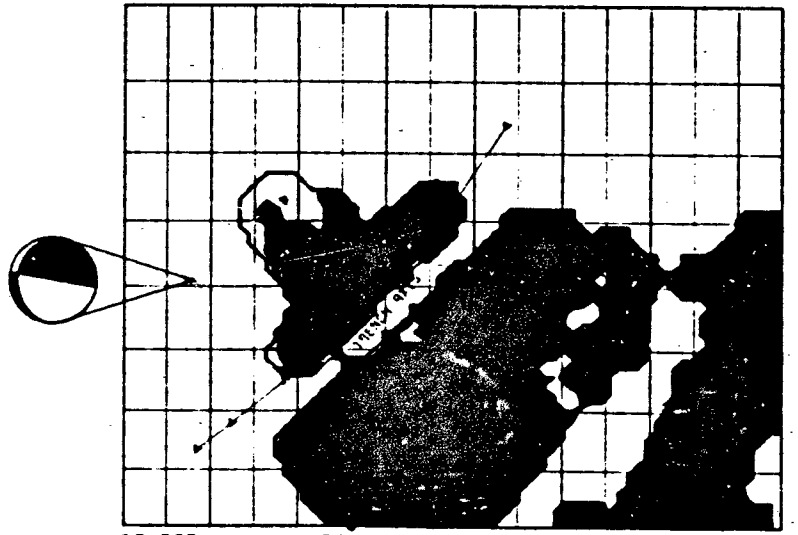

SOURCE: KURILE ISLANDS
LAT: 48.20 LONG: 148.20 DEPTH: 425.0
STRIKE: 100.0 DIP: 90.0 RAKE: -110.0 VSRC: -9.99

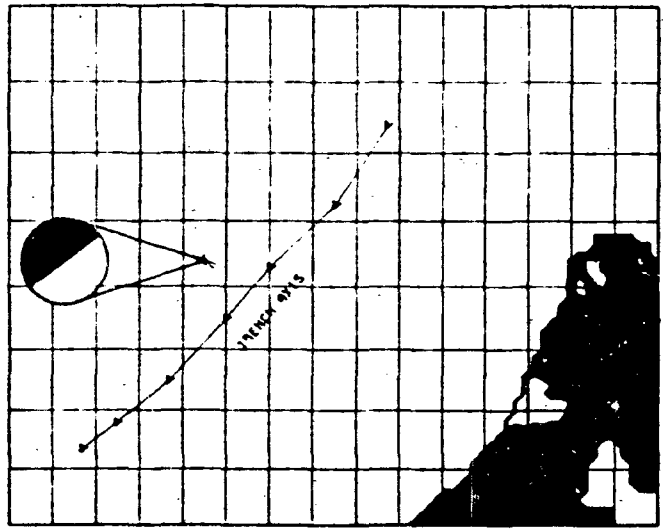


SOURCE: KURILE ISLANDS
LAT. 48.80 LONG. 154.00 DEPTH. 150.0
STRIKE. 53.0 DIP. 90.0 RAKE 90.0 VSRC .8.28

SOURCE: KC1

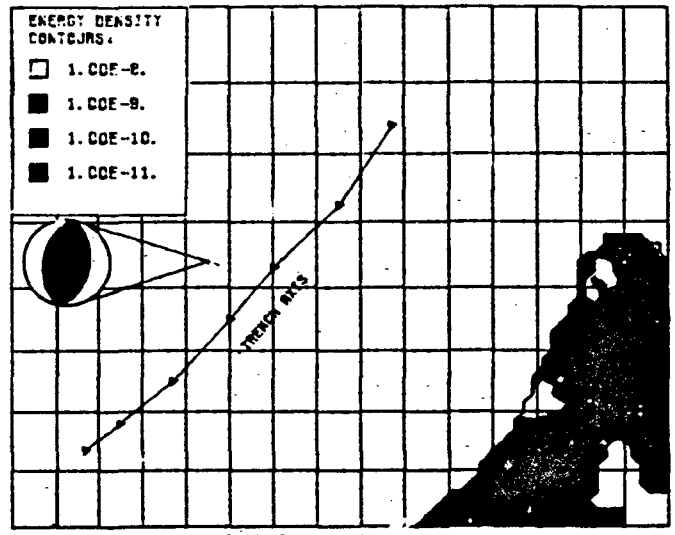


SOURCE: KURILE ISLANDS
LAT: 48.80 LONG: 154.00 DEPTH: 150.0
STRIKE: 10.0 DIP: 45.0 RAKE 90.0 VSRC :8.28

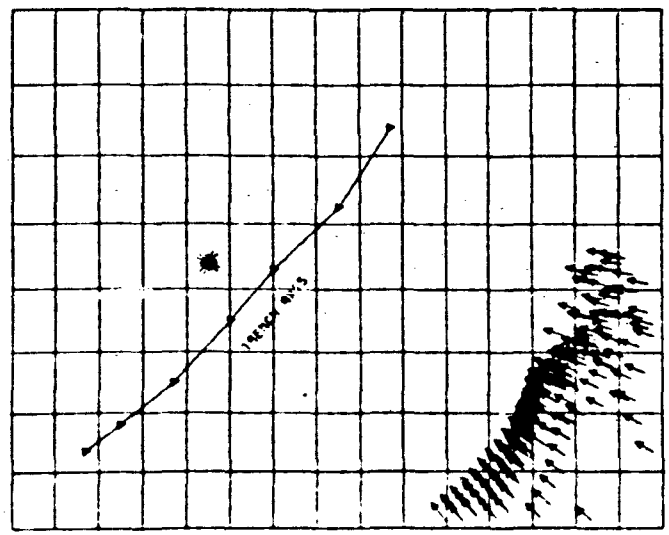


SOURCE. KURILE ISLANDS
LAT. 48.80 LONG. 154.00 DEPTH. 150.0

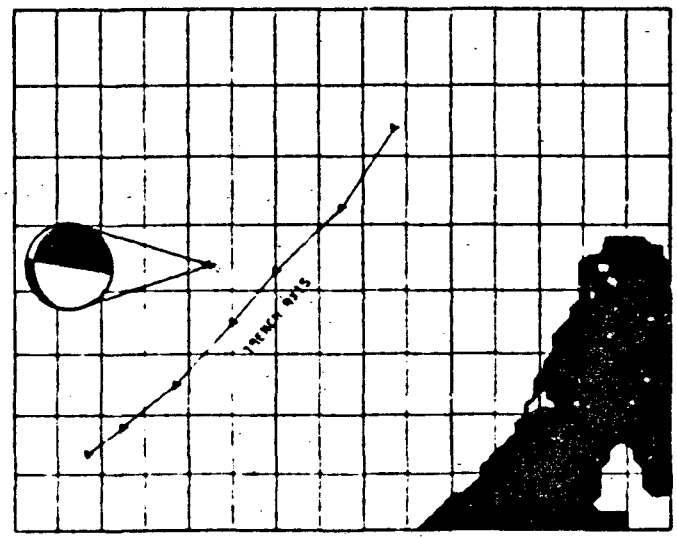


SOURCE. KURILE ISLANDS
LAT. 48.80 LONG 154.00 DEPTH. 150.0
STRIKE. 100.0 DIP. 90.0 RAKE :10.0 VSRC .8.28

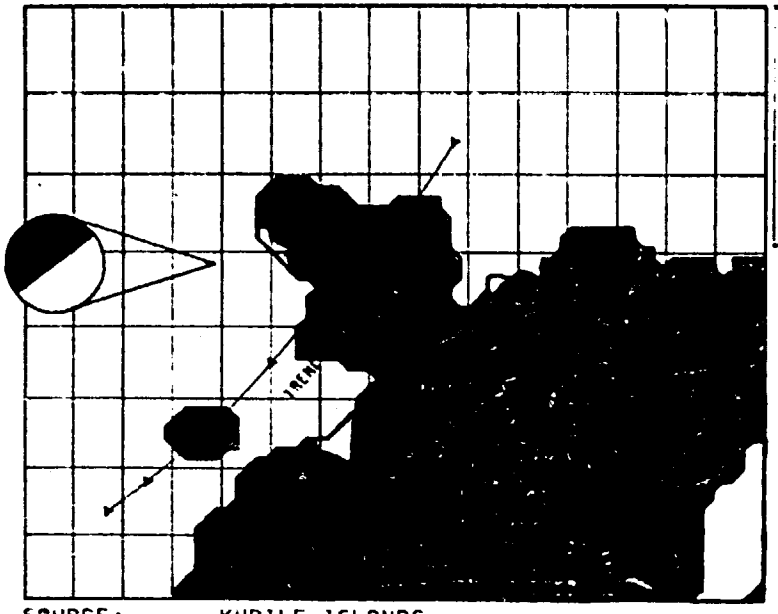


SOURCE: KURILE ISLANDS
LAT. 49.70 LONG. 152.70 DEPTH: 300.0
STRIKE. 53.0 DIP: 90.0 RAKE: 90.0 VSRC: 9.07

SOURCE: KC2

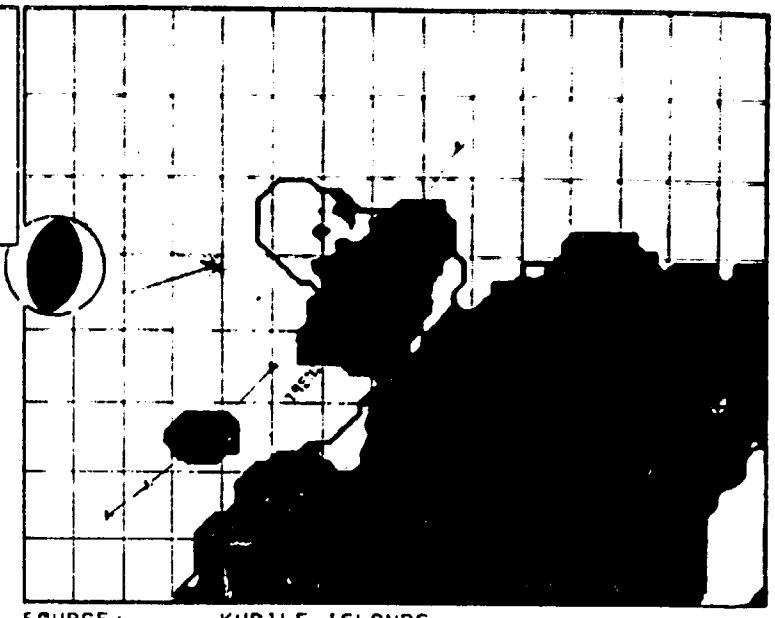

SOURCE: KURILE ISLANDS
LAT. 49.70 LONG. 152.70 DEPTH: 300.0
STRIKE. 10.0 DIP: 45.0 RAKE: 90.0 VSRC: 9.07

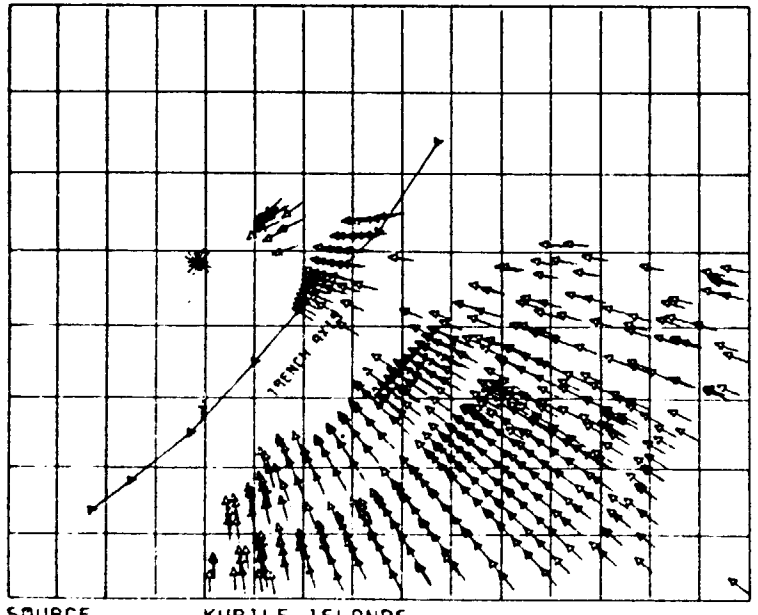

SOURCE. KURILE ISLANDS
LAT. 49.70 LONG. 152.70 DEPTH: 300.0

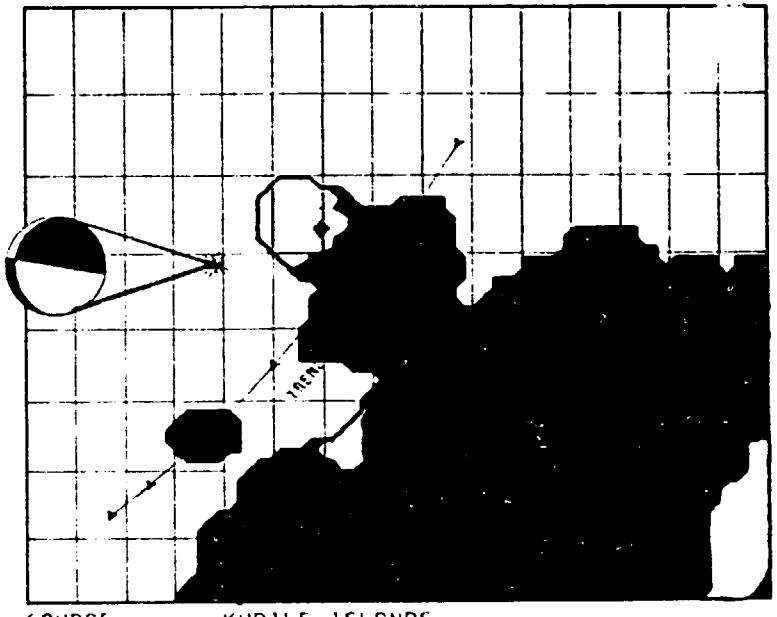

SOURCE. KURILE ISLANDS
LAT. 49.70 LONG. 152.70 DEPTH: 300.0
STRIKE. 100.0 DIP: 90.0 RAKE: 110.0 VSRC: 9.07

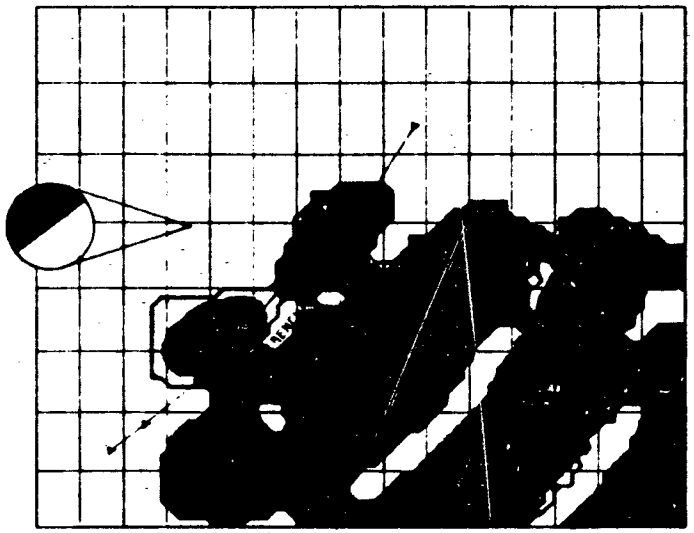

SOURCE: KURILE ISLANDS

LAT. 49.90 LONG. 152.10 DEPTH. 400.0

STRIKE. 53.0 DIP. 90.0 RAKE 90.0 VSRC .9.97

SOURCE: KC3

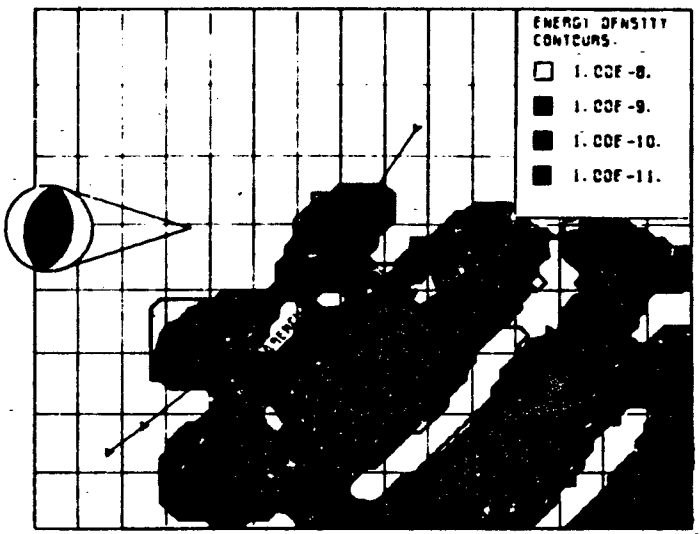


SOURCE: KURILE ISLANDS

LAT. 49.90 LONG. 152.10 DEPTH. 400.0

STRIKE. 10.0 DIP. 45.0 RAKE 90.0 VSRC .9.97

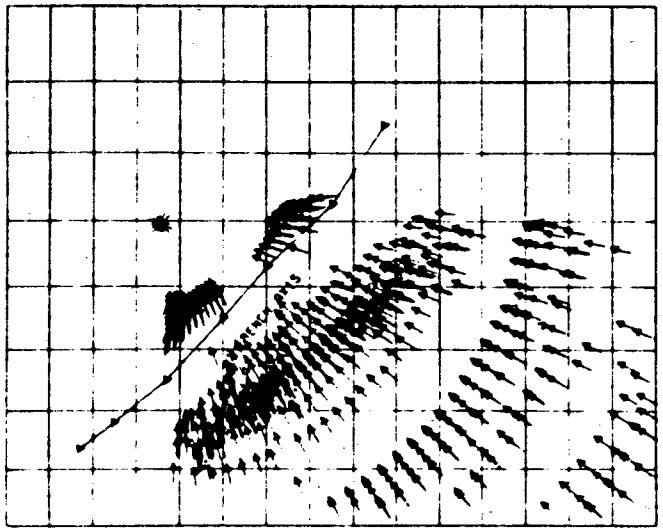

SOURCE: KURILE ISLANDS

LAT. 49.90 LONG 152.10 DEPTH. 400.0

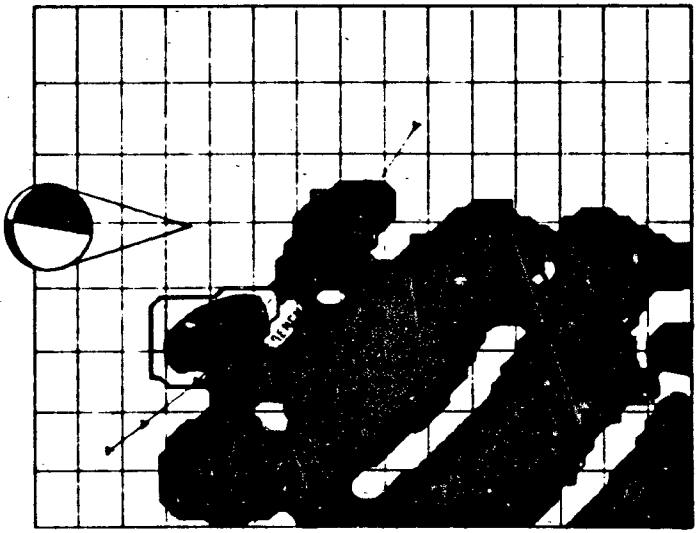

SOURCE: KURILE ISLANDS

LAT. 49.90 LONG 152.10 DEPTH. 400.0

STRIKE. 100.0 DIP. 90.0 RAKE 110.0 VSRC .9.97

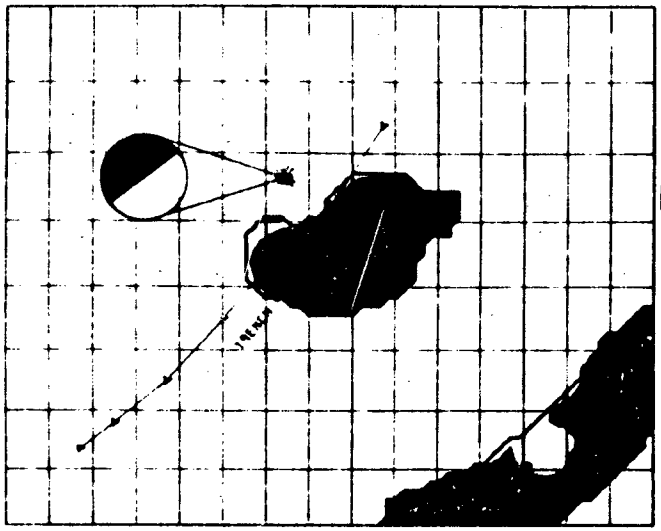


ENERGY DENSITY CONTOURS

- 1.00E-8.
- 1.00E-9.
- 1.00E-10
- 1.00E-11.

SOURCE: KURILE ISLANDS

LAT: 51.30 LONG: 157.80 DEPTH: 150.0

STRIKE: 53.0 DIP: 90.0 RAKE: 90.0 VSRC: 8.28

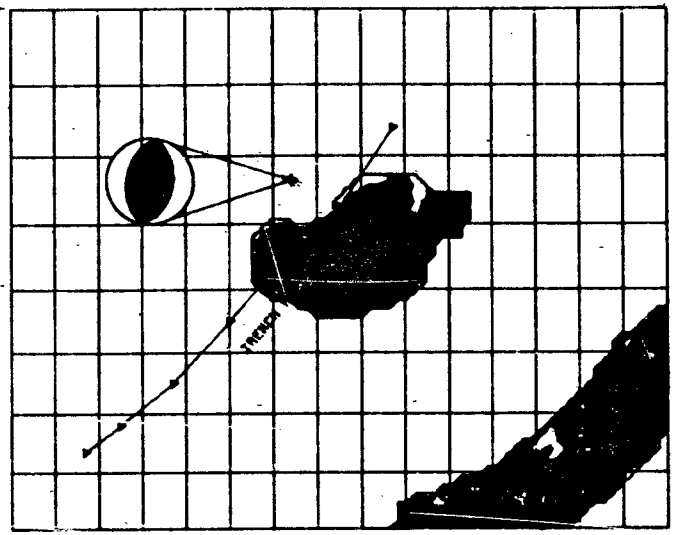


SOURCE: KURILE ISLANDS

LAT: 51.30 LONG: 157.80 DEPTH: 150.0

STRIKE: 10.0 DIP: 45.0 RAKE: 90.0 VSRC: 8.28

SOURCE: KD1

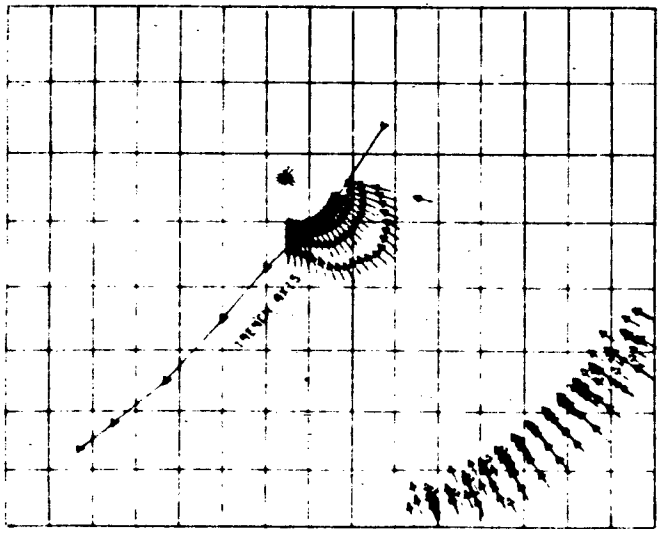


SOURCE: KURILE ISLANDS

LAT: 51.30 LONG: 157.80 DEPTH: 150.0

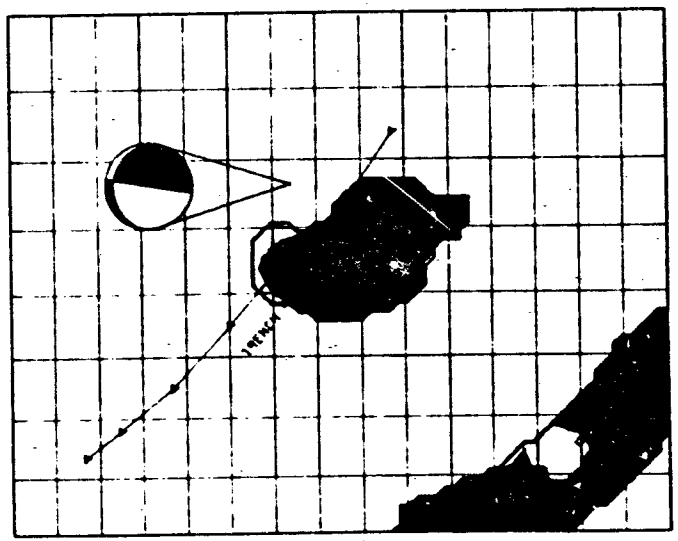


SOURCE: KURILE ISLANDS

LAT: 51.30 LONG: 157.80 DEPTH: 150.0

STRIKE: 100.0 DIP: 90.0 RAKE: 110.0 VSRC: 8.28

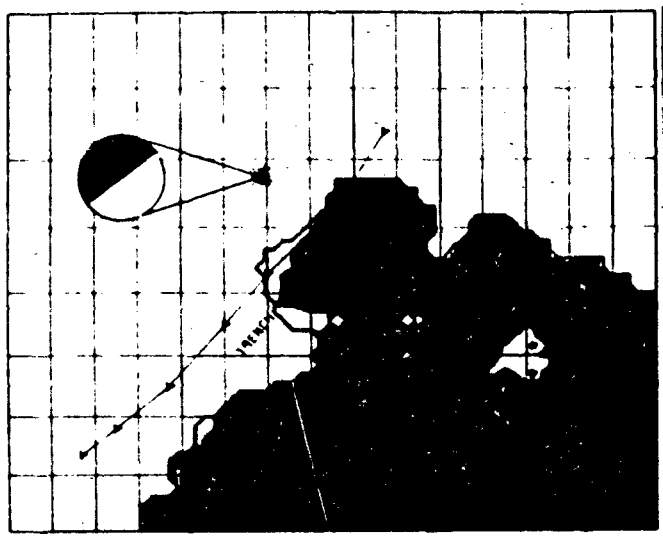


ENERG. DENSITY CONTOURS
1.00E-8.
1.00E-9
1.00E-10
1.00E-11

SOURCE. KURILE ISLANDS
LAT. 51.50 LONG. 156.70 DEPTH. 275.0
STRIKE. 53.0 DIP. 90.0 RAKE. 90.0 VSRC. 9.29

SOURCE: KD2

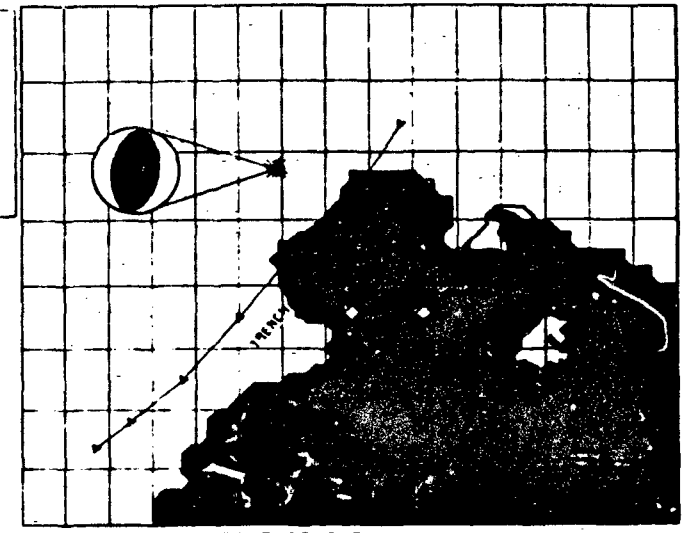


SOURCE. KURILE ISLANDS
LAT. 51.50 LONG. 156.70 DEPTH. 275.0
STRIKE. 10.0 DIP. 45.0 RAKE. 90.0 VSRC. 9.29

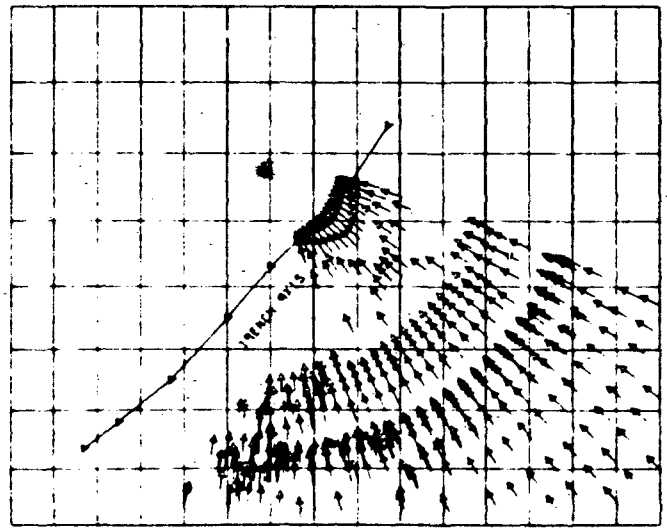


SOURCE. KURILE ISLANDS
LAT. 51.50 LONG. 156.70 DEPTH. 275.0

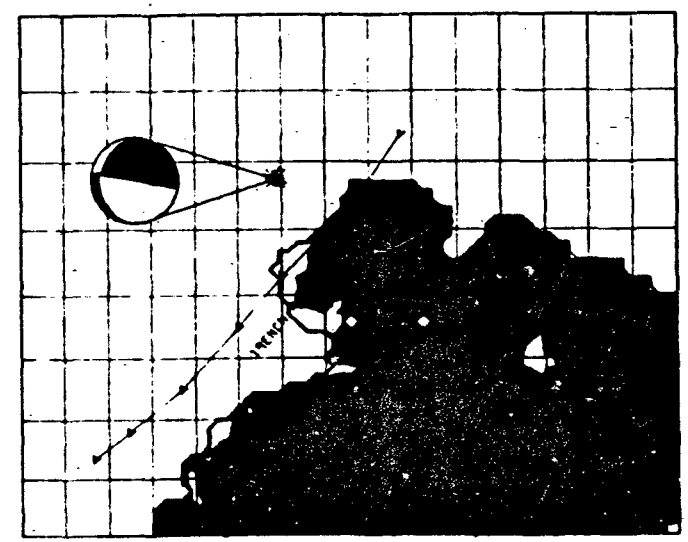


SOURCE. KURILE ISLANDS
LAT. 51.50 LONG. 156.70 DEPTH. 275.0
STRIKE. 100.0 DIP. 90.0 RAKE. 110.0 VSRC. 9.29

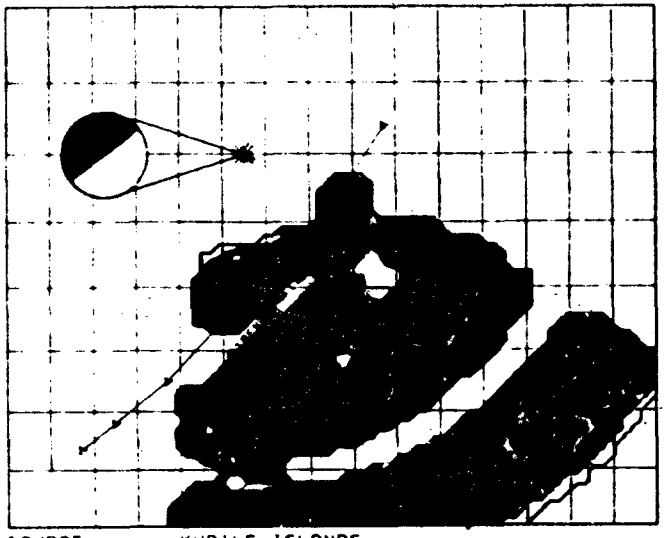

SOURCE. KURILE ISLANDS
LAT. 52.00 LONG. 156.00 DEPTH. 400.0
STRIKE. 53.0 DIP. 90.0 RAKE 90.0 VSRC .9.97

**SOURCE: KD3**

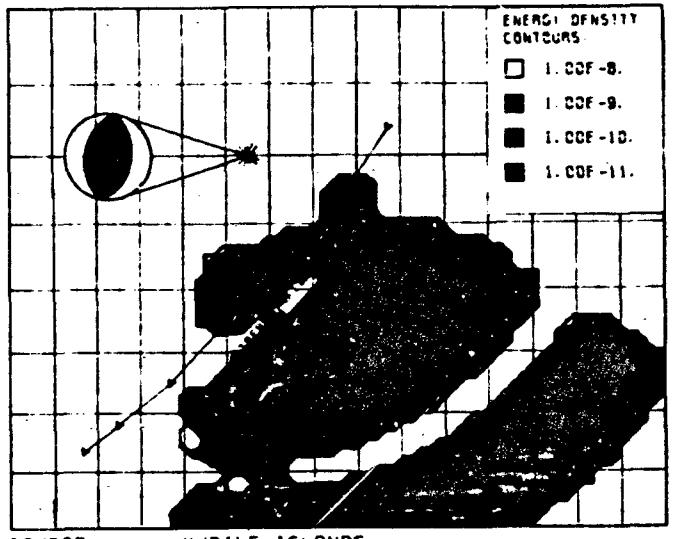


SOURCE: KURILE ISLANDS
LAT. 52.00 LONG. 156.00 DEPTH. 400.0
STRIKE. 10.0 DIP. 45.0 RAKE 90.0 VSRC .9.97

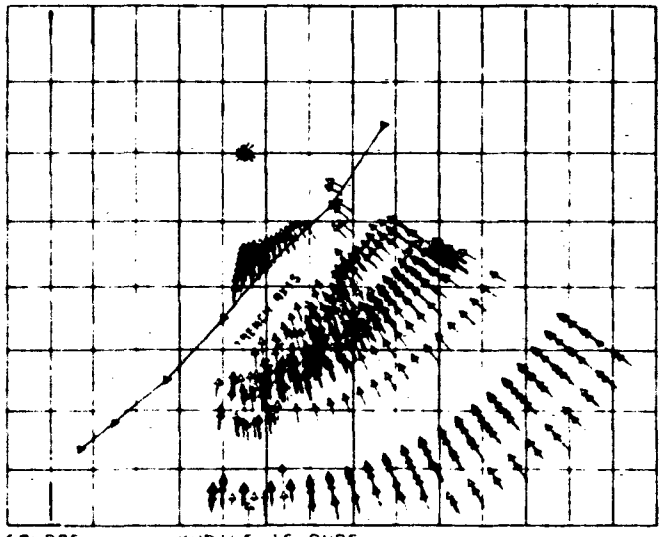

SOURCE. KURILE ISLANDS
LAT. 52.00 LONG 156.00 DEPTH 400.0

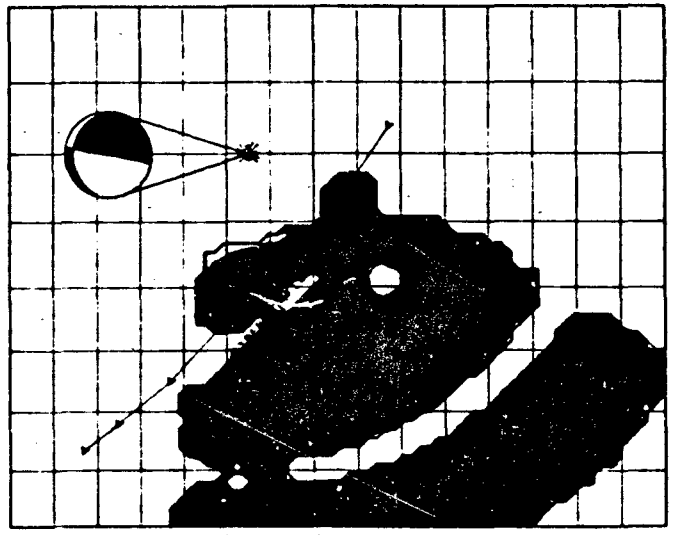

SOURCE. KURILE ISLANDS
LAT. 52.00 LONG. 156.00 DEPTH. 400.0
STRIKE. 100.0 DIP. 90.0 RAKE 110.0 VSRC .9.97

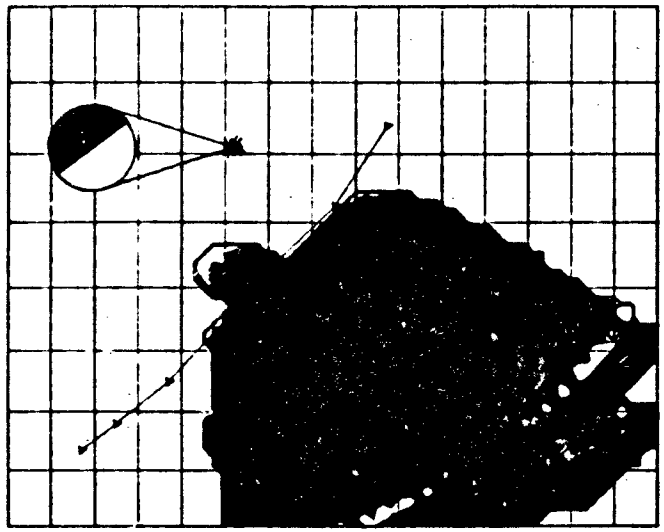

SOURCE. KURILE ISLANDS
LAT. 52.20 LONG. 155.30 DEPTH. 600.0
STRIKE. 53.0 DIP. 90.0 RAKE 90.0 VSRC 10.86

**SOURCE: KD4**

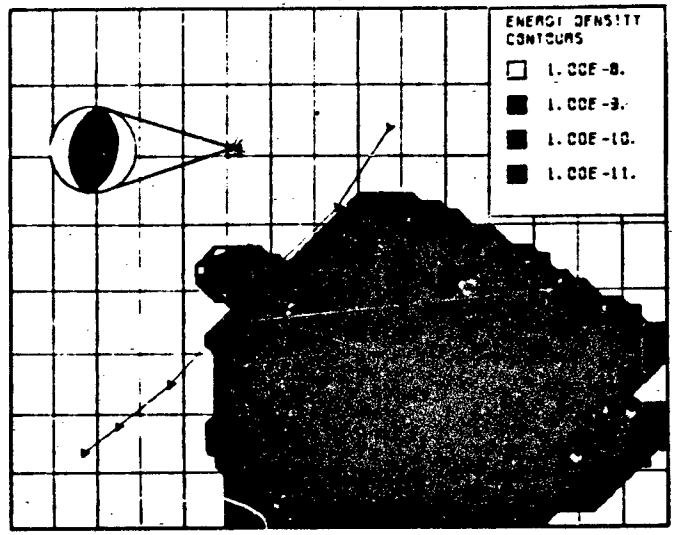


SOURCE: KURILE ISLANDS
LAT. 52.20 LONG. 155.30 DEPTH. 600.0
STRIKE. 10.0 DIP. 45.0 RAKE 90.0 VSRC 10.86

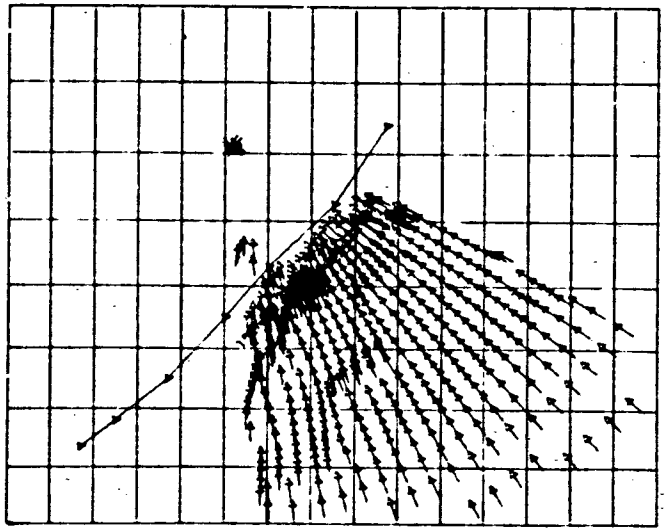

SOURCE. KURILE ISLANDS
LAT. 52.20 LONG. 155.30 DEPTH. 600.0

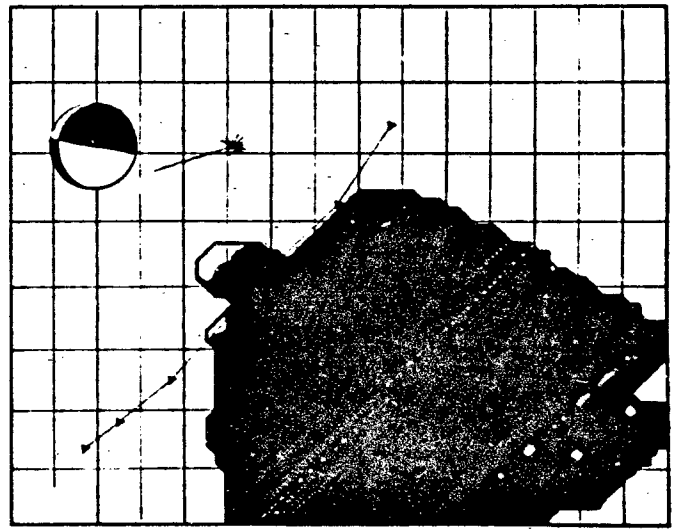

SOURCE: KURILE ISLANDS
LAT: 52.20 LONG: 155.30 DEPTH. 600.0
STRIKE: 100.0 DIP: 30.0 RAKE 110.0 VSRC 10.86

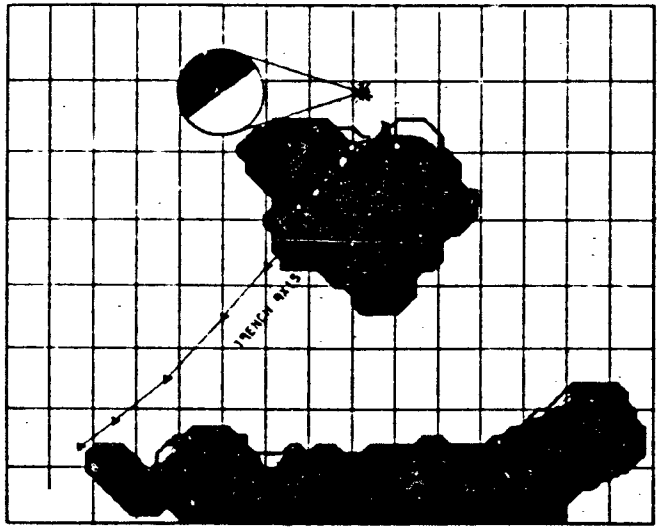


SOURCE: KURILE ISLANDS
LAT. 53.70 LONG. 161.30 DEPTH. 150.0
STRIKE. 53.0 DIP: 90.0 RAKE 90.0 VSRC .8.27

SOURCE: KE1

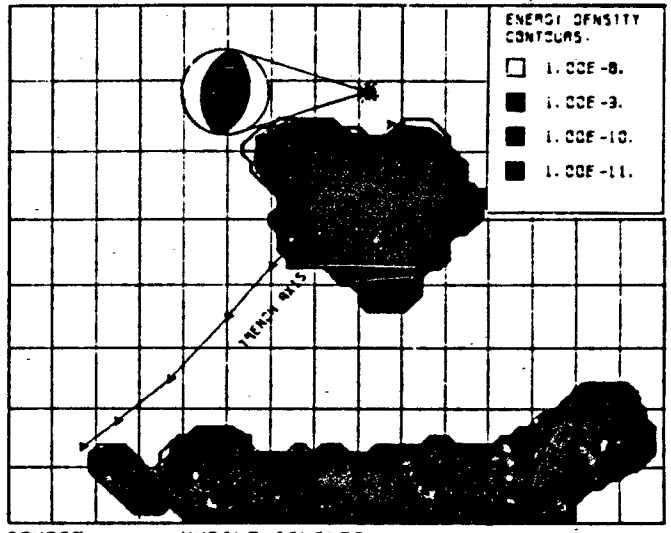


SOURCE: KURILE ISLANDS
LAT. 53.70 LONG. 161.30 DEPTH. 150.0
STRIKE. 10.0 DIP: 45.0 RAKE 90.0 VSRC .8.27

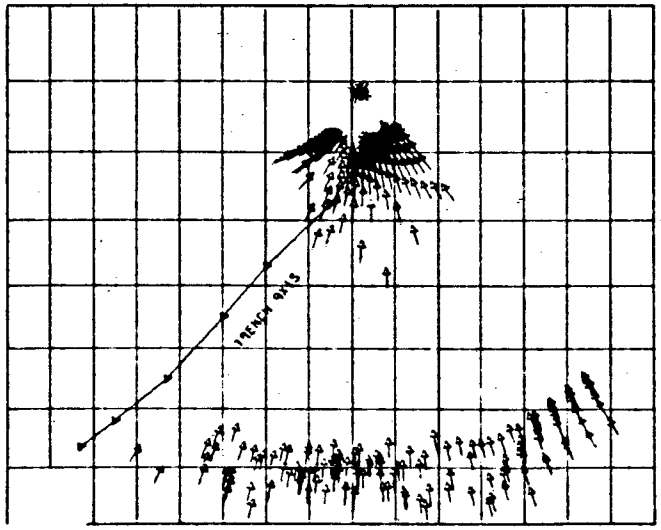


SOURCE. KURILE ISLANDS
LAT. 53.70 LONG. 161.30 DEPTH. 150.0

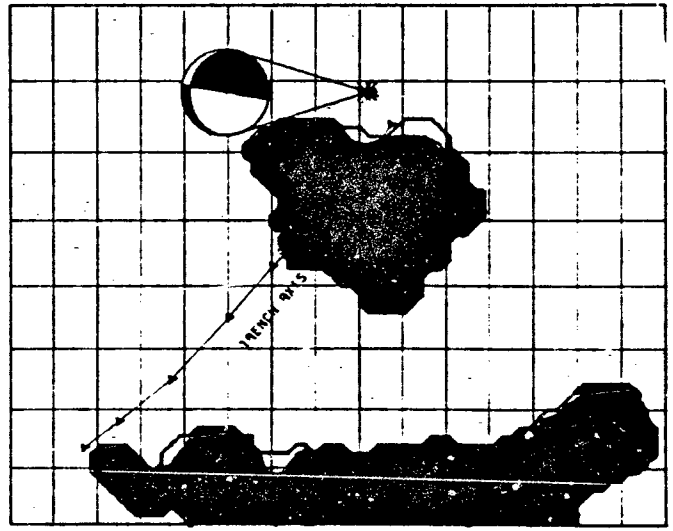


SOURCE. KURILE ISLANDS
LAT. 53.70 LONG. 161.30 DEPTH. 150.0
STRIKE. 100.0 DIP. 90.0 RAKE .110.0 VSRC .8.27

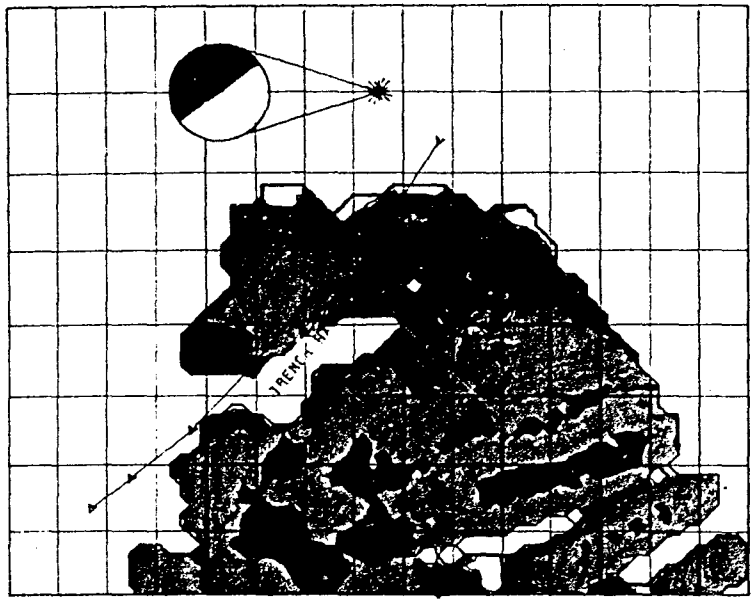


SOURCE: KURILE ISLANDS

LAT. 54.00 LONG. 160.00 DEPTH: 325.0

STRIKE: 53.0 DIP: 90.0 RAKE: 90.0 VSRC .9.57

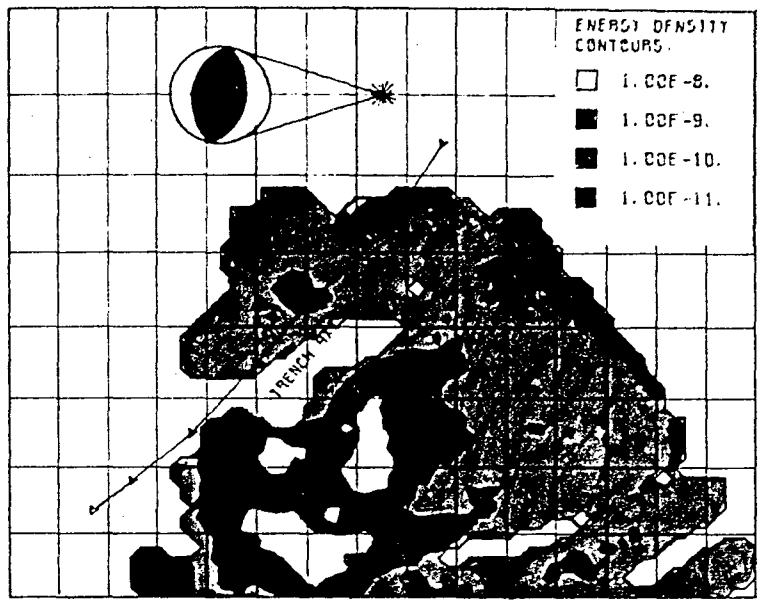


SOURCE: KURILE ISLANDS

LAT: 54.00 LONG. 160.00 DEPTH: 325.0

STRIKE. 10.0 DIP. 45.0 RAKE .90.0 VSRC .9.57

SOURCE: KE2

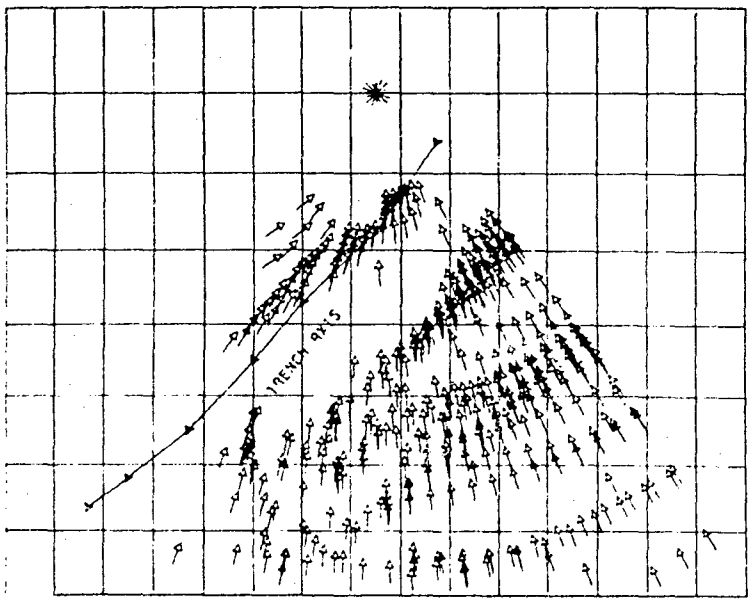


SOURCE. KURILE ISLANDS

LAT. 54.00 LONG. 160.00 DEPTH. 325.0

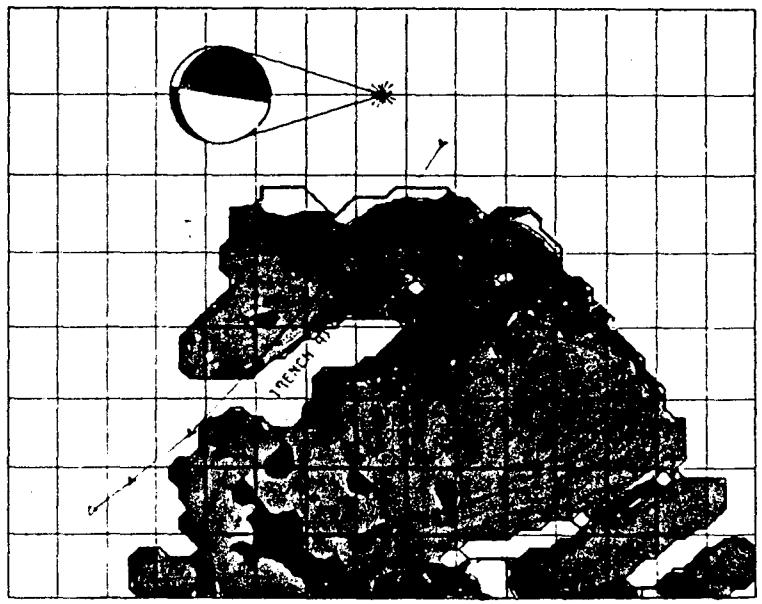


SOURCE. KURILE ISLANDS

LAT. 54.00 LONG. 160.00 DEPTH. 325.0

STRIKE. 100.0 DIP. 90.0 RAKE .110.0 VSRC .9.57

SOURCE: KURILE ISLANDS

LAT. 54.70 LONG. 158.40 DEPTH: 550.0

STRIKE: 53.0 DIP: 90.0 RAKE: 90.0 VSRC: 10.61


SOURCE: KE3

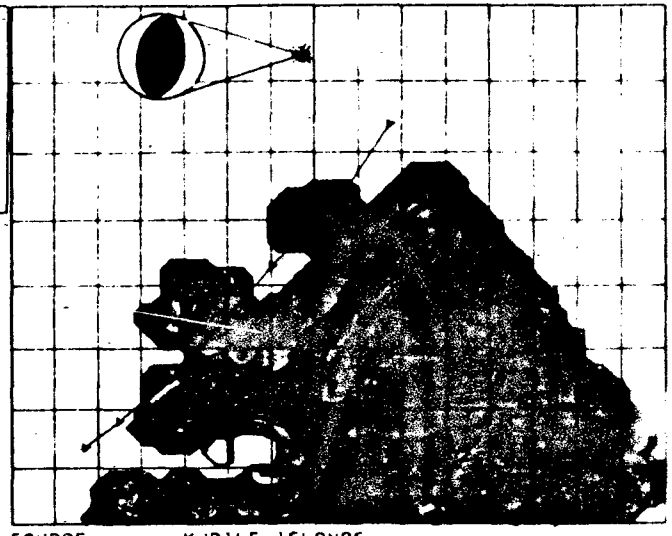

SOURCE: KURILE ISLANDS

LAT. 54.70 LONG. 158.40 DEPTH: 550.0

STRIKE: 10.0 DIP: 45.0 RAKE: 90.0 VSRC: 10.61

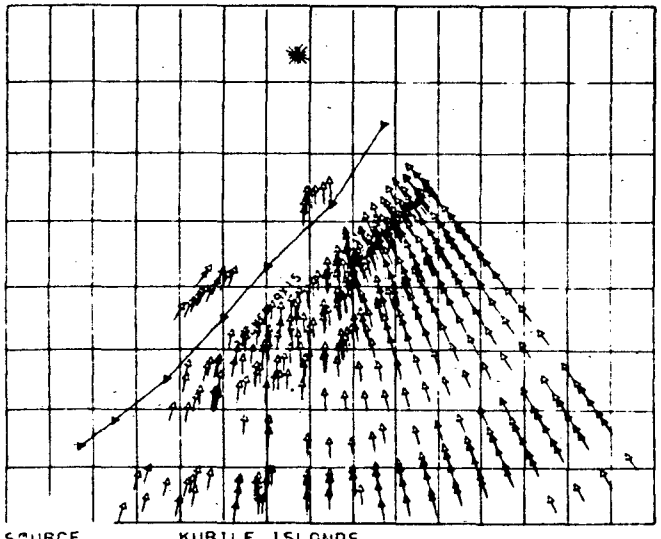

SOURCE: KURILE ISLANDS

LAT. 54.70 LONG. 158.40 DEPTH: 550.0

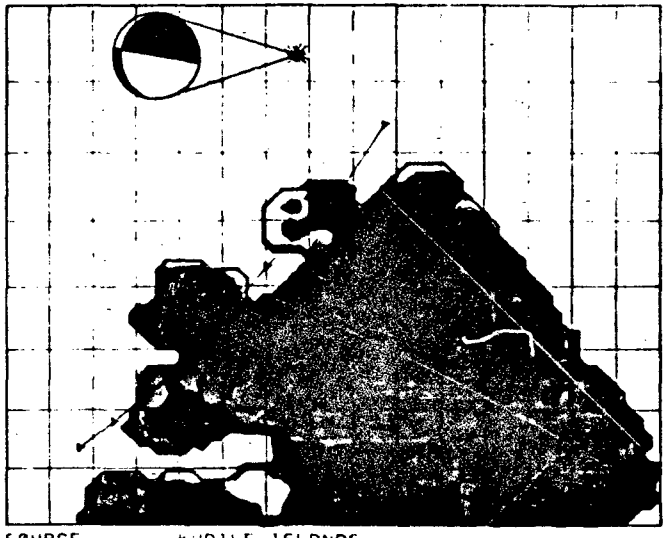

SOURCE: KURILE ISLANDS

LAT. 54.70 LONG. 158.40 DEPTH: 550.0

STRIKE: 100.0 DIP: 90.0 RAKE: 110.0 VSRC: 10.61

rare to observe absolute null regions corresponding to radiation pattern nulls. In Figure 31, this result is illustrated more directly. Figures 31a and 31b plot the emergence points and radiation polarity from two deep thrust events at the northern end of the trench, the first at a depth of 325 km, the second at 550 km. Compressional and dilatational arrivals are represented by open circles and crosses respectively. The strong overlap of the two polarities clearly illustrate the problem. This result is presented not as a necessarily important siting consideration but rather as an indication of potential ambiguities in the data once the MSS is sited or operating. At that time, it would be worthwhile to perform this kind of analysis to improve the utility of the data from the MSS.

GENERALIZED RAY THEORY ANALYSIS

In the ray tracing analysis presented in the preceding section, only the direct arrivals were included. No reflected or diffracted phases were included in the calculations. This represents an appropriate solution since the first arrivals from these deeper events will be the direct rays, any reflected or other phases will arrive later in the wavetrain. However, when the hypocentral depths are relatively shallow (less than ~100 km for this velocity structure), the situation changes. The direct, diving rays are refracted down into the mantle and channeled out to distances beyond the area of interest. This point was illustrated in Figure 13. Hence, the siting area sits in a classical shadow zone for the diving or direct rays from shallow sources in the

# KURILE TRENCH RAY TRACING

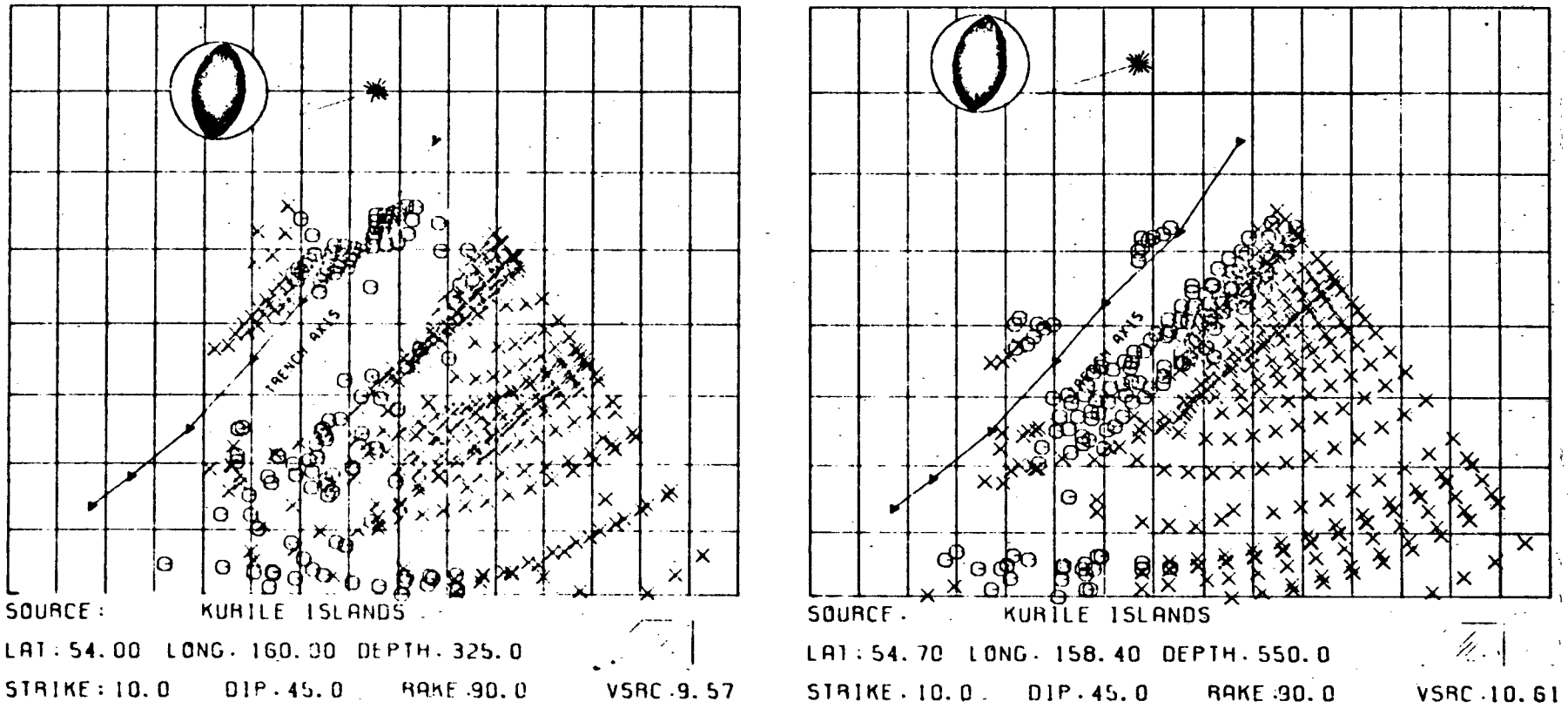


**Figure 31.** Ray emergence points and radiation polarity are plotted here for two thrust earthquakes implanted at depths of 325 km and 550 km. Crosses indicate dilatational first motions and open circles compressional. Polarities normally change smoothly through nodal regions but in this case the structural complexity has caused raypaths to wander. The mixing of ray polarities which results would certainly introduce error into a calculation of source mechanism.

Kuriles or Kamchatka. The first arrivals are thus multiple or diffracted $P_g$ and $P_n$ type phases. In order to examine these phases, it has been necessary to use a generalized ray theory code to calculate synthetic seismograms in the region.

A detailed discussion of the calculation of synthetic seismograms is beyond the scope of this report. The methods involved have been extensively discussed in the open seismological literature (e.g., de Hoop, 1960; Helmberger, 1968; Helmberger and Wiggins, 1971, Fuchs, 1971; Wiggins, 1976; Chapman, 1976; Mellman and Helmberger, 1978). In our analysis, we have used the asymptotic Cagniard formulation of Wiggins and Helmberger (1970). Use of this method provides greater insight into the physical processes involved than reflectivity methods (i.e., Fuchs, 1971).

As noted earlier, the first arrivals from shallow sources, at the distances of interest to us here, are dominated by multiple reflected and diffracted $P_g$ and $P_n$ type phases. The resulting seismogram is principally dependent upon the existence of a waveguide layer in which the seismic energy can be efficiently trapped. The details of the seismogram, however, depend strongly upon fine structure such as sediment thicknesses, on the depth of the source relative to the waveguide layer(s), and on such factors as the depth of burial of the downhole seismometer. It was not computationally practical or cost effective to examine many, much less all, of the possible source-receiver pairs in the Kuriles/Kamchatka area. As an alternative approach, we have used first an illustrative calculation by Helmberger

and Engen (1980) of propagation in a layer over a half space; and, second, we have calculated the response of our upper mantle model for several different shallow source depths. In each case, profiles of the synthetic seismograms are presented from 100 km to 1,000 km for each of the three fundamental faults (vertical strike-slip, vertical dip-slip, 45° dip-slip). The first example, shown in Figures 32a, 32b, and 32c, is the calculation by Helmberger and Engen (1980). This study used the following model:

| P Velocity (km/sec) | S Velocity (km/sec) | Density (gm/ee) | Thickness (km) |
|---|---|---|---|
| 6.2 | 3.5 | 2.7 | 32 |
| 8.2 | 4.5 | 3.4 | ∞ |

This calculation includes all of the multiples and trapped energy within the waveguide layer. The purpose of including this result here is to illustrate the complexity introduced into the initial portions of the seismogram by this trapped energy and to give an indication of the expected amplitude fall off with distance.

The second set of examples utilized in our study was obtained by calculating the model response of our upper mantle model (Table I) for three source depths; 5 km, 13 km, and 45 km. This calculation differs from the previous example in that it does not include the higher multiples in the upper waveguide. These calculations include all of the direct phases, head waves, pP and sP phases (off of both the ocean bottom and the underside of the Moho) and such phases as $s_mP$ (energy

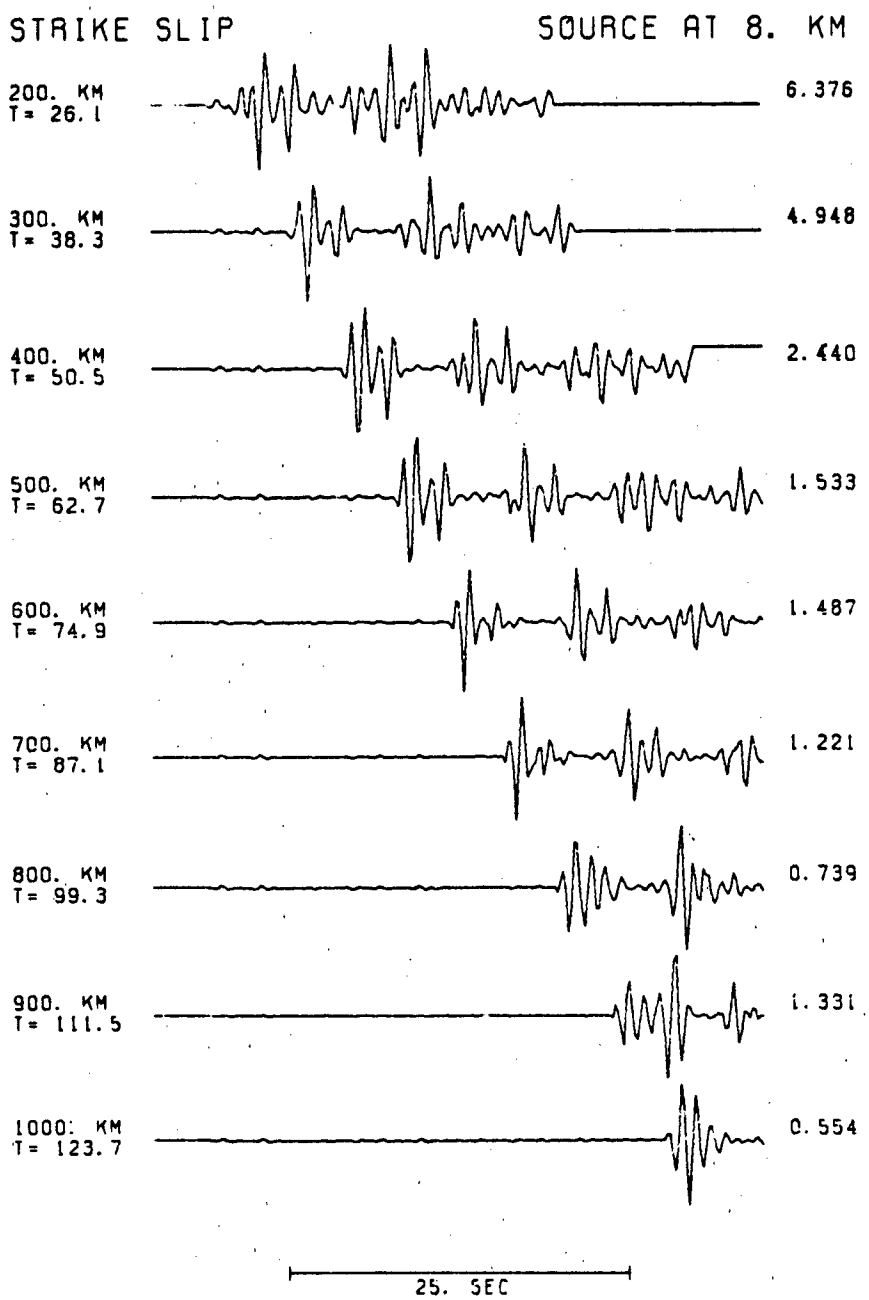


Figures 32a,b,c. Layer over half-space calculation by Helmberger and Engen (1980). The vertical displacement responses are calculated for each of the three fundamental double couple systems: strike-slip (a), vertical dip-slip (b), 45° dip slip (c). Each response has been convolved with a triangular time function (0.5, 0.5 sec) and a WWSSN short period response. The numbers on the right indicate the trace amplitudes in $10^{-6}$cm. Assuming a source with static moment $M_o = 4\pi\rho_o$ x $10^{20}$ dyn-cm.

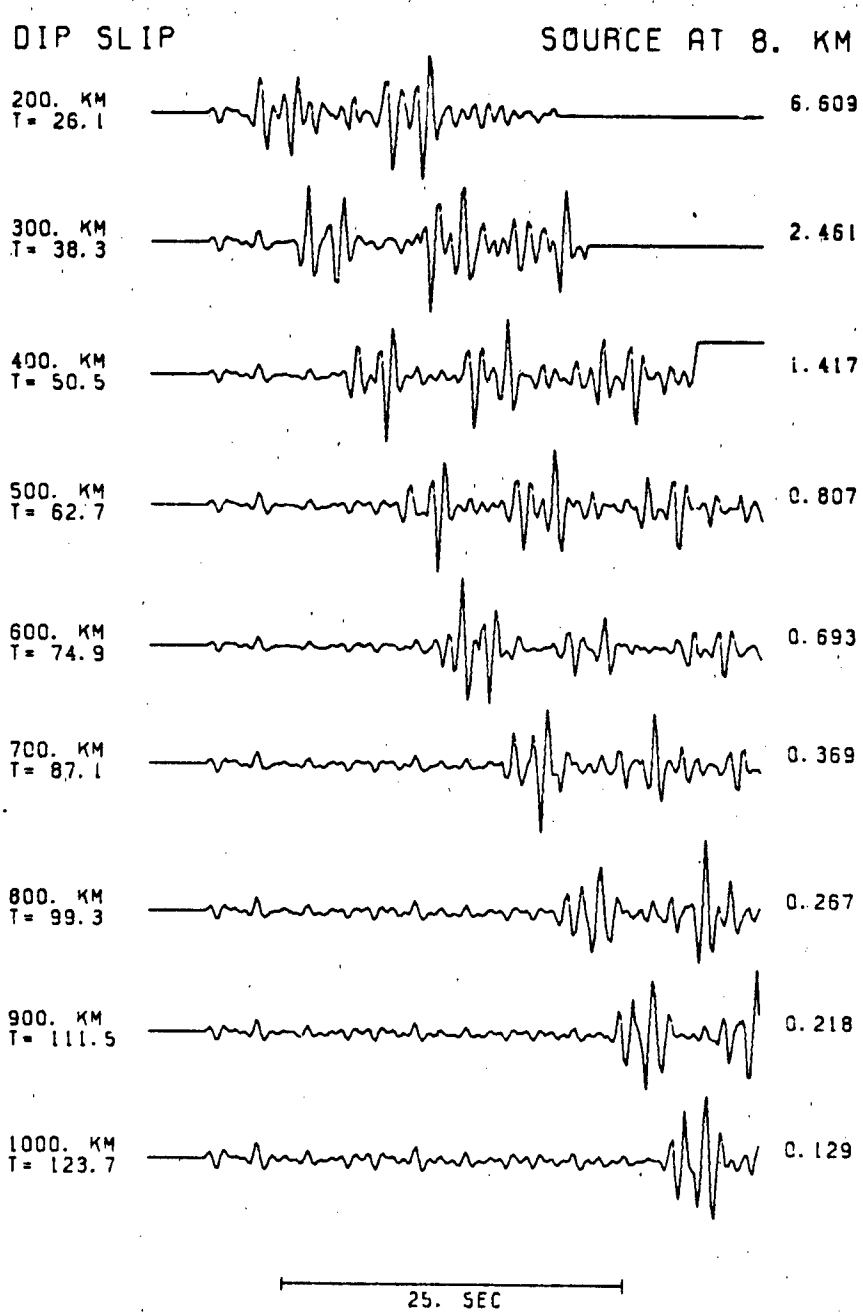
DIP SLIP
SOURCE AT 8. KM
200. KM
T= 26.1
6.609
300. KM
T= 38.3
2.461
400. KM
T= 50.5
1.417
500. KM
T= 62.7
0.807
600. KM
T= 74.9
0.693
700. KM
T= 87.1
0.369
800. KM
T= 99.3
0.267
900. KM
T= 111.5
0.218
1000. KM
T= 123.7
0.129
25. SEC

Figure 32b

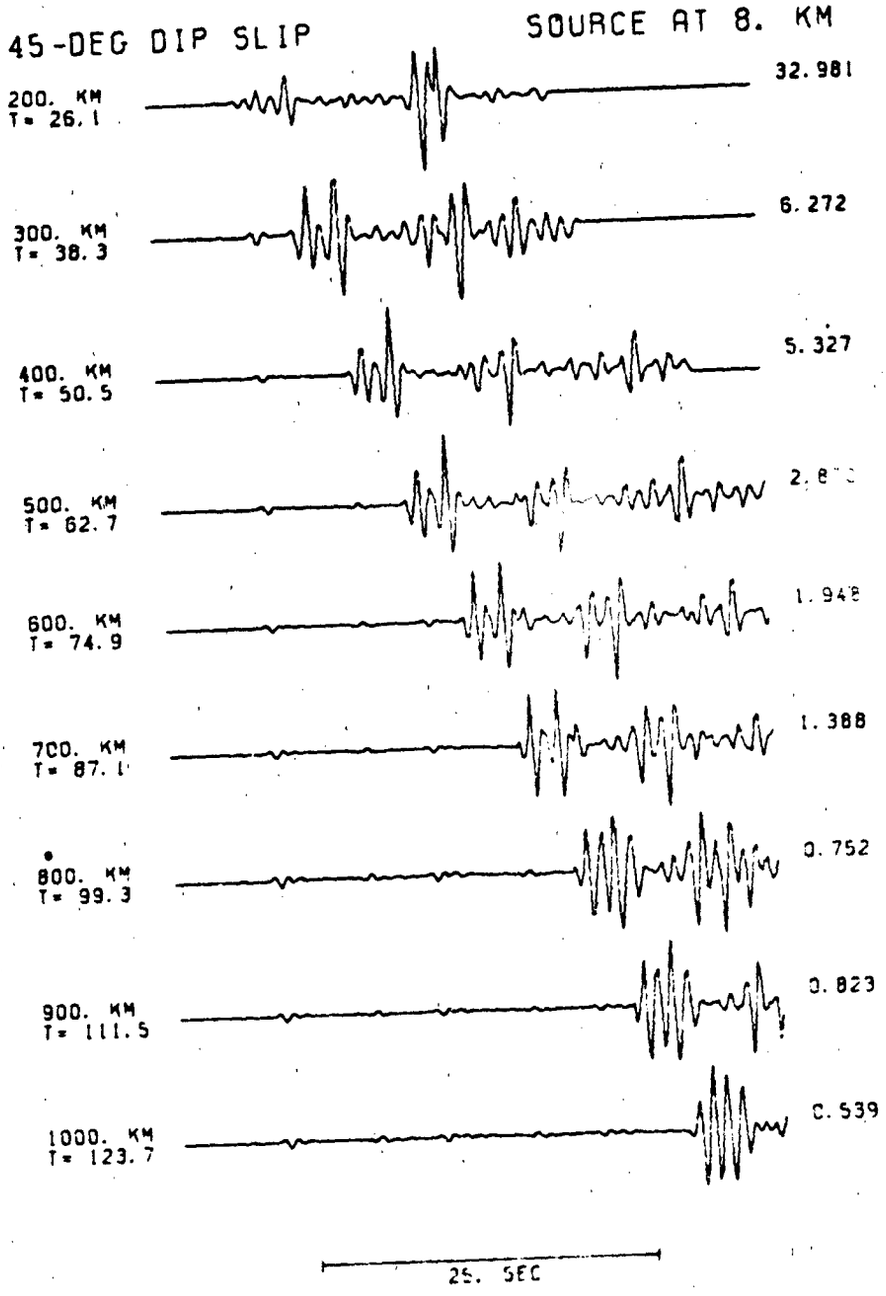
45-DEG DIP SLIP
SOURCE AT 8. KM
200. KM
T= 26.1
32.981
300. KM
T= 38.3
6.272
400. KM
T= 50.5
5.327
500. KM
T= 62.7
2.8
600. KM
T= 74.9
1.94
700. KM
T= 87.1
1.388
800. KM
T= 99.3
0.752
900. KM
T= 111.5
0.823
1000. KM
T= 123.7
0.539
25. SEC

Figure 32c

TABLE I

Velocity Model used for Generalized Ray Calculations

| P Velocity (km/sec) | S Velocity (km/sec) | Density (gm/ee) | Thickness (km) |
|---|---|---|---|
| 1.5 | 0.0 | 1.0 | 4 |
| 6.2 | 3.5 | 2.7 | 15 |
| 8.2 | 4.74 | 3.4 | 70 |
| 7.5 | 4.33 | 3.16 | 40 |
| 7.7 | 4.45 | 3.23 | 40 |
| 7.8 | 4.51 | 3.26 | 20 |
| 8.0 | 4.62 | 3.32 | 13.3 |
| 8.05 | 4.65 | 3.34 | 13.3 |
| 8.11 | 4.69 | 3.36 | 13.3 |
| 8.16 | 4.72 | 3.38 | 13.3 |
| 8.22 | 4.75 | 3.40 | 13.3 |

leaving downward from the source as shear and converting to P at the Moho). The first three figures, 33, 34, and 35, show the synthetic seismograms with each trace amplitude normalized independently. The last figure, 36, is a duplication of Figure 33 with the trace amplitudes normalized to the 100 km record in order to more dramatically illustrate the shadow zone effect on the arrivals in the seismograms. In each example, the first arriving phase are the $P_n$ and slightly diving phases, the second major arrivals are the $P_g$ direct and first multiple bounce phases.

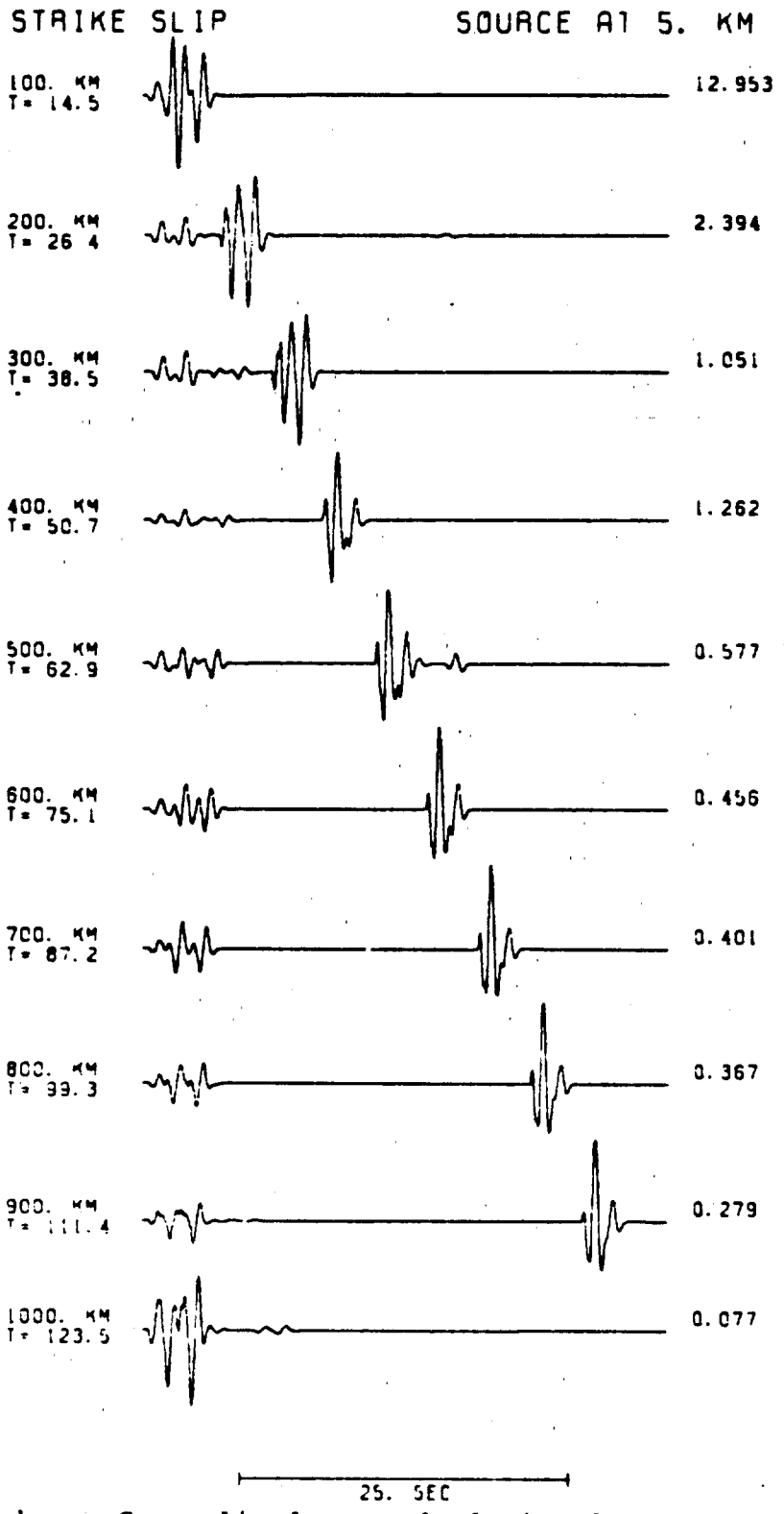


Figures 33a,b,c. Generalized ray calculation for model shown in Table I and a source depth of 5 km beneath the ocean bottom. Included in the ray sum are the direct ray, down going primary rays (i.e., one reflection, no mode conversion), and primary rays from

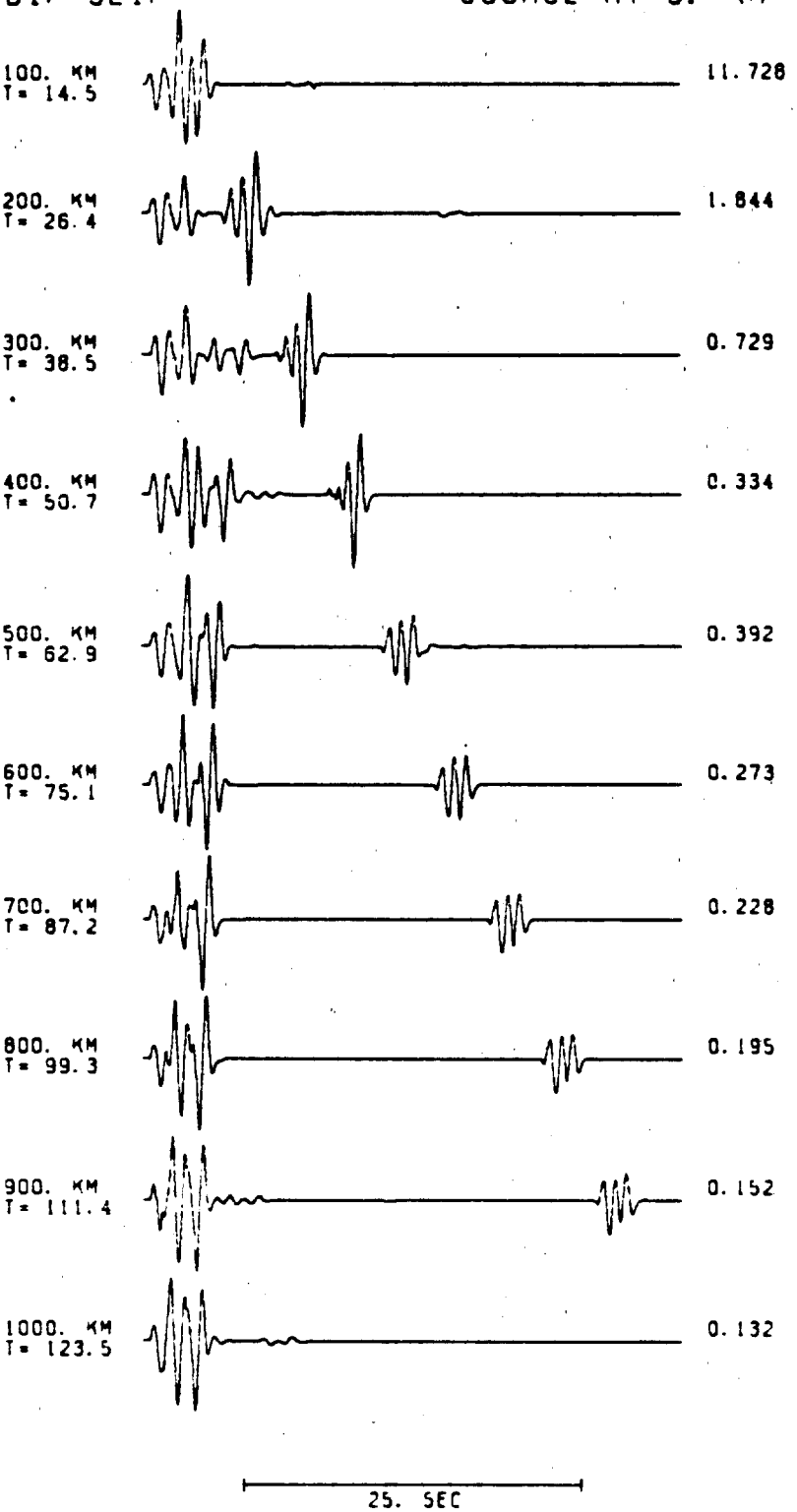
DIP SLIP
SOURCE AT 5. KM
100. KM
T= 14.5
11.728
200. KM
T= 26.4
1.844
300. KM
T= 38.5
0.729
400. KM
T= 50.7
0.334
500. KM
T= 62.9
0.392
600. KM
T= 75.1
0.273
700. KM
T= 87.2
0.228
800. KM
T= 99.3
0.195
900. KM
T= 111.4
0.152
1000. KM
T= 123.5
0.132
25. SEC

Figure 33b.

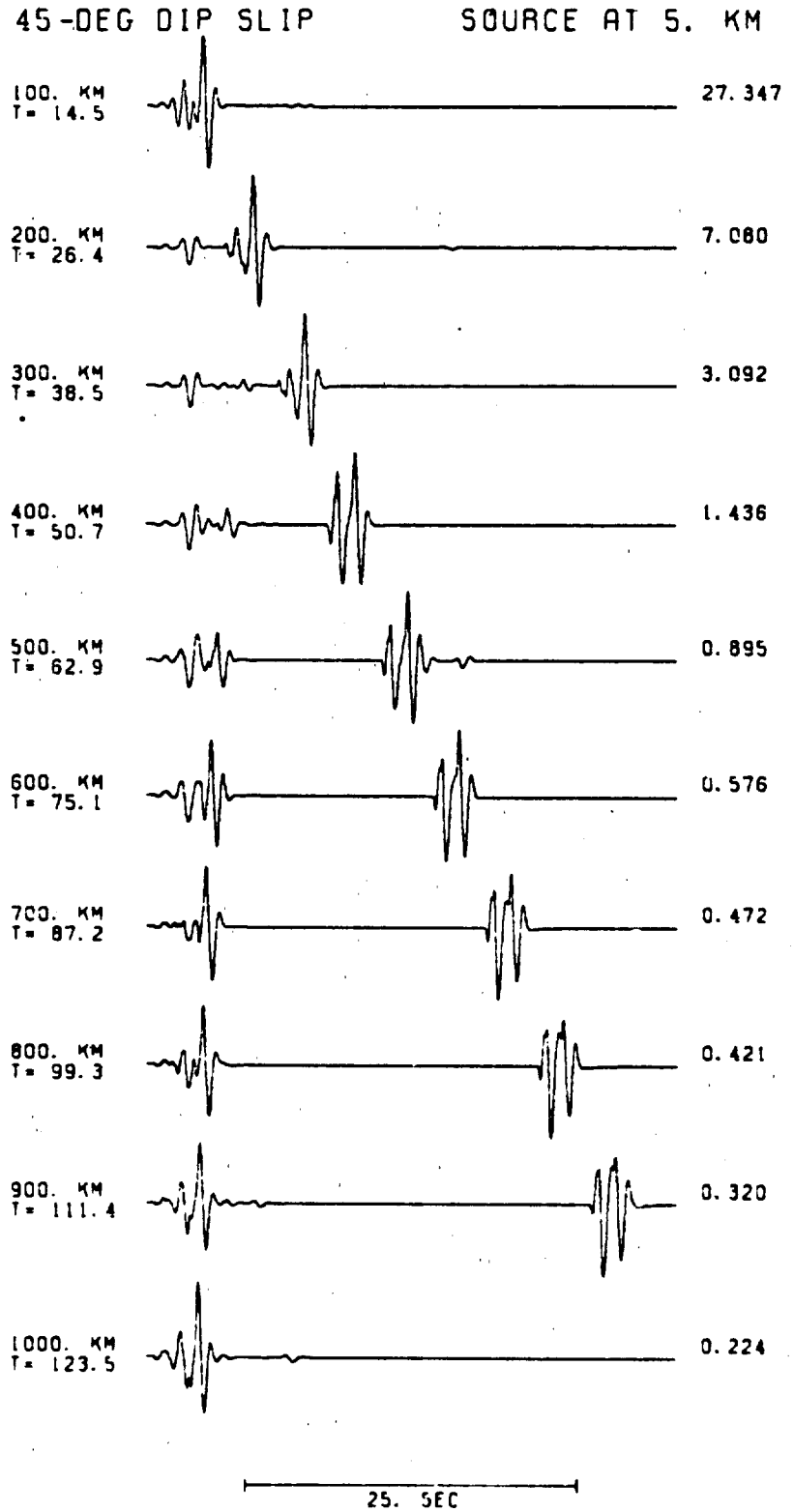
45-DEG DIP SLIP
SOURCE AT 5. KM
100. KM
T= 14.5
27.347
200. KM
T= 26.4
7.080
300. KM
T= 38.5
3.092
400. KM
T= 50.7
1.436
500. KM
T= 62.9
0.895
600. KM
T= 75.1
0.576
700. KM
T= 87.2
0.472
800. KM
T= 99.3
0.421
900. KM
T= 111.4
0.320
1000. KM
T= 123.5
0.224
25. SEC

Figure 33c.

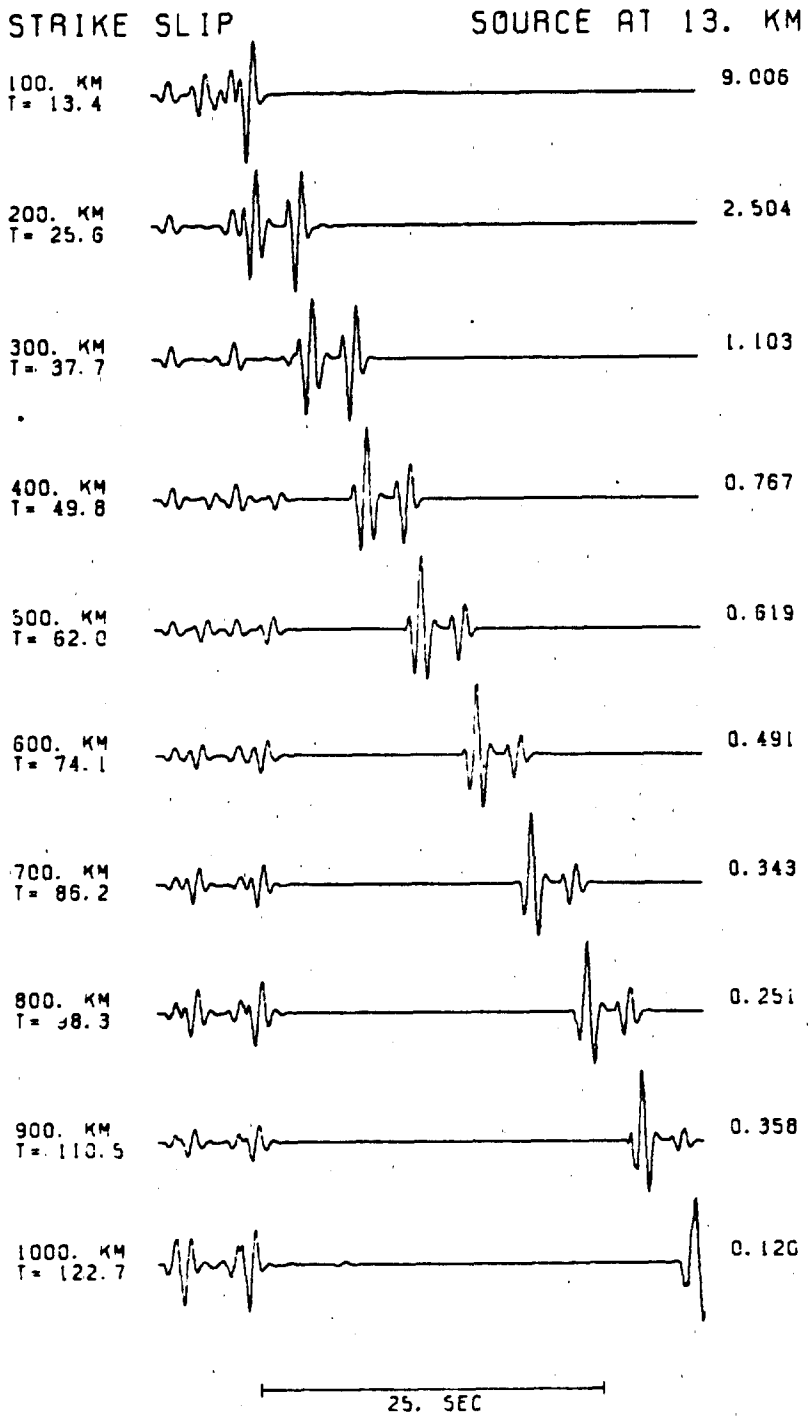


Figures 34a,b,c. Generalized ray calculations for sources 13 km below the ocean floor (same as Figure 33 except for depth change).

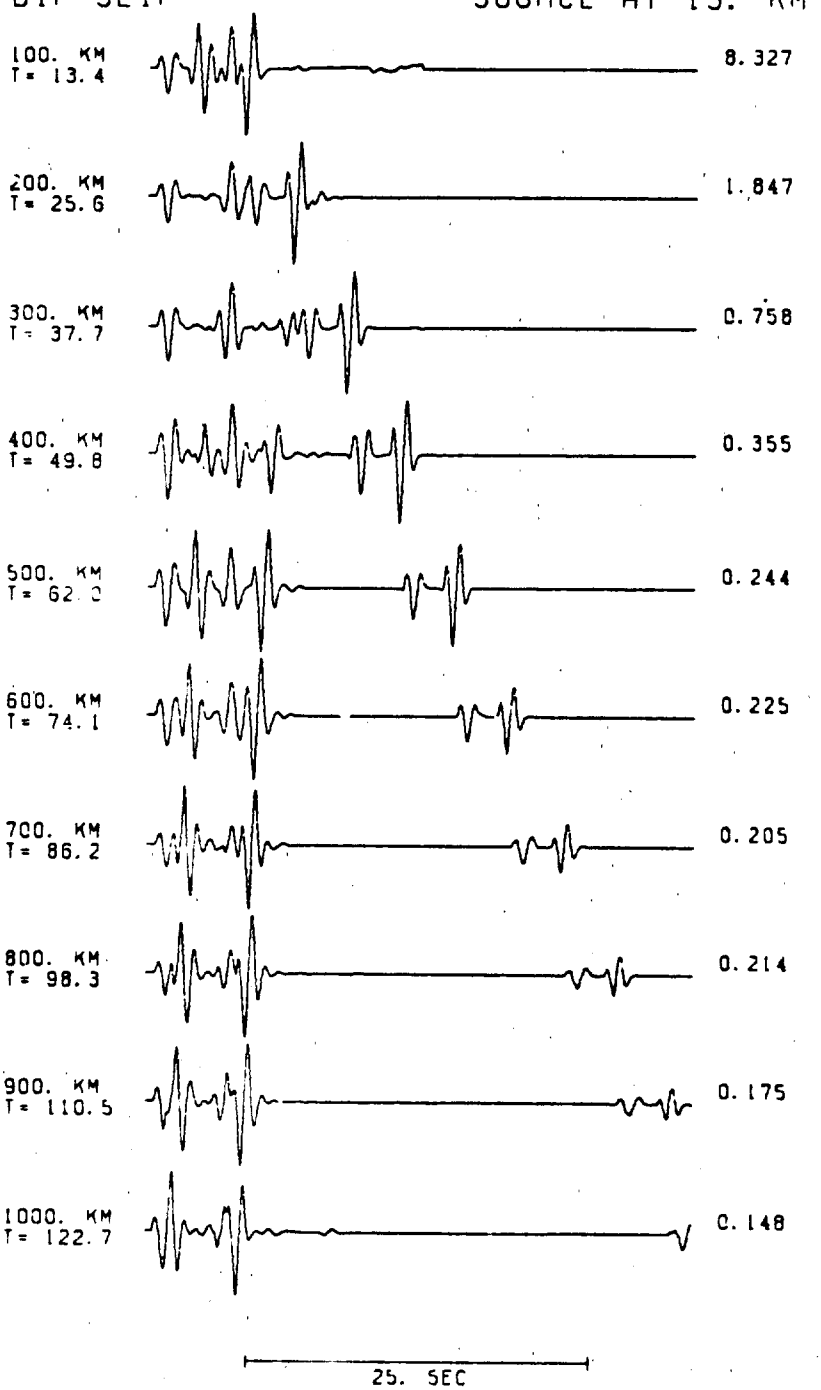
DIP SLIP
SOURCE AT 13. KM
100. KM
T= 13.4
8.327
200. KM
T= 25.6
1.847
300. KM
T= 37.7
0.758
400. KM
T= 49.8
0.355
500. KM
T= 62.0
0.244
600. KM
T= 74.1
0.225
700. KM
T= 86.2
0.205
800. KM
T= 98.3
0.214
900. KM
T= 110.5
0.175
1000. KM
T= 122.7
0.148
25. SEC

Figure 34b.

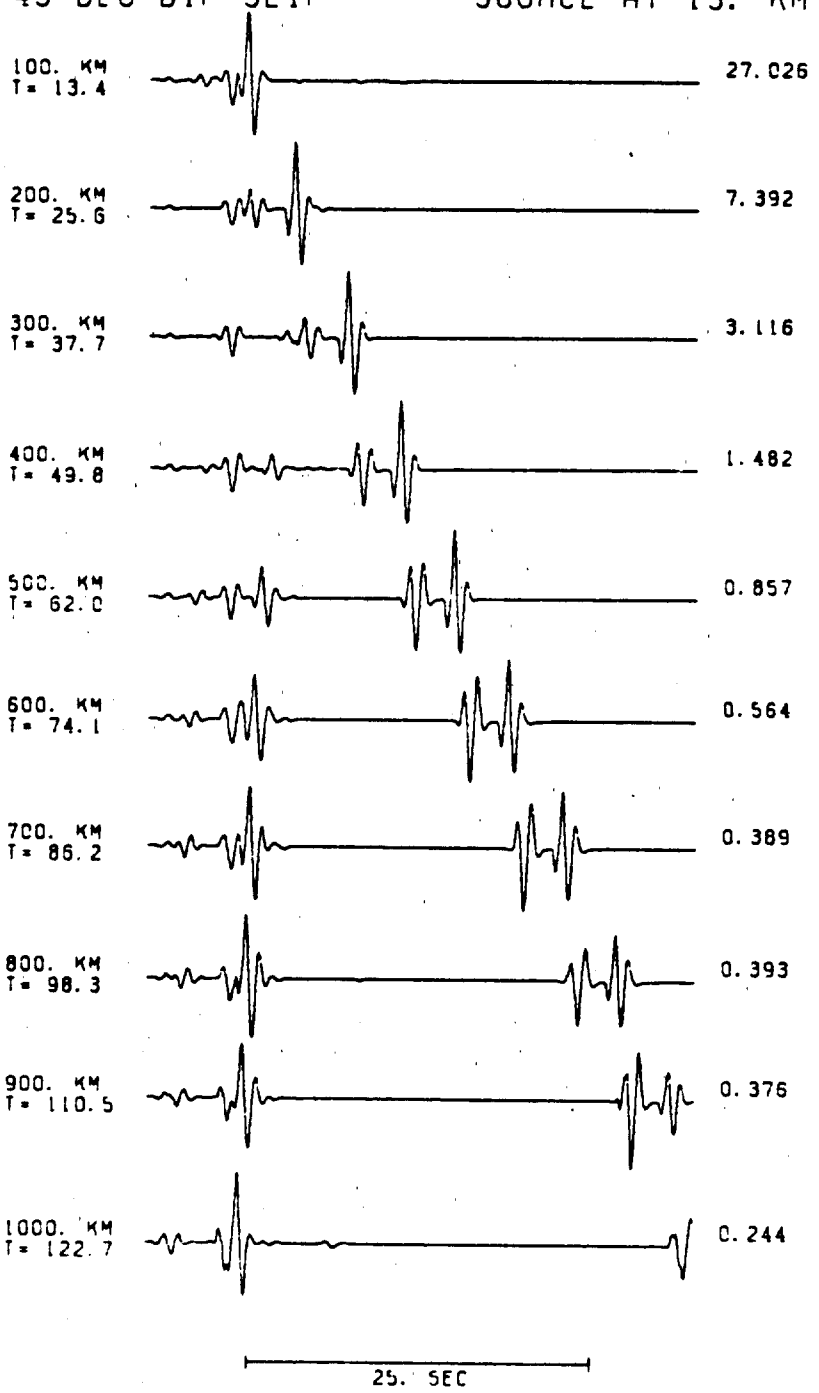
45-DEG DIP SLIP
SOURCE AT 13. KM
100. KM
T= 13.4
27.026
200. KM
T= 25.6
7.392
300. KM
T= 37.7
3.116
400. KM
T= 49.8
1.482
500. KM
T= 62.0
0.857
600. KM
T= 74.1
0.564
700. KM
T= 86.2
0.389
800. KM
T= 98.3
0.393
900. KM
T= 110.5
0.376
1000. KM
T= 122.7
0.244
25. SEC

Figure 34c.

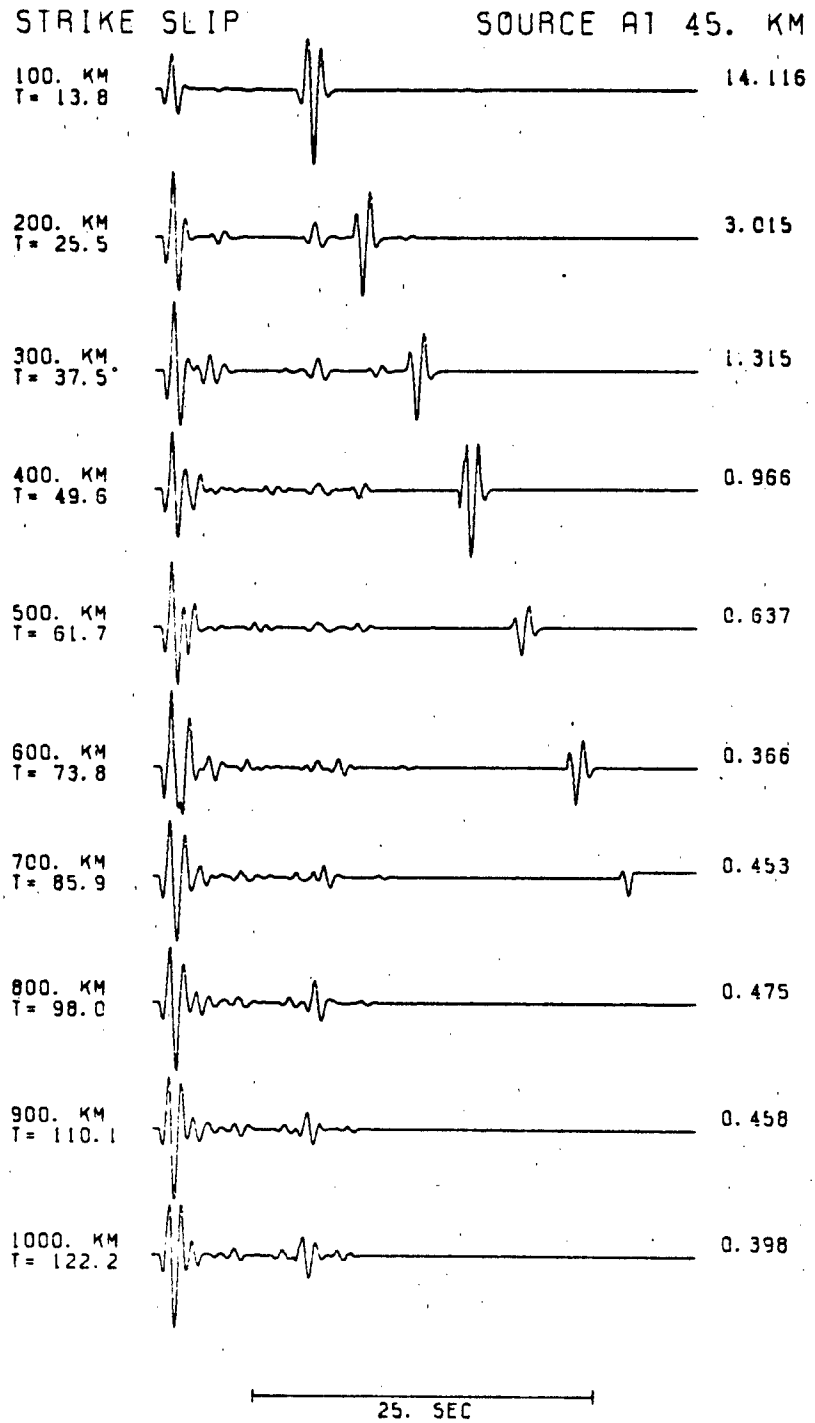


Figures 35a,b,c. Generalized ray calculations assuming a source depth of 45 km. Also included in the ray sum are the first reflections (sP, pP) from the Moho.

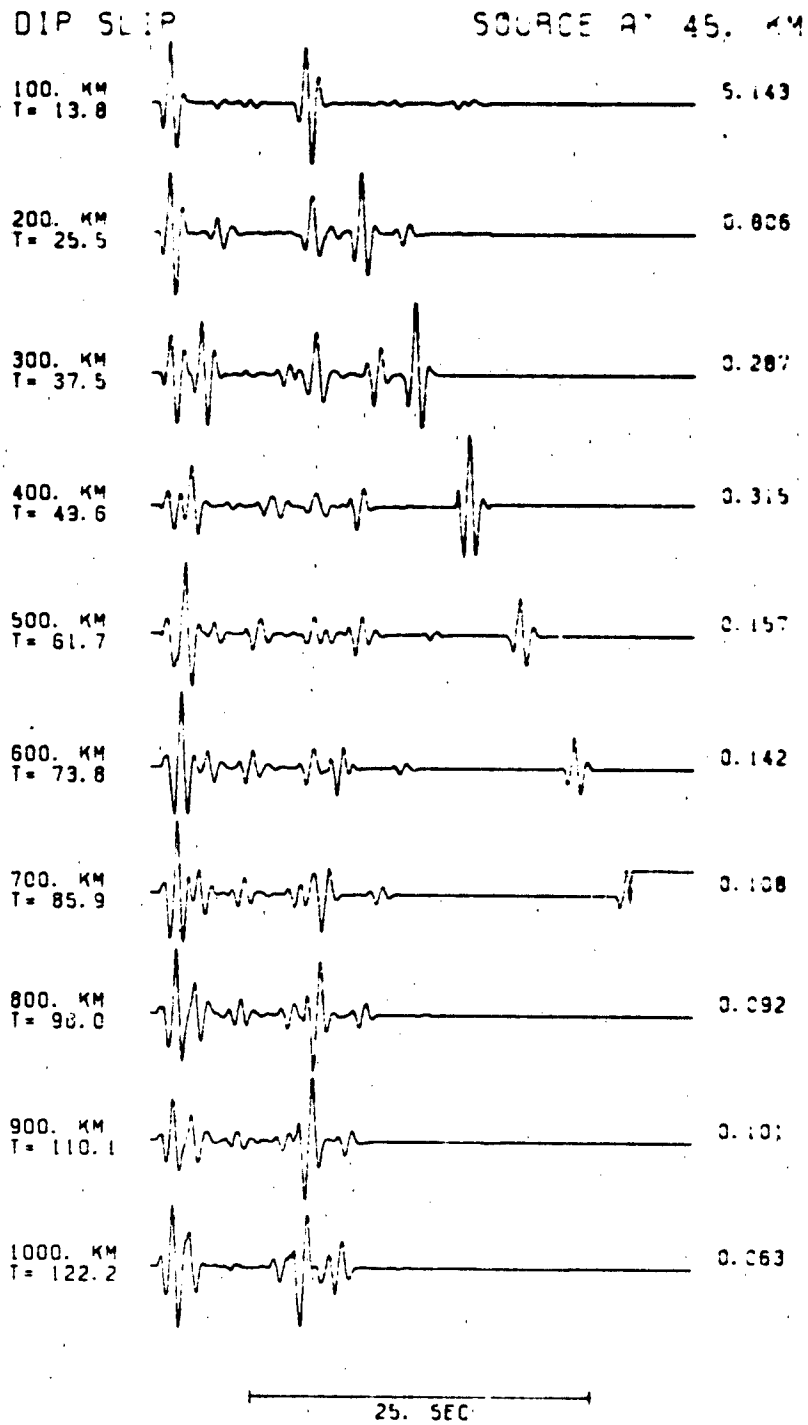
DIP SLIP
SOURCE AT 45. KM
100. KM
T= 13.8
5.143
200. KM
T= 25.5
0.806
300. KM
T= 37.5
0.287
400. KM
T= 49.6
0.315
500. KM
T= 61.7
0.157
600. KM
T= 73.8
0.142
700. KM
T= 85.9
0.108
800. KM
T= 98.0
0.092
900. KM
T= 110.1
0.101
1000. KM
T= 122.2
0.063
25. SEC

Figure 35b.

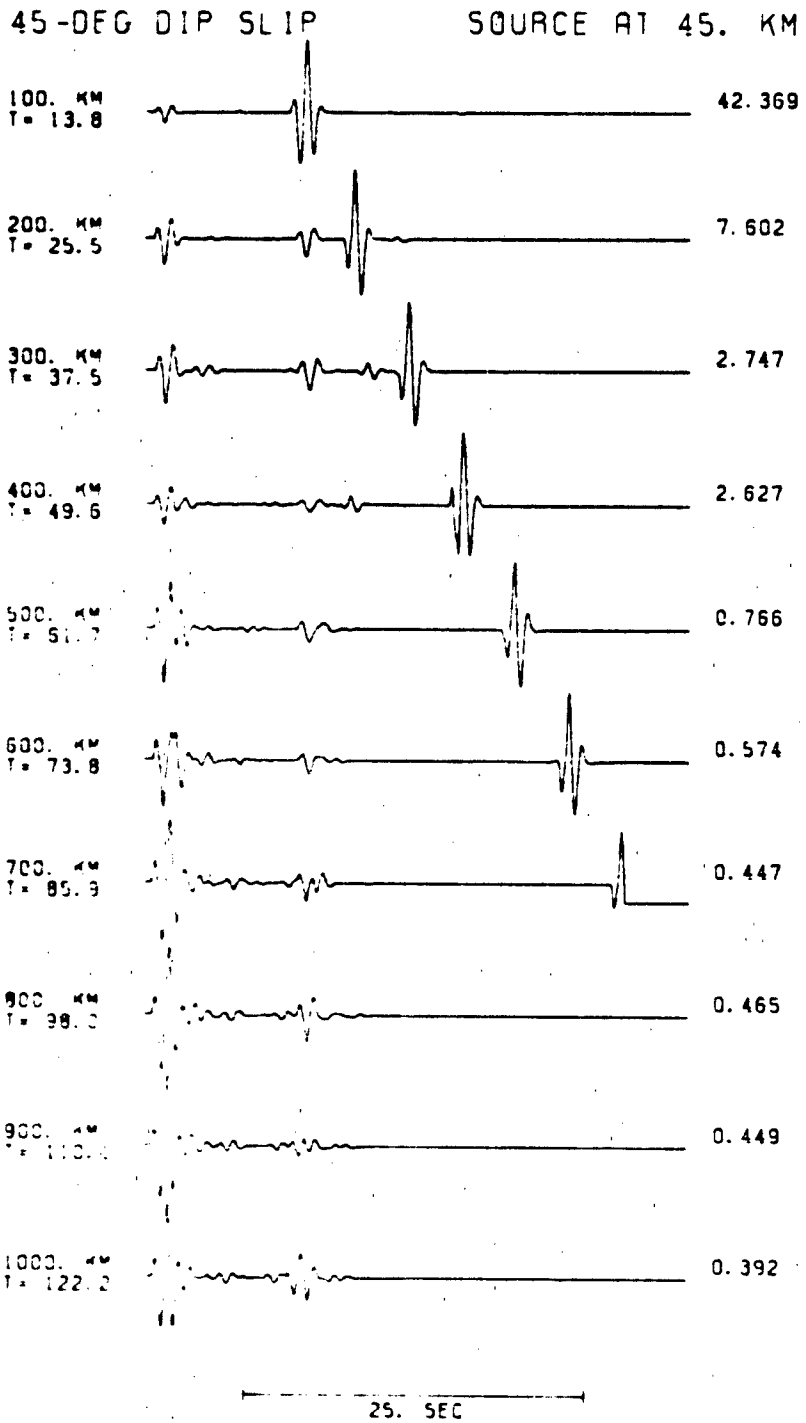
45-DEG DIP SLIP
SOURCE AT 45. KM
100. KM
T= 13.8
42.369
200. KM
T= 25.5
7.602
300. KM
T= 37.5
2.747
400. KM
T= 49.6
2.627
500. KM
0.766
600. KM
T= 73.8
0.574
700. KM
0.447
800. KM
0.465
900. KM
0.449
1000. KM
T= 122.2
0.392
25. SEC

**Figure 35c.**

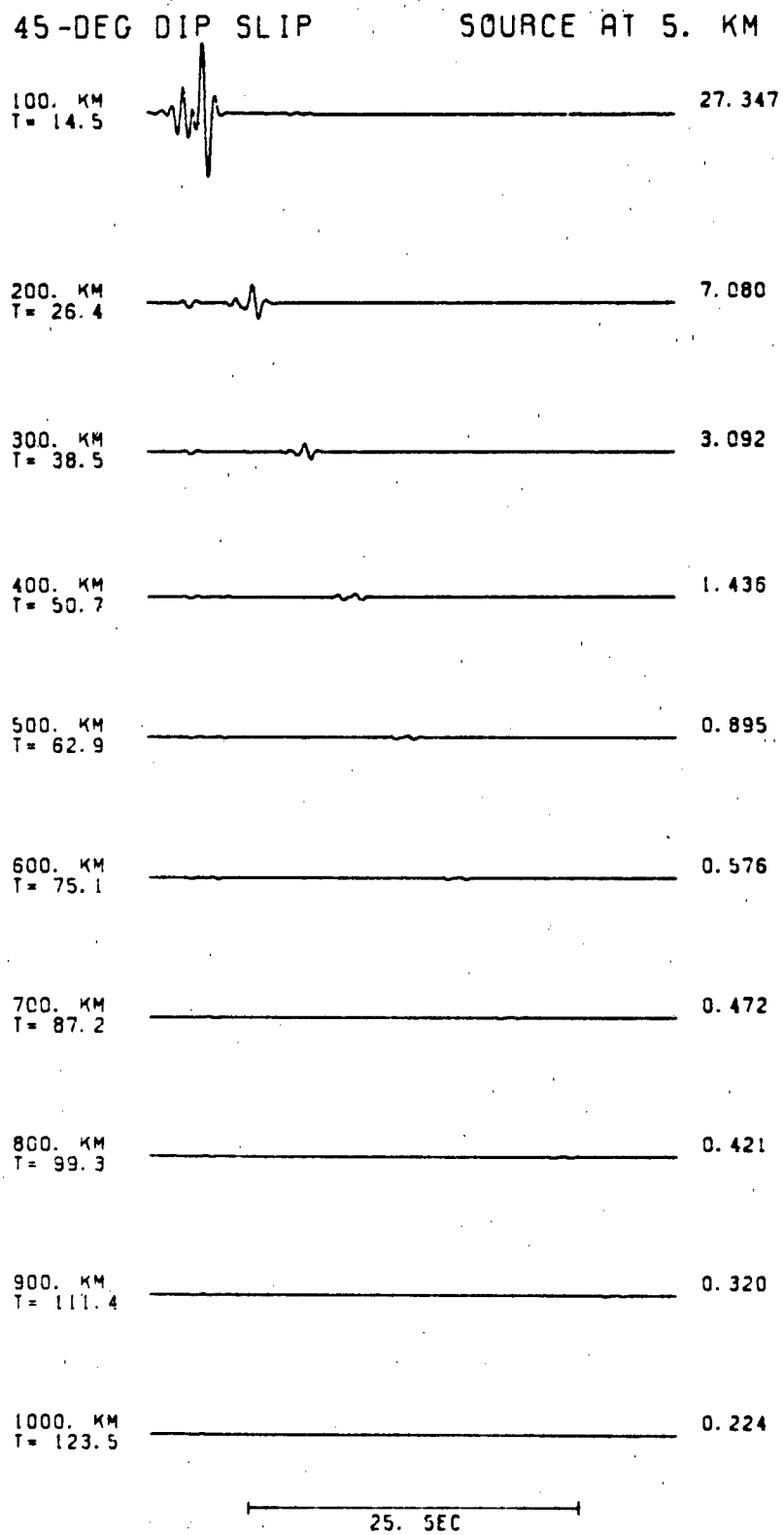


Figures 36a,b,c. This figure is a u plot of Figure 33 with the amplitudes scaled the same. The decay in amplitude is a "shadow zone" caused by the low velocity zone at 85 km depth.

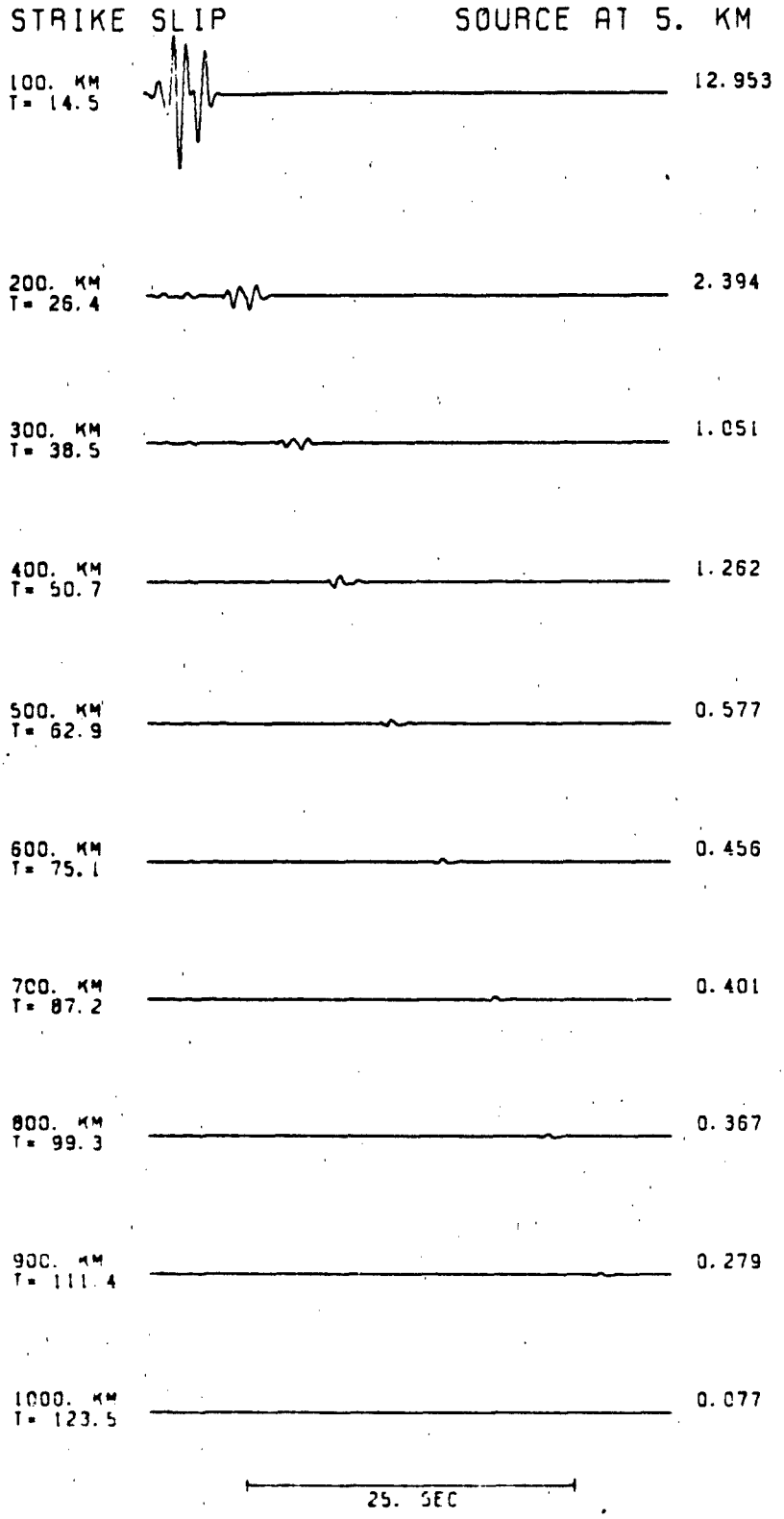
STRIKE SLIP
SOURCE AT 5. KM
100. KM
T= 14.5
12.953
200. KM
T= 26.4
2.394
300. KM
T= 38.5
1.051
400. KM
T= 50.7
1.262
500. KM
T= 62.9
0.577
600. KM
T= 75.1
0.456
700. KM
T= 87.2
0.401
800. KM
T= 99.3
0.367
900. KM
T= 111.4
0.279
1000. KM
T= 123.5
0.077
25. SEC

Figure 36b.

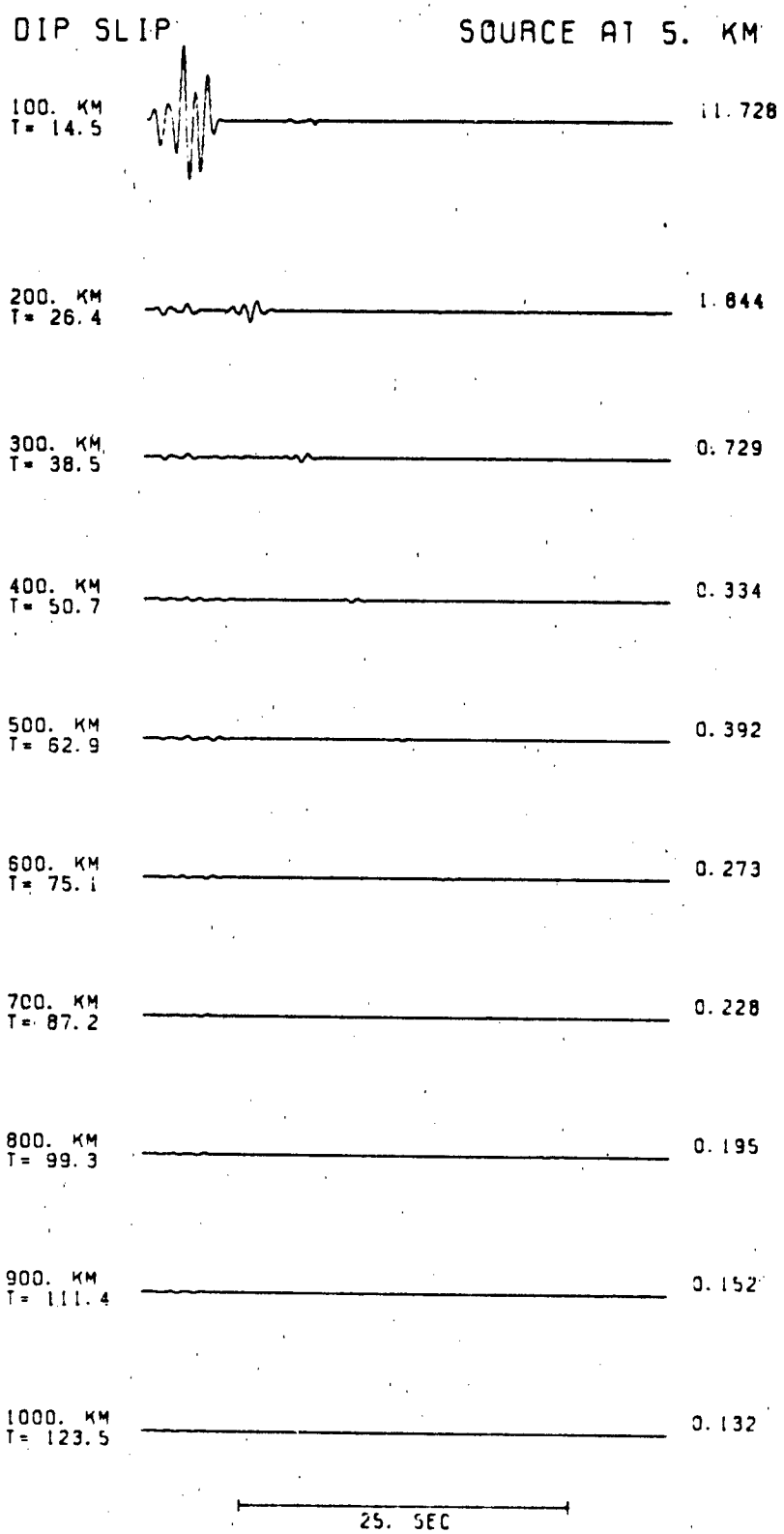
DIP SLIP
SOURCE AT 5. KM
100. KM
T= 14.5
11.728
200. KM
T= 26.4
1.844
300. KM
T= 38.5
0.729
400. KM
T= 50.7
0.334
500. KM
T= 62.9
0.392
600. KM
T= 75.1
0.273
700. KM
T= 87.2
0.228
800. KM
T= 99.3
0.195
900. KM
T= 111.4
0.152
1000. KM
T= 123.5
0.132
25. SEC

Figure 36c.

## SUMMARY AND CONCLUSIONS

This project has involved the calculation of literally tens of thousands of rays through a rapidly changing, laterally heterogeneous material. The purpose of the study was to provide an additional seismological evaluation of potential sites for the MSS system. In the course of the investigation, a detailed three-dimensional upper mantle model was constructed for the Kuriles/Kamchatka area. The adoption of this, or any other, model is a crucial step in the overall analysis. The results presented within this report are based very strongly upon the velocity structure selected. The model used here was a modification of the Veith (1974) model. This model has the advantage of being based on a very large set of corrected seismic travel-times and is felt to be quite reliable. Large changes in the velocity structure used could alter some of our conclusions. However, we have also performed the simulation using an unwarped slab model. The results do not greatly differ between the two calculations. Thus, we can analyze the results with some confidence.

There is a tendency to become somewhat inundated with detail when one attempts to assimilate the results from this study. It is necessary to maintain a broad overview and to identify consistent patterns in the predicted energy density. This has been true throughout the project. The scale of the questions addressed and the broad geographical area involved required that the investigation emphasize broadly-based analysis methods and not concentrate on small details. On this basis, we can draw several

significant conclusions from the study and provide a firm foundation for siting recommendations.

In referring to the four potential MSS sites identified here, we shall use the designators Sta. 3, Sta. 4, Sta. 1, and Sta. 1a to indicate the four sites in order of decreasing latitude (i.e., Sta. 3 is the northernmost site, Sta. 1a the southernmost).

When one considers the results of the ray-tracing analysis (sources deeper than 100 km), we find that Sta. 3 is, by a large margin, the best site in terms of ability to see diving rays from most of the region. Only three of the sixteen hypocenters considered resulted in Sta. 3 being in a shadow zone (these hypocenters were all at 150 km depth for the three northernmost source sets). Using the same criteria, Sta. 1 represents the least desirable site. However, if we are particularly interested in shallow events under Kamchatka the two southern sites, Sta. 1 and especially Sta. 1a are superior to the other stations in their ability to see diving rays from northern events. Indeed, Sta. 1a is at a very intense, bright spot for several northern locations. In the end, the seismological evaluation of each site is dependent upon a decision of which seismic area is of greatest interest. From our perspective, for best uniform coverage of the region, we would rate the four site locations in order of desirability as: Sta. 3, Sta. 1a, Sta. 4, and finally, Sta. 1.

On the basis of other siting criteria, a station that is situated in a shadow zone for much of the studied seismic area may be desirable. The utility of such a station would necessarily

require a thorough understanding of the multiple phases and non-geometric arrivals that typify the location. A simulation and discussion of these multiple reflected and refracted phases was presented earlier in this report, Figures 32-36. Distances from the source as well as fine details of the path are of utmost importance. The obvious difficulty with the interpretation of such seismic data for the determination of source parameters is the poorly defined path-dependent propagational effects.

There are several obvious directions for future research that have come to light during the course of this investigation. Ultimately synthetic seismograms that correctly account for laterally varying structures will be required. With the addition of multiple reflected arrivals, the current code could be modified to generage synthetic seismograms that correctly account for amplitude, timing and phase-shifts of later arrivals. Such a code would be quite valuable for the determination of source characteristics.

## REFERENCES

Anderson, D.L. and R.S. Hart, An earth model based on free oscillations and body waves, J. Geophys. Res., 81, p. 1461, 1976.

Bullen, K.E., Introduction to the Theory of Seismology, Cambridge University Press, Cambridge, 381 pp., 1965.

Chapman, C.H., Exact and approximate generalized ray theory in vertically inhomogeneous media, Geophys. J. R. Astr. Soc., 46, p. 201, 1976.

Davies, D. and B. R. Julian, A study of short period P-wave signals from Longshot, Geophys. J. R. Astr. Soc., 29, p. 185, 1972.

de Hoop, A.T., A modification of Cagniard's method for solving seismic pulse problems, Appl. Sci. Res. B., 8, p. 349, 1960.

Fuchs, K. and G. Muller, Computation of synthetic seismograms with the reflectivity method and comparison with observations, Geophys. J. R. Astr. Soc., 23, p. 417, 1971.

Goldstein, H., Classical Mechanics, Addison-Wesley Publishing, Reading, Mass., 399 pp., 1950.

Hasegawa, A., N. Umino, and S. Takagi, Fine structure of deep seismic plane in Northeast Japan (abstract), Spring Meeting of Seismological Society of Japan, 1976.

Helmberger, D.V., the crust mantle transition in the Bering Sea, Bull. Seism. Soc. Am., 58, p. 179, 1968.

Helmberger, D.V., and G.R. Engen, Modeling the long period body waves from shallow earthquakes at regional distances, Bull. Seism. Soc. Am., (in press) 1980.

Helmberger, D.V. and R. Wiggins, Upper mantle structure of the midwestern United States, J. Geophys. Res., 86, p. 3229, 1973.

Jacob, K., Global tectonic implications of anomalous seismic P traveltimes from the nuclear explosion Longshot, J. Geophys. Res., 77, p. 2556, 1972.

Le Pichon, X., Sea floor spreading and continental drift, J. Geophys. Res., 73, p. 3661, 1968.

Mellman, G.R. and D. V. Helmberger, A modified first motion approximation for the synthesis of body wave seismograms, Geophys. J. R. Astr. Soc., 54, p. 129, 1978.

Ringwood, A.E., Composition and evolution of the upper mantle, in The Earth's Crust and Upper Mantle, AGU Monograph 13, P. J. Hart (ed.), p. 1, 1969.

Toksöz, M.N., J. W. Minear, and B.R. Julian, Temperature field and geophysical effects of a downgoing slab, J. Geophys. Res., 76, p. 1113, 1971.

Veith, K.F., The Relationship of Island Arc to Plate Tectonics, Ph.D. Thesis, Southern Methodist University, Dallas, Texas, 1974.

Wiggins, R.A., Body wave amplitude calculations II, Geophys. J. R. Astr. Soc., 46, p. 1, 1976.